

BIASES IN METALLICITY MEASUREMENTS FROM GLOBAL GALAXY SPECTRA: THE EFFECTS OF FLUX-WEIGHTING AND DIFFUSE IONIZED GAS CONTAMINATION

RYAN L. SANDERS¹, ALICE E. SHAPLEY¹, KAI ZHANG², AND RENBIN YAN²

Draft version November 8, 2018

ABSTRACT

Galaxy metallicity scaling relations provide a powerful tool for understanding galaxy evolution, but obtaining unbiased global galaxy gas-phase oxygen abundances requires proper treatment of the various line-emitting sources within spectroscopic apertures. We present a model framework that treats galaxies as ensembles of H II and diffuse ionized gas (DIG) regions of varying metallicities. These models are based upon empirical relations between line ratios and electron temperature for H II regions, and DIG strong-line ratio relations from SDSS-IV MaNGA IFU data. Flux-weighting effects and DIG contamination can significantly affect properties inferred from global galaxy spectra, biasing metallicity estimates by more than 0.3 dex in some cases. We use observationally-motivated inputs to construct a model matched to typical local star-forming galaxies, and quantify the biases in strong-line ratios, electron temperatures, and direct-method metallicities as inferred from global galaxy spectra relative to the median values of the H II region distributions in each galaxy. We also provide a generalized set of models that can be applied to individual galaxies or galaxy samples in atypical regions of parameter space. We use these models to correct for the effects of flux-weighting and DIG contamination in the local direct-method mass-metallicity and fundamental metallicity relations, and in the mass-metallicity relation based on strong-line metallicities. Future photoionization models of galaxy line emission need to include DIG emission and represent galaxies as ensembles of emitting regions with varying metallicity, instead of as single H II regions with effective properties, in order to obtain unbiased estimates of key underlying physical properties.

Keywords: galaxies: ISM — galaxies: abundances

1. INTRODUCTION

The formation and growth of galaxies over cosmic history are governed by the relationship between gas accretion, star formation, and feedback. Understanding this process, known as the “cycle of baryons,” is of critical importance to gaining a full picture of galaxy growth, but directly observing gas in inflow and outflow stages is observationally challenging. In lieu of direct observations, the cycle of baryons can be probed indirectly by measuring the chemical abundances of galaxies. In particular, the scaling of gas-phase oxygen abundance, which we refer to in this work as “metallicity,” with global galaxy properties such as stellar mass (M_*) and star-formation rate (SFR) can give insight into the interplay between inflows, outflows, and star formation.

A monotonic increase in metallicity with increasing stellar mass has been observed for local star-forming galaxies, and is known as the “mass-metallicity relation” (MZR; e.g., Tremonti et al. 2004; Kewley & Ellison 2008; Andrews & Martini 2013). The $z \sim 0$ MZR has been found to have a secondary dependence on SFR, with the relationship among M_* , SFR, and metallicity known as the “fundamental metallicity relation” (FMR; e.g., Mannucci et al. 2010; Lara-López et al. 2010; Andrews & Martini 2013; Salim et al. 2014, but see Sánchez et al. 2013; Barrera-Ballesteros et al. 2017 for conflicting re-

sults using spatially-resolved data). Chemical evolution models make predictions for the shape and normalization of these metallicity scaling relations under different sets of assumptions about the nature of galactic winds and the balance between inflow, outflow, and SFR (e.g., Finlator & Davé 2008; Peebles & Shankar 2011; Zahid et al. 2014; Davé et al. 2017). An accurate comparison between chemical evolution models and the observed MZR and FMR can elucidate the nature of feedback and cosmological accretion. However, such a comparison depends critically on robust measurements of metallicity for observed star-forming galaxy samples, and additionally requires the measurement of a metallicity that is compatible with metallicities extracted from cosmological hydrodynamical simulations. It is thus of paramount importance to eliminate observational biases in galaxy metallicity estimates.

The gas-phase oxygen abundances of galaxies in the local universe are typically estimated using one of two methods. In the so-called “direct method,” the temperature-sensitive ratio of the intensities of an auroral emission feature (e.g., [O III] λ 4363, [O II] λ λ 7320,7330, [N II] λ 5755) to strong emission lines from the same ionic species (e.g., [O III] λ λ 4959,5007, [O II] λ λ 3726,3729, [N II] λ λ 6548,6584) is used to measure the electron temperature of the ionized gas (Osterbrock & Ferland 2006). The cooling efficiency of ionized gas increases as the metal abundance increases. Thus, the gas-phase metallicity can be determined from the equilibrium electron temperature, assuming a heating and cooling balance (Izotov et al. 2006; Pilyugin et al. 2012a). This method is the most accurate method of metallicity determina-

email: rlsand@astro.ucla.edu

¹Department of Physics & Astronomy, University of California, Los Angeles, 430 Portola Plaza, Los Angeles, CA 90095, USA

²Department of Physics and Astronomy, University of Kentucky, 505 Rose Street, Lexington, KY 40506, USA

tion that can be applied to reasonably large samples ($N > 100$) of low-redshift galaxies. The utility of the direct-method has been demonstrated by the observation that direct-method metallicities tightly correlate with metallicities obtained from oxygen recombination lines that more directly measure the oxygen abundance, where the relation has a slope of unity but an offset of ~ 0.2 dex from a one-to-one relation (Blanc et al. 2015). Metal recombination lines are $\sim 10^4$ times weaker than strong lines and thus are not a practical metallicity indicator for any large sample. While the accuracy of the direct method is desirable, its use is limited because auroral lines are typically $\sim 50 - 100$ times weaker than strong optical emission lines at low-metallicities ($12 + \log(\text{O}/\text{H}) \lesssim 8.2$) and become weaker exponentially as metallicity increases, making it extremely difficult to detect these lines in individual metal-rich galaxies. For these reasons, samples of local galaxies with auroral line detections have sizes of only a few hundred and do not extend to $12 + \log(\text{O}/\text{H}) \gtrsim 8.4$ (Izotov et al. 2006; Pilyugin et al. 2010).

When auroral lines are not detected, galaxy oxygen abundances may be estimated from methods using only strong optical emission lines. The “strong-line method” utilizes empirical or theoretical calibrations between strong optical emission line ratios and oxygen abundance. Empirical calibrations are based on samples of individual H II regions with direct-method metallicities (e.g., Pettini & Pagel 2004). Theoretical calibrations instead make use of the predictions of photoionization models to determine the relations between line ratios and oxygen abundance (e.g., Kewley & Dopita 2002; Kobulnicky & Kewley 2004; Tremonti et al. 2004; Dopita et al. 2016). Because the strong-line method does not depend on the detection of any intrinsically weak emission lines, it can be applied to much larger samples of galaxies than the direct method. Strong-line metallicities have been estimated for sample sizes of $> 10^4$ galaxies (e.g., Tremonti et al. 2004) thanks to large spectroscopic surveys such as the Sloan Digital Sky Survey (SDSS; York et al. 2000).

Both the strong-line and direct methods share an inherent flaw when used to determine galaxy metallicities: they assume that the object of interest is a single H II region. Empirical strong-line calibrations utilize H II regions as the calibrating dataset, and will therefore not produce a reliable metallicity if the target does not follow the same relations between line ratios and oxygen abundance as H II regions. Theoretical strong-line calibrations are produced from photoionization models of single H II regions (or in many cases a single slab of illuminated gas) and thus also assume that the target behaves similarly to an individual star-forming region. When modeling galaxy emission spectra, it is common practice to illuminate the gas with the spectrum of a stellar population synthesis model (e.g., Starburst99; Leitherer et al. 2014) instead of a single stellar population (as in classical H II regions). However, this treatment fails to account for the variety of physical conditions of gas throughout the galaxy and the correlation of stellar properties with those variations. The direct method suffers from a similar problem, in that it assumes that the auroral and strong emission lines are produced in a single homogeneous H II region ionized by a single star cluster.

Galaxies are not single H II regions, but are instead complex objects with a multiphase gaseous interstellar medium (ISM) and intricate substructure. The warm ($\sim 10^4$ K) ionized phase includes H II regions with a range of properties, as well as diffuse ionized gas (DIG) not contained in H II regions. H II regions are the line-emitting component associated with recent star formation, in which gas in close proximity to young, massive stars is ionized and emits both recombination and collisionally-excited lines.

While the light from H II regions is of primary interest in determining gas-phase metallicity, other important sources of line emission exist in the ISM. DIG contributes significantly to optical line emission in local galaxies. Studies based on narrowband H α imaging suggest that DIG emission contributes 30 – 60% of the total H α flux in local spiral galaxies (Zurita et al. 2000; Oey et al. 2007). Additionally, DIG has different physical conditions and ionizing spectra from those of H II regions, and therefore likely follows different line ratio excitation sequences (Zhang et al. 2017). Hard ionizing radiation from accreting black holes incident on the ISM also produces line emission in galaxies harboring an active galactic nucleus (AGN), but in this study we ignore this source of line emission and focus only on galaxies dominated by star formation. Because of the diversity of ISM sub-components, applying the aforementioned methods to estimate galaxy metallicities while treating the galaxy as a single H II region will inevitably result in some level of bias.

The observed global galaxy spectrum is a flux-weighted combination of light on a line-by-line basis from each of these line-emitting components falling in the spectroscopic slit or fiber. For typical spectroscopic apertures (i.e., SDSS fibers), this mixture includes multiple H II and DIG regions with a spread in physical properties. A proper interpretation of the observed galaxy emission line spectrum cannot be obtained unless the mixture of these components is accounted for.

Robust galaxy gas-phase oxygen abundances are absolutely required when comparing observed metallicity scaling relations such as the MZR and FMR with simulations of galaxy chemical evolution. In this work, we reevaluate the reliability of oxygen abundances estimated from the emission lines of global galaxy spectra. For this analysis, we create simple models based on empirical auroral and strong emission line relations. These models include flux-weighting effects from the combination of emitting regions with a spread in physical properties, incorporating up-to-date line ratio and electron temperature relations for H II regions. An important novel component of our models is the inclusion of emission from DIG regions based upon recent empirical results on DIG line ratios from the ongoing SDSS-IV MaNGA IFU survey (Zhang et al. 2017). In Section 2, we motivate and describe the models and empirical relations upon which they are based. We present results from the models and compare to both composites and individual local galaxies from SDSS in Section 3. We characterize the biases in line ratios, electron temperature, and oxygen abundance measurements from global galaxy spectra in Section 4, and discuss the effects on metallicity measurements for local galaxies. In Section 5, we apply corrections to the

local mass-metallicity and fundamental metallicity relations and discuss DIG contamination in the context of other recent $z \sim 0$ galaxy line-ratio studies. In Section 6, we discuss the implications for metallicity measurements from both the direct and strong-line methods for high-redshift galaxies. Finally, we summarize and make concluding remarks in Section 7. Those readers who wish to skip over the details of the model framework may refer to Section 4 for the presentation of the biases in properties derived from global galaxy spectra, and subsequent sections for applications of the results.

Throughout this paper, we adopt shorthand abbreviations to refer to emission line ratios and present them here for the convenience of the reader. We normalize strong emission line fluxes to the $H\beta$ flux, following the practice of H II region studies. We use the following abbreviations for strong-line ratios throughout this work:

$$O3 = \log([\text{O III}]\lambda\lambda 4959, 5007/H\beta), \quad (1)$$

$$O2 = \log([\text{O II}]\lambda\lambda 3726, 3729/H\beta), \quad (2)$$

$$N2 = \log([\text{N II}]\lambda\lambda 6548, 6584/H\beta), \quad (3)$$

$$S2 = \log([\text{S II}]\lambda\lambda 6716, 6731/H\beta), \quad (4)$$

$$O3N2 = O3 - N2. \quad (5)$$

These strong-line ratios are always reddening-corrected unless otherwise noted. The strong-line ratios that utilize a single doublet component and/or the Balmer line with the closest proximity in wavelength to the forbidden line, more common in galaxy studies, can be found from these ratios: $\log([\text{O III}]\lambda 5007/H\beta) = O3 - 0.125$; $\log([\text{N II}]\lambda 6584/H\alpha) = N2 - 0.581$; $\log([\text{S II}]\lambda\lambda 6716, 6731/H\alpha) = S2 - 0.456$; and $\log([\text{O III}]\lambda 5007/H\beta)/([\text{N II}]\lambda 6584/H\alpha) = O3N2 + 0.456$. We also adopt abbreviations for the strong-to-auroral line ratios from which electron temperatures are estimated:

$$Q3 = [\text{O III}]\lambda\lambda 4959, 5007/\lambda 4363, \quad (6)$$

$$Q2 = [\text{O II}]\lambda\lambda 3726, 3729/\lambda\lambda 7320, 7330, \quad (7)$$

$$Q2N = [\text{N II}]\lambda\lambda 6548, 6584/\lambda 5755. \quad (8)$$

Whenever it occurs, the term “metallicity” is used synonymously with gas-phase oxygen abundance (O/H) unless otherwise mentioned. We assume a Λ CDM cosmology with $H_0 = 70 \text{ km s}^{-1} \text{ Mpc}^{-1}$, $\Omega_m = 0.3$, and $\Omega_\Lambda = 0.7$.

2. MODELING GALAXIES AS ENSEMBLES OF LINE-EMITTING REGIONS

There is clear evidence that global galaxy spectra cannot be described by H II region photoionization models or H II region empirical datasets alone. Local star-forming galaxies follow distinct excitation sequences from those of H II regions in the $[\text{O III}]\lambda 5007/H\beta$ vs. $[\text{S II}]\lambda\lambda 6716, 6731/H\alpha$, $[\text{O III}]\lambda 5007/H\beta$ vs. $[\text{O II}]\lambda\lambda 3726, 3729/H\beta$, and

$[\text{O III}]\lambda 5007/H\beta$ vs. $[\text{O I}]\lambda 6300/H\alpha$ diagrams (Croxall et al. 2015). Such differences, alongside other pieces of evidence from past studies presented below, motivate a modeling approach that treats galaxies as collections of multiple emitting regions spanning a range of excitation levels and oxygen abundances.

In this section, we discuss past work modeling global galaxy spectra as ensembles of emitting regions, describe the H II region and DIG datasets, present the line ratio relations and other inputs to the models, and outline the method by which the mock galaxy spectra are created. We evaluate the performance of these models in Section 3 by comparing to observations of galaxies from SDSS.

2.1. Previous investigations of global galaxy biases

Kobulnicky et al. (1999) investigated the question of whether chemical abundances could be reliably estimated from global galaxy spectra. Using a sample of six dwarf galaxies with both individual H II region and global galaxy spectra, the authors found that the global spectra systematically overestimated electron temperatures by $\sim 1,000 - 3,000 \text{ K}$ while underestimating direct-method $12+\log(O/H)$ by $\sim 0.05 - 0.2 \text{ dex}$ compared to the mean properties of the individual H II regions. These offsets were attributed to flux-weighting effects when combining light from multiple H II regions with different levels of excitation. Kobulnicky et al. also investigated the same question for local spiral galaxies by comparing measurements from individual H II regions to mock global spectra constructed using a weighted sum of the H II region spectra in radial bins. This analysis suggested that strong-line methods reproduced the mean metallicity of the individual H II regions without significant systematic effects despite the range of abundances in the individual H II region distributions. However, their spiral galaxy models did not incorporate dust reddening and, critically, contributions from DIG emission, which were poorly constrained at the time. Additionally, their sample of spiral and dwarf galaxies with direct-method measurements was very small ($N=6$) and only contained metal-poor ($12+\log(O/H) \leq 8.15$), low-mass objects. An analysis utilizing a more representative sample spanning a wide dynamic range in mass and metallicity is needed to test metallicity estimates from modern spectroscopic surveys.

Pilyugin et al. (2010) found that SDSS galaxies with auroral temperature measurements do not follow the H II region relationship between electron temperature as measured from O^+ (T_2) and O^{++} (T_3), known as the T_2-T_3 relation, but instead have lower T_2 at fixed T_3 . A similar galaxy ionic temperature offset of $\sim 1,000 - 1,500 \text{ K}$ lower T_2 at fixed T_3 compared to the H II region T_2-T_3 relation has been observed when T_2 and T_3 are inferred from composite spectra constructed from local SDSS star-forming galaxies (Andrews & Martini 2013; Curti et al. 2017). Such composite spectra leverage the large-number statistics of SDSS to measure auroral-line ratios over an unprecedentedly wide range of galaxy properties. Pilyugin et al. (2010) were able to roughly reproduce this offset by combining the spectra of 2-3 H II regions falling on the T_2-T_3 relation but spanning a wide range of temperatures, suggesting that such an offset could be the result of combining light from multiple line-emitting regions with different physical properties. However, the

models of Pilyugin et al. (2010) did not include any DIG component and thus were not representative of typical $z \sim 0$ star-forming galaxies. Pilyugin et al. (2012b) expanded on these results by simulating composite nebular spectra using a set of high-quality, self-consistent H II region observations as input components. These authors combined emission on a line-by-line basis from multiple H II regions with abundances within a certain range of a central metallicity value, and found that the combination of multiple H II regions can explain observed auroral-line properties of SDSS galaxies. Furthermore, the bias in inferred nebular abundances relative to the central metallicity value increases with increasing width of the metallicity range. We note that Pilyugin et al. (2012b) did not include any DIG emission regions in their composite spectra models. Collectively, these results imply that galaxy auroral and strong-line ratios do not behave in the same manner as those of individual H II regions. We build upon these previous studies of global galaxy spectra by creating models that treat galaxies ensembles of line-emitting regions with varying physical conditions, and crucially include a prescription for DIG emission.

2.2. An empirical approach to modeling galaxy spectra

In order to characterize the biases in measurements of electron temperature, oxygen abundance, and strong-line ratios from global galaxy spectra, we constructed a set of models that are based on observed line-ratio relations of H II and DIG regions. We treat a galaxy as a collection of H II and DIG regions with a distribution of physical properties, and create mock global galaxy spectra by summing the line fluxes from each individual component. These models are simple in nature, and minimize the number of free parameters that can be tuned to match observations of real galaxies. In the description that follows, we will attempt to make it clear when we were forced to make assumptions due to a lack of constraining observations.

We chose to base our models on empirical relations rather than photoionization models for two reasons. First, photoionization models have a large number of free parameters that can be fine-tuned to match a set of observations, often allowing for multiple degenerate solutions. The interpretation of emission lines through photoionization models depends on the various required assumptions such as the shape of the relation between N/O and O/H, the method of accounting for the depletion of gas-phase elements onto dust grains, and the properties of the ionizing stellar population. In contrast, we prioritize simplicity over flexibility, minimizing the number of free parameters.

Second, DIG emission cannot be properly represented in photoionization models because the relative contributions of various ionization sources for DIG are still not agreed upon. The DIG ionization mechanism appears to be photoionization from some combination of leaking Lyman-continuum from O and B stars in H II regions (Voges & Walterbos 2006; Haffner et al. 2009; Reynolds et al. 2012) and evolved intermediate-mass post-AGB stars (Flores-Fajardo et al. 2011; Zhang et al. 2017). Although O and B stars appear to provide most of the DIG ionization energy, there is an ongoing discussion about the importance of evolved stars. It has been suggested that additional nonionizing heating sources

such as shocks are required to explain DIG observations (Reynolds et al. 1999; Seon et al. 2011). Some emission attributed to DIG may also originate from dust-scattering of emission line photons produced in H II regions (Barnes et al. 2015; Ascasibar et al. 2016). These effects are difficult to include in photoionization models, and introduce significant uncertainties.

By utilizing observed line ratio relations for both DIG and H II regions, we minimize the number of free parameters and only sample regions of parameter space where real objects are found. Thus, the main uncertainty concerning the applicability of these models stems from how representative the input datasets are of the full range of such emitting regions.

2.3. Abundances and line emission of H II regions

We obtain line ratio relations for H II regions from the sample of Pilyugin & Grebel (2016), which includes 965 observations of H II regions with auroral line measurements and direct-method abundances. We supplement this sample with recent observations of extragalactic H II regions from Croxall et al. (2016) and Toribio San Cipriano et al. (2016), bringing the total sample size to 1052. While all of the H II regions in this sample have measurements of at least one auroral line, some of these auroral-line measurements have low S/N or are otherwise unreliable. In order to construct a representative sample of H II regions with a range of metallicities and ionization parameters, we select a reference sample of high-quality, self-consistent observations from this parent sample using the counterpart method following Pilyugin et al. (2012a).

The counterpart method is a technique for estimating metallicity that is based on the assumption that a set of H II regions with the same physical properties such as density, electron temperature, and chemical abundance will have identical strong-line ratios. A high-quality reference sample of H II regions with reliable auroral measurements can be selected by requiring the auroral-line ratios of an H II region to closely match those of H II regions with similar strong-line ratios, automatically excluding low-S/N measurements and strong outliers. Here, we only use the counterpart method to cull the H II region parent sample of low-quality measurements. All electron temperatures and metallicities are determined using the direct method in our analysis. For the selection of the reference sample, we require the difference between the direct method and counterpart method oxygen and nitrogen abundances to be less than 0.1 dex, and we interpolate over a metallicity interval of 0.2 dex around the metallicity of the closest counterpart when determining the counterpart-method O/H and N/H. After iterating over the parent sample several times, the selection converges, yielding a reference sample of 475 objects that we refer to as the “reference H II region sample.” Objects in this sample have detections of [O II] $\lambda\lambda$ 3726,3729, H β , [O III] λ 5007, H α , [N II] λ 6584, [S II] $\lambda\lambda$ 6716,6731, and at least one of the auroral lines [O III] λ 4363 and [N II] λ 5755. All line fluxes have been corrected for dust reddening.

Electron temperatures are calculated using a five-level atom approximation and up-to-date atomic data (Sanders et al. 2016). For the transition probabilities, we use values from the NIST MCHF database (Fischer & Tachiev 2014) for all ions. We obtain the collision

strengths from Storey et al. (2014) for O III, Hudson & Bell (2005) for N II, and Tayal (2007) for O II. The O II ion is only relevant for the models and galaxy comparison samples since auroral [O II] $\lambda\lambda$ 7320,7330 is not tabulated for the reference H II region sample. The vast majority of the H II region sample has electron densities of $n_e < 200 \text{ cm}^{-3}$ and thus falls in the low density regime where electron temperature calculations are insensitive to the density. We assume an electron density of $n_e = 100 \text{ cm}^{-3}$ for all temperature calculations. Because the five-level atom code is not optimized for speed and we need to calculate electron temperatures many times for each mock galaxy spectrum, we fit analytic formulae to the strong-to-auroral line ratio as a function of temperature obtained from the five-level atom code. Electron temperatures are calculated for a range of line ratios and we fit a function of the form $R = ae^{b/T_e}$, where R is the strong-to-auroral line ratio and T_e is the electron temperature for each ionic species. We obtain the following best-fit equations, which are accurate to $< 1.5\%$ between 5,000 K and 30,000 K:

$$Q3 = 7.892\text{exp}(3.278 \times 10^4 \text{ K}/T_3), \quad (9)$$

$$Q2 = 7.519\text{exp}(1.928 \times 10^4 \text{ K}/T_2). \quad (10)$$

$$Q2N = 7.789\text{exp}(2.493 \times 10^4 \text{ K}/T_2), \quad (11)$$

To infer the electron temperature from an observed line ratio, we invert these expressions.

For objects that have measurements of both [O III] λ 4363 and [N II] λ 5755, T_3 and T_2 are calculated using equations 9 and 11. For objects with a measurement of only one of these auroral lines, we calculate the corresponding ionic temperature and infer the temperature of the other ionic zone assuming the T_2 – T_3 relation of Campbell et al. (1986):

$$T_2 = 0.7T_3 + 3,000 \text{ K}. \quad (12)$$

We note that calculating the oxygen abundance requires T_2 ([O II]), while T_2 ([N II]) is measured for the reference H II region sample because [O II] $\lambda\lambda$ 7320,7330 fluxes were not tabulated. We make the assumption commonly adopted that O II and N II predominantly trace the same ionic zone in the nebula such that T_2 ([O II])= T_2 ([N II]) as expected from photoionization models. We note for completeness that recent observations of H II regions with measurements of both ionic temperatures have shown that this relation has a large dispersion and called the one-to-one correspondence into question (Berg et al. 2015; Croxall et al. 2015, 2016).

Ionic oxygen abundances are calculated using the formulae from Izotov et al. (2006) in the low-density limit:

$$12 + \log(O^+/H^+) = O2 + 5.961 + \frac{1.676}{T_2} - 0.040 \log(T_2) - 0.034T_2, \quad (13)$$

$$12 + \log(O^{++}/H^+) = O3 + 6.200 + \frac{1.251}{T_3} - 0.55 \log(T_3) - 0.014T_3. \quad (14)$$

Total oxygen abundance is calculated assuming the fraction of oxygen in higher ionic and neutral states is neg-

ligible (Izotov et al. 2006; Pilyugin et al. 2012a):

$$\frac{O}{H} \approx \frac{O^+}{H^+} + \frac{O^{++}}{H^+}. \quad (15)$$

In order to create a distribution of realistic H II regions with known metallicities in a mock galaxy, we first need to parameterize the strong line ratios of the observed H II region sample because calculating direct-method metallicities requires the strong-line ratios O2 and O3. Since we are interested in biases in abundance measurements, an obvious choice of parameter is the oxygen abundance. However, because the direct-method oxygen abundance calculation depends on the strong line ratios O3 and O2, parameterizing by O/H will introduce covariances that are not observed in real H II region samples. We instead parameterize the strong line ratios as a function of T_3 , which has no dependence on the strong-line ratios and is a good proxy for the oxygen abundance since the relationship between T_3 and $12+\log(O/H)$ is nearly linear over the range of metallicities of interest here, as shown in Figure 1. Figure 2 presents the strong line ratios O3, O2, N2, and S2 as a function of T_3 for the reference H II region sample. For each line ratio, we find the median relation in bins of T_3 and fit polynomials to the median points to obtain functional forms of these relations:

$$O3 = -16.6 \log(T_3)^3 + 189 \log(T_3)^2 - 711 \log(T_3) + 884, \quad (16)$$

$$O2 = -5.89 \log(T_3)^2 + 46.8 \log(T_3) - 92.8, \quad (17)$$

$$N2 = -5.48 \log(T_3)^2 + 40.3 \log(T_3) - 73.9, \quad (18)$$

$$S2 = -2.67 \log(T_3)^2 + 20.5 \log(T_3) - 38.3. \quad (19)$$

In Figure 2, the points in the right three panels are color coded by O3. It is apparent that at fixed T_3 , each of these low-ionization line ratios is anticorrelated with O3. This anticorrelation encodes the range of ionization parameters at fixed T_3 : higher ionization parameter H II regions have higher O3 and lower low-ionization line ratios (N2, O2, and S2) at fixed T_3 . We include variations in ionization parameter in our models by encoding ionization parameter changes using ΔX , the difference in line ratio X between the data point and the best-fit polynomial at fixed T_3 . We subtract the best-fit polynomials from the data shown in the right three panels of Figure 2 and fit linear functions with y-intercept of zero to $\Delta O2$, $\Delta N2$, and $\Delta S2$, all as a function of $\Delta O3$. In this way, we obtain fits with the following values:

$$\Delta O2 = -0.47\Delta O3 \quad (20)$$

$$\Delta N2 = -0.42\Delta O3 \quad (21)$$

$$\Delta S2 = -0.56\Delta O3 \quad (22)$$

Thus, the residuals of the O3 fit, $\Delta O3$, are used as input for the low-ionization line ratios. The standard deviation of the O3 residuals is 0.14 dex and is independent of T_3 . Adding the ionization parameter (i.e., $\Delta O3$) terms to the best-fit polynomials yields good fits to the data, with

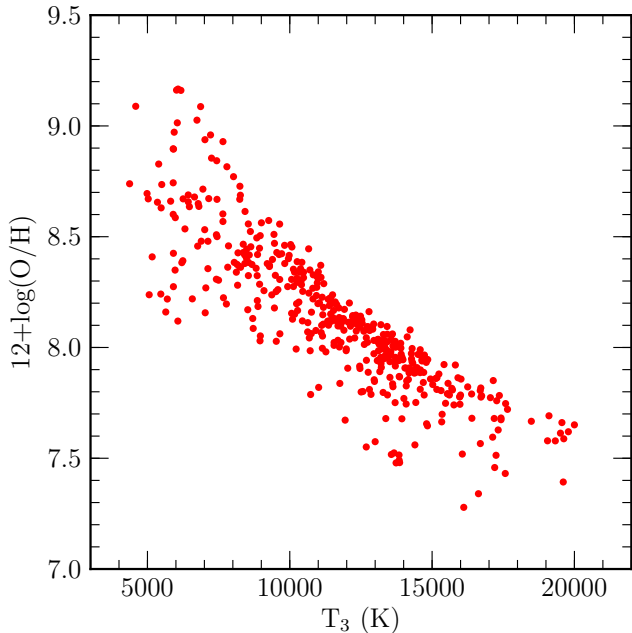


Figure 1. Direct-method $12+\log(\text{O}/\text{H})$ vs. T_3 for the 475 individual H II regions in the reference H II region sample. Metallicities are calculated using up-to-date atomic data. $12+\log(\text{O}/\text{H})$ is nearly linearly dependent on T_3 , which provides a good proxy for the direct-method metallicity.

residuals having standard deviations of $\lesssim 0.15$ dex for O2, N2, and S2. We note that the measurement uncertainty in T_3 is the main source of uncertainty in Figure 2, and accounts for some of the scatter about these fits. The solid lines in Figure 2 show contours of constant O3 based on the combination of the polynomial fits and ionization parameter terms presented above. These analytic functions represent the relationships between strong-line ratios and T_3 well for observed H II regions.

These formulae allow us to obtain realistic strong-line ratios for H II regions using input T_3 distributions. The strong-line emission from mock H II regions is combined with strong-line emission from DIG in order to produce global galaxy strong-line ratios that are a necessary component for the calculation of direct-method metallicity inferred from global galaxy spectra. We also investigate the impact of DIG emission and flux-weighted combination effects on diagnostic strong-line ratio diagrams and strong-line metallicity indicators. Additionally, we test whether our models simultaneously match the position of real galaxies in multiple strong-line ratio diagrams, a requirement for any realistic model of galaxy line emission.

2.4. Line emission from diffuse ionized gas

The models presented herein include emission from DIG, in addition to line emission from multiple H II regions with varying abundances, for the first time. It is of critical importance to account for DIG emission when studying emission-line spectra of local star-forming galaxies since $\sim 30 - 60\%$ of $\text{H}\alpha$ emission in local spiral galaxies can be attributed to DIG (Zurita et al. 2000; Oey et al. 2007). Because of the diffuse nature of DIG, its line emission has a low surface brightness compared to that of H II regions and is thus difficult to observe. DIG was first identified with the discovery of a layer of

warm ionized hydrogen permeating the Milky Way ISM (i.e., the Reynolds Layer; Reynolds et al. 1973). Initial observations of DIG line ratios in other galaxies have come from longslit spectroscopy of extra-planar emission around edge-on galaxies (e.g., Otte et al. 2001, 2002) or of low-surface-brightness emission in face-on galaxies probing only a small number of DIG regions (e.g., Hoopes & Walterbos 2003). These observations showed that low-ionization line ratios (N2, S2) of DIG are enhanced relative to those typical of H II regions, but sample sizes were too small to establish DIG line ratio trends over a range of physical conditions.

2.4.1. MaNGA observations of DIG line ratios

In order to estimate DIG contribution to line emission in local star-forming galaxy spectra with a wide range of stellar masses and metallicities, we need to characterize DIG line ratios over a wide range of excitation levels throughout star-forming disks and tie DIG line ratios in a galaxy to the H II region abundances in the same galaxy in some realistic way. To achieve this task, we characterize the DIG emission line ratios using data from the SDSS-IV Mapping Nearby Galaxies at APO (MaNGA; Bundy et al. 2015; Yan et al. 2016; Law et al. 2016) integral field spectroscopic (IFS) survey. The MaNGA IFS dataset provides spatially-resolved spectroscopic observations of a large number of local star-forming galaxies for which such an analysis of DIG emission is possible (Zhang et al. 2017).

Zhang et al. (2017) recently showed how optical strong emission-line ratios in local galaxies vary with $\text{H}\alpha$ surface brightness ($\Sigma_{\text{H}\alpha}$), with the strength of low ionization lines ($[\text{N II}]$, $[\text{S II}]$, $[\text{O II}]$, and $[\text{O I}]$) relative to Balmer lines increasing with decreasing $\Sigma_{\text{H}\alpha}$ at fixed radius. However, Zhang et al. also found that O3 did not increase or decrease with $\Sigma_{\text{H}\alpha}$ on average. Under the assumption that high- $\Sigma_{\text{H}\alpha}$ regions are dominated by H II region emission and DIG emission becomes increasingly important as $\Sigma_{\text{H}\alpha}$ decreases, this result indicates that the O3 ratios of DIG and H II regions are the same on average within a single galaxy. Thus, we can match a sample of model H II regions with DIG emitting regions in a way that mimics the ISM of real galaxies by matching in O3. We note that Zhang et al. (2017) found some stellar mass dependence for ΔO3 vs. $\Delta\Sigma_{\text{H}\alpha}$, such that DIG O3 is higher than that of H II regions in the most massive third of their sample. We do not include this stellar mass effect in our models because we have no direct way of assigning stellar mass to a mock galaxy, but this effect could be included in future models to increase the accuracy of the DIG representation.

In order to realistically match model distributions of DIG and H II regions, we characterize the DIG excitation sequences of $[\text{N II}]/\text{H}\alpha$, $[\text{S II}]/\text{H}\alpha$, $[\text{O II}]/\text{H}\beta$, and $[\text{O III}]/\text{H}\beta$ as a function of O3N2. We utilize the sample of galaxies from SDSS Data Release 13 (SDSS Collaboration et al. 2016) presented in Zhang et al. (2017). From their sample of 365 blue, low-inclination galaxies, we selected a sample of 266 star-forming galaxies by requiring that the central region does not host an AGN according to the demarcation of Kauffmann et al. (2003) in the $[\text{O III}]/\text{H}\beta$ vs. $[\text{N II}]/\text{H}\alpha$ diagram. In order to determine the line ratios of the central region of a galaxy, we construct a $3''$ pseudo-fiber by summing the line fluxes

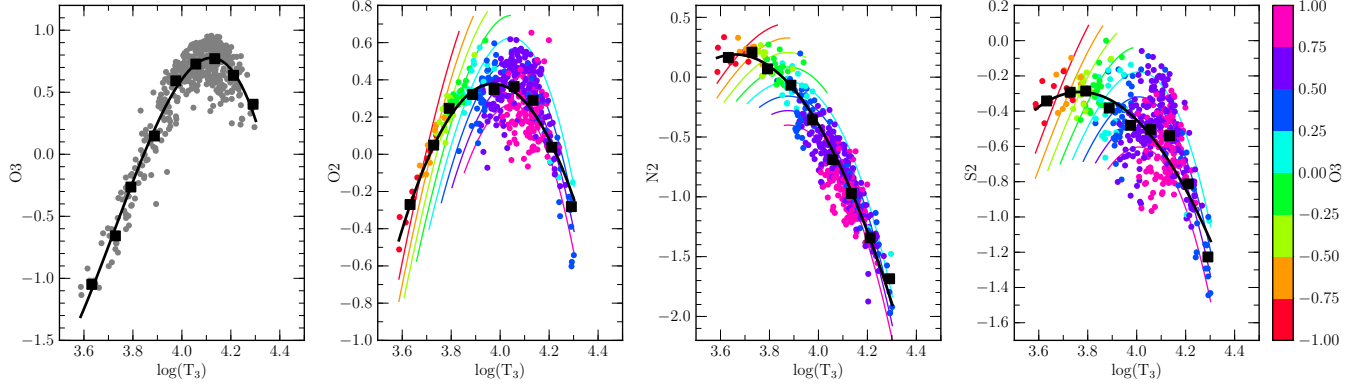


Figure 2. Strong-line ratios O3, O2, N2, and S2 as a function of T_3 for the reference H II region sample. In each panel, black squares display the median strong-line ratio in bins of T_3 . The black lines show best-fit polynomials to the median points presented in equations 16–19. In the right three panels, the points are color-coded according to O3. The anticorrelation between O3 and O2, N2, and S2 at fixed T_3 reflects ionization parameter dependence in the strong-line ratio vs. T_3 relations. The solid colored lines display contours of constant O3 according to the analytic parameterization of ionization parameter presented in equations 20–22. Mock H II region distributions are drawn from the analytic functional fits presented here, including the secondary ionization parameter dependence.

of all spaxels within a $1.5''$ radius of the galaxy center. This pseudo-fiber mimics the aperture of an SDSS fiber, matching the observations upon which the Kauffmann et al. (2003) demarcation are based.

For each galaxy in the DIG galaxy sample, we select all spaxels that have a signal-to-noise ratio $S/N \geq 3$ for $[\text{O II}]\lambda\lambda 3726, 3729$, $\text{H}\beta$, $[\text{O III}]\lambda 5007$, $\text{H}\alpha$, $[\text{N II}]\lambda 6584$, and $[\text{S II}]\lambda\lambda 6716, 6731$. We assume that the highest $\Sigma_{\text{H}\alpha}$ spaxels are dominated by H II region emission, while the lowest $\Sigma_{\text{H}\alpha}$ spaxels are dominated by DIG emission. We identify spaxels with $\Sigma_{\text{H}\alpha}$ below the 10th percentile of the $\Sigma_{\text{H}\alpha}$ distribution in each galaxy as DIG-dominated. The threshold of 10% was selected in order to provide the purest probe of DIG emission while still yielding a large sample of spaxels. Results do not change significantly when varying this threshold from 5% to 15%. The DIG-dominated spaxel sample can be thought of as the diffuse analog of the H II region sample. Before calculating $[\text{O II}]/\text{H}\beta$, the $[\text{O II}]$ and $\text{H}\beta$ fluxes are first corrected for reddening on a spaxel-by-spaxel basis assuming the attenuation law of Cardelli et al. (1989) and an intrinsic ratio of $\text{H}\alpha/\text{H}\beta = 2.86$. The line ratios $[\text{O III}]/\text{H}\beta$, $[\text{N II}]/\text{H}\alpha$, and $[\text{S II}]/\text{H}\alpha$ are calculated without correcting for dust reddening given the close proximity in wavelength of the relevant emission lines.

We construct the DIG strong-line excitation sequences by taking the median line ratios of the DIG spaxel sample in bins of O3N2. We chose to bin in O3N2 rather than O3 because O3N2 monotonically increases with T_3 in a nearly linear fashion for the reference H II region sample, while O3 is double-valued as a function of T_3 . We assume that O3 of DIG regions is also double-valued as a function of T_3 , in which case the median relation in bins of O3 would not be a good representation of the actual excitation sequence in the regime where the temperature-dependence of O3 weakens. While there are no constraints on the electron temperatures of DIG, we work under the assumption that DIG electron temperature decreases with increasing metallicity as for H II regions. Binning excitation sequences and matching H II and DIG regions in O3N2 instead of O3 alone is also motivated by the fact that the sequences of H II regions, $z \sim 0$ star-forming galaxies, and DIG regions are nearly identical in the $[\text{O III}]/\text{H}\beta$ vs. $[\text{N II}]/\text{H}\alpha$ diagram as

shown below in Section 2.4.2, in agreement with the results of Zhang et al. (2017) that O3 and N2 are minimally affected by DIG compared to other strong-line ratios. The DIG line ratio distributions and median excitation sequences in the $[\text{O III}]/\text{H}\beta$ vs. $[\text{N II}]/\text{H}\alpha$, $[\text{O III}]/\text{H}\beta$ vs. $[\text{S II}]/\text{H}\alpha$, and $[\text{O III}]/\text{H}\beta$ vs. $[\text{O II}]/\text{H}\beta$ diagrams are presented in Figure 3, which we refer to as the O3N2, O3S2, and O3O2 diagrams, respectively. For comparison, the median line ratios of the reference H II region sample in bins of T_3 are shown. As implied by the results of Zhang et al. (2017), we find that at fixed O3, DIG regions display larger low-ionization line ratios than those of H II regions.

2.4.2. Extrapolations of DIG excitation sequences

We note that the reference H II region sample spans a wide range of excitation levels with $-1.0 \lesssim \text{O3} \lesssim 1.0$, while the DIG spaxel sample only has sufficient statistics over a smaller range ($-0.6 \lesssim \text{O3} \lesssim 0.4$). This limitation in the range of DIG excitation levels stems from the nature of the MaNGA sample used here, which mostly comprises moderate-metallicity galaxies leaving the low- and high-metallicity tails of the distribution poorly sampled. The dearth of low-O3 DIG measurements is also present due to the trend observed by Zhang et al. (2017) in which DIG O3 is higher than H II region O3 on average in massive ($\log(M_*/M_\odot) > 10.08$) star-forming galaxies. Once the survey is completed, the full MaNGA sample will contain ~ 10 times more galaxies than were available at the time of this study, which should allow for direct constraints of the metal-rich and metal-poor tails of the DIG excitation sequences. To allow our models to be applicable for galaxies over a wide range of metallicities, we extend the DIG excitation sequences by making assumptions about the behavior of DIG line ratios in the low- and high-metallicity tails based on the position of H II regions and $z \sim 0$ SDSS galaxies in strong-line excitation diagrams.

In order to compare the positions of galaxies and H II regions in line ratio diagrams, we select a comparison sample of $z \sim 0$ star-forming galaxies from SDSS Data Release 7 (DR7; Abazajian et al. 2009) for which strong-line measurements are available. We take global galaxy properties and emission-line measurements from

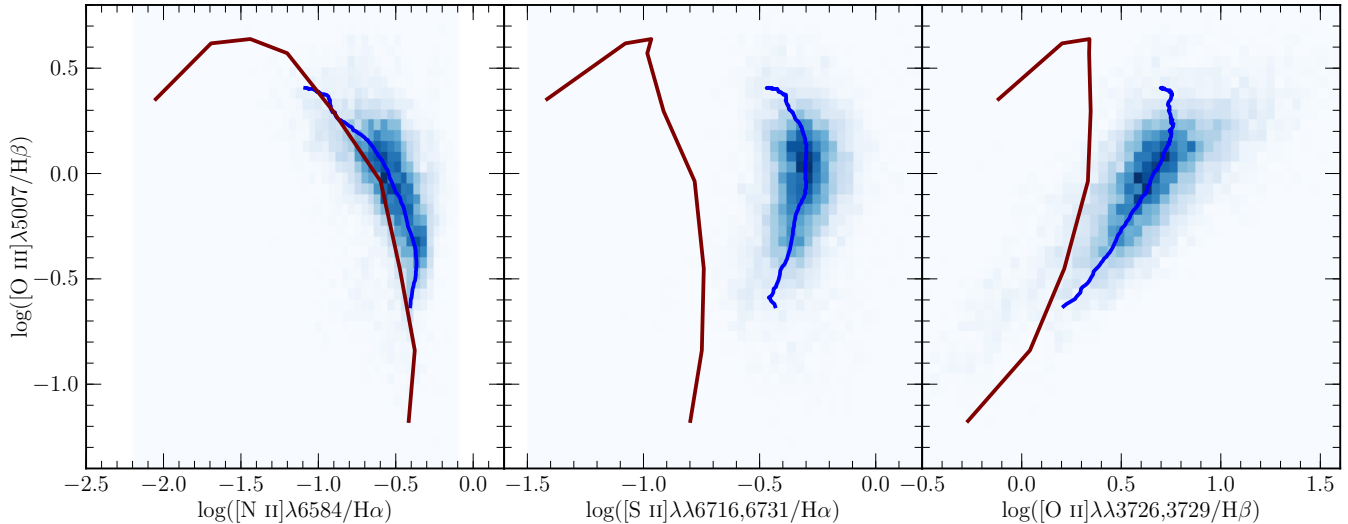


Figure 3. The O3N2 (left), O3S2 (middle), and O3O2 (right) strong-line ratio diagrams for DIG-dominated spaxels from MaNGA galaxies (Zhang et al. 2017). The blue two-dimensional histogram shows the distribution of strong-line ratios for the 10% lowest surface-brightness spaxels for each galaxy in the DIG galaxy sample. These spaxels are dominated by emission from DIG rather than H II regions. The running median of the DIG spaxel distribution in bins of O3N2 is displayed as a solid blue line. The maroon line shows the median strong-line excitation sequences of the reference H II region sample in bins of T_3 .

the MPA-JHU SDSS DR7 catalogs.³ We use the same selection criterion employed by Andrews & Martini (2013), and later compare our models to their stacks of SDSS galaxies constructed from this sample of individual star-forming galaxies. We require SDSS galaxies to have $0.027 \leq z \leq 0.25$ and $S/N \geq 5$ for each of the lines $H\beta$, $H\alpha$, and $[N II]\lambda 6584$. AGN are rejected by requiring $\log([N II]\lambda 6584/H\alpha) < -0.4$ as well as a location below the star-forming/AGN demarcation of Kauffmann et al. (2003) in the $[O III]\lambda 5007$ vs. $[N II]\lambda 6584/H\alpha$ diagram when $S/N \geq 3$ for $[O III]\lambda 5007$. This selection yields a sample of 209,513 local star-forming galaxies with a median redshift of $z_{\text{med}} = 0.08$, which we refer to as the “SDSS strong-line comparison sample.”⁴ Before calculation of the line ratios, the emission-line fluxes were corrected for reddening using the attenuation law of Cardelli et al. (1989), assuming an intrinsic Balmer decrement of $H\alpha/H\beta = 2.86$. In line-ratio diagrams involving $[O II]\lambda\lambda 3726, 3729$, $[O III]\lambda 5007$, or $[S II]\lambda\lambda 6716, 6731$, only the subset of galaxies with $S/N \geq 3$ in the relevant emission lines are plotted.

The excitation sequences of H II regions and $z \sim 0$ SDSS star-forming galaxies in the O3N2, O3S2, and O3O2 diagrams are presented in Figure 4. These plots demonstrate the necessity of including DIG emission in order to properly interpret SDSS star-forming galaxy line ratios. In the O3N2 diagram, H II regions and SDSS galaxies follow nearly identical sequences, suggesting that the DIG O3N2 sequence is similar to that of H II regions, as observed in the DIG line ratios from MaNGA data (Zhang et al. 2017). In the O3S2 and O3O2 diagrams, SDSS galaxies are offset towards significantly

higher $[S II]/H\alpha$ and $[O II]/H\beta$ at fixed $[O III]/H\beta$ compared to H II regions, suggesting that the galaxy spectra contain a significant DIG contribution based on the observed DIG line ratio relations in Figure 3. The interpretation that DIG is largely responsible for the offset between H II regions and SDSS galaxies in these diagrams is supported by the observation of Masters et al. (2016) that SDSS galaxies display a dependence on $H\alpha$ surface-brightness ($\Sigma_{H\alpha}$) perpendicular to these excitation sequences, such that those galaxies with the lowest $\Sigma_{H\alpha}$ are offset farthest from the H II region sequences. Under the assumption that DIG accounts for a larger fraction of line emission in galaxies with lower $\Sigma_{H\alpha}$ (Oey et al. 2007), the results of Masters et al. imply that DIG emission is most important in those galaxies farthest offset from the H II region sequences, while galaxies with large $\Sigma_{H\alpha}$ and highly-concentrated star formation appear more similar to H II regions in these line ratio spaces.

In the O3S2 diagram, H II regions and SDSS galaxies show the largest offset at moderate excitation ($[O III]/H\beta \sim 0$) where the DIG $[S II]/H\alpha$ reaches a maximum. Above and below this point, the H II region and SDSS sequences appear to converge suggesting that the DIG line ratios become similar to H II region line ratios in the low- and high-excitation tails. A similar behavior is observed in the O3O2 diagram, where the H II regions and SDSS galaxies converge at the lowest and highest metallicities. We therefore adopt simple linear extrapolations of the DIG excitation sequences that approach the point of convergence of H II regions and SDSS galaxies at both high and low metallicities. This behavior is consistent with the turnover in DIG $[N II]/H\alpha$ and $[S II]/H\alpha$ at moderate $[O III]/H\beta$ observed in the data. The adopted extrapolations are shown as blue dashed lines in Figure 4. It is possible that these linear extrapolations are not accurate representations of the DIG excitation sequences, however the relative locations of the H II region and SDSS sequences suggest these extrapolations provide a good approximation. The region of largest uncertainty

³ Available online at <http://www.mpa-garching.mpg.de/SDSS/DR7>

⁴ Andrews & Martini additionally rejected galaxies for which the SDSS photometric flags indicated that the spectroscopic fiber targeted the outskirts of a large galaxy instead of a galaxy center, and removed low-mass targets for which the stellar mass was obviously incorrect through visual inspection. We do not apply these additional criteria since such issues affect less than 0.5% of the sample.

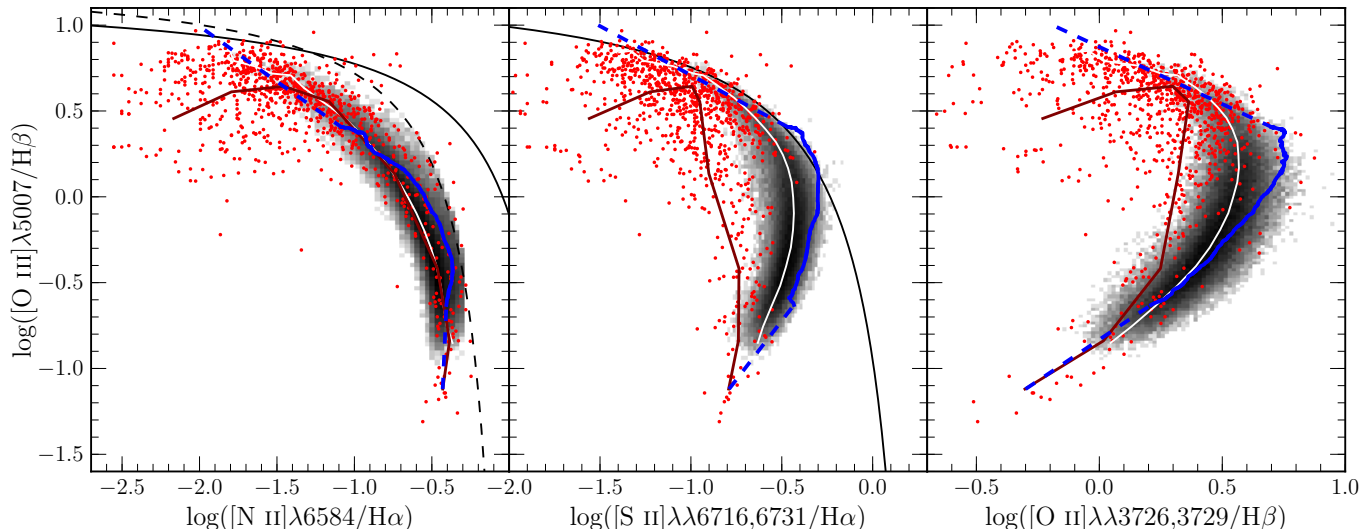


Figure 4. Excitation sequences of H II regions, SDSS star-forming galaxies, and DIG regions in the O3N2 (left), O3S2 (middle), and O3O2 (right) diagrams. The gray two-dimensional histogram shows the distribution of $z \sim 0$ star-forming galaxies from the strong-line comparison sample, where the white line represents the running median of the galaxies in bins of O3N2. Individual H II regions in the reference H II region sample are represented by red points, where the maroon line gives the running median of the H II regions. The solid blue line shows the running median of the DIG-dominated spaxels from the MaNGA DIG galaxy sample in bins of O3N2, while the dashed blue lines denote the linear extrapolations that we assume for the DIG excitation sequences. In the left and middle panels, the solid black line shows the “maximum-starburst” line of Kewley et al. (2001), while the empirical demarcation between AGN and star-forming galaxies of Kauffmann et al. (2003) is displayed as the black dashed line in the left panel.

is the extreme metal-poor regime in which the H II region sequences turn over in $[\text{O III}]/\text{H}\beta$ while the DIG sequence extrapolations continue increasing in $[\text{O III}]/\text{H}\beta$. Zhang et al. (2017) demonstrated that $[\text{O III}]/\text{H}\beta$ of DIG and H II regions is the same on average at fixed galactocentric radius for the least-massive third of their sample ($\log(M_*/M_\odot) < 9.43$), suggesting an agreement between DIG and H II region $[\text{O III}]/\text{H}\beta$ in low-metallicity environments. However, the MaNGA survey only targeted galaxies with $\log(M_*/M_\odot) \gtrsim 9.0$ that do not have low enough stellar masses to populate the extreme low-metallicity tail. The nature of DIG line ratios in this regime therefore cannot be directly constrained. It is possible that the DIG sequences also turn over like the H II region sequences, but this uncertainty only affects a regime where a small fraction of SDSS galaxies lie, and will therefore minimally impact our results.

The low- and high-metallicity convergence of the SDSS and H II region sequences could also arise from a changing DIG contribution with metallicity, such that emission line contribution from DIG is largest at moderate metallicity and is small at low and high metallicities. In this case, the DIG line ratios need not converge with the galaxy and H II region line ratios in either extreme regime. However, individual SDSS galaxies do not show any evidence for a strong dependence of the fractional DIG contribution on O3 or M_* (see Section 3.1 below), disfavoring an explanation based on a dynamic level of DIG contribution.

2.5. Model framework

We create the individual line-emitting components of mock galaxies using the line-ratio relations of H II and DIG regions described above, and construct fake global galaxy spectra by combining light from the individual components in a manner that mimics the ISM structure of real galaxies. Below we describe the methodology used

to create one mock galaxy spectrum, which is repeated many times using a range of input parameters to build up a statistical sample of mock galaxies.

First, we begin with a population of H II regions. As described in Section 2.3, the strong line ratios are parameterized by the electron temperature T_3 , and thus the oxygen abundance is primarily a function of T_3 in the models. We produce a population of H II regions by randomly selecting N_{HII} samples from an input distribution of T_3 . We adopt a log-normal shape for this T_3 distribution, in which the free parameters are the central temperature T_{cent} and the logarithmic width σ_T . A log-normal distribution is observationally motivated by the distributions of T_3 and T_2 of individual H II regions in local star-forming spirals. These distributions are shown in Figure 5 using data from three galaxies in the CHAOS survey (Berg et al. 2015; Croxall et al. 2015, 2016). The central temperature T_{cent} is representative of the characteristic metallicity of the galaxy star-forming regions, while the width of the distribution σ_T corresponds to the range of metallicities spanned by individual H II regions. The CHAOS galaxies are characterized by $\sigma_T = 0.03 - 0.08$ dex. We note that a log-normal distribution has symmetric wings in $\log(T)$, but the CHAOS galaxies display high-temperature wings, with no corresponding low-temperature wings. This absence is likely an observational bias because of the exponential decline in auroral line strength with decreasing temperature, supported by the fact that the lowest-temperature measurements in each CHAOS galaxy tend to fall only just above the $S/N \geq 3$ cut on auroral line strength.

We obtain the strong-line ratios for the H II regions using the T_3 distribution as input to equations 16-19. We add an ionization parameter term to these median relations by assigning ΔO3 to each mock H II region by randomly drawing from a normal distribution with a mean of zero and a standard deviation of 0.14 dex,

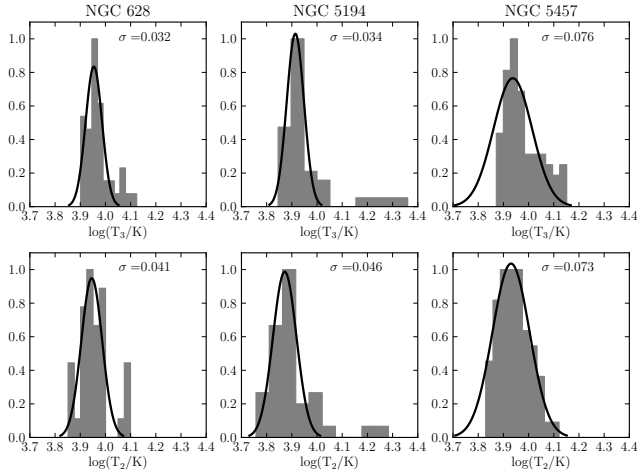


Figure 5. T_3 and T_2 distributions of individual H II regions within the local spiral galaxies NGC 628 (Berg et al. 2015), NGC 5194 (Croxall et al. 2015), and NGC 5457 (Croxall et al. 2016). Black lines show log-normal fits to the electron temperature distribution in each panel, where the best-fit width of the log-normal is given in the upper right corner.

equal to the observed scatter about the median in the O3 vs. T_3 diagram for the reference H II region sample. $\Delta O2$, $\Delta N2$, and $\Delta S2$ are then calculated for each mock H II region using equations 20-22. The final strong-line ratios for each mock H II region are obtained by adding $\Delta O3$, $\Delta O2$, $\Delta N2$, and $\Delta S2$ to the O3, O2, N2, and S2 values obtained from the polynomial fits of equations 16-19. Each of these strong-line ratios has $H\beta$ as the denominator, so we assume an H II region $H\beta$ flux distribution in order to obtain the strong-line fluxes. For simplicity, we assign the same $H\beta$ flux to each H II region. This assumption does not affect our results because $H\beta$ flux does not show any dependence on either T_3 or $12+\log(O/H)$ in the CHAOS H II regions on a galaxy-by-galaxy basis, suggesting that the brightness of an H II region does not depend on its abundance properties (Berg et al. 2015; Croxall et al. 2015, 2016). Thus, using a distribution of $H\beta$ fluxes is simply a source of scatter but has no systematic effect on any of our results. The combination of strong-line ratios and $H\beta$ fluxes yields the intrinsic fluxes of $[O II]\lambda\lambda 3726, 3729$, $H\beta$, $[O III]\lambda\lambda 4959, 5007$, $[N II]\lambda\lambda 6548, 6584$, and $[S II]\lambda\lambda 6716, 6731$ for each H II region. The $H\alpha$ flux is obtained assuming an intrinsic ratio of $H\alpha/H\beta = 2.86$. We then combine the $[O III]\lambda\lambda 4959, 5007$ and $[O II]\lambda\lambda 3726, 3729$ fluxes with the T_3 values to produce the intrinsic fluxes of the auroral lines $[O III]\lambda 4363$ and $[O II]\lambda\lambda 7320, 7330$ using equations 9 and 10.

The emission lines from each individual H II region are then reddened. The $E(B-V)$ values of individual H II regions in the CHAOS sample do not correlate with T_3 or $12+\log(O/H)$ on a galaxy-by-galaxy basis, suggesting that using a random $E(B-V)$ assuming some distribution shape is appropriate. For each H II region, we draw an $E(B-V)$ value from a normal distribution with a width of 0.15 magnitudes, with negative $E(B-V)$ values set to zero. The $E(B-V)$ distributions of the CHAOS H II regions suggest that this shape and width is appropriate for local star-forming spirals. While individual H II region $E(B-V)$ shows no correlation with metallicity, $E(B-V)^{gal}$ inferred from the global galaxy spectrum does correlate

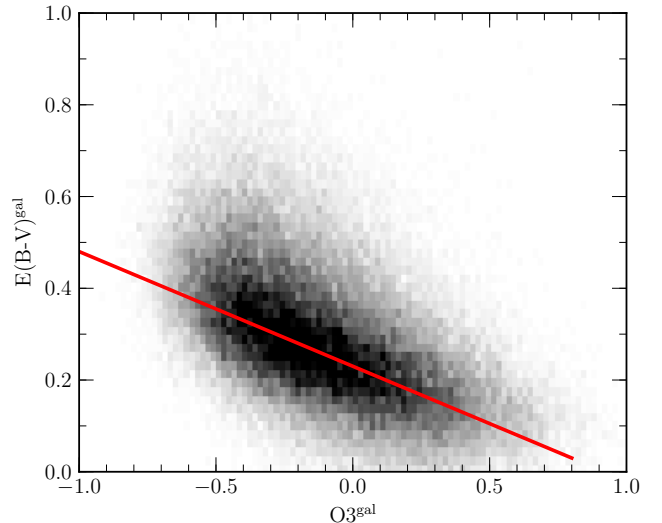


Figure 6. $E(B-V)^{gal}$ as a function of $O3^{gal}$ for the SDSS strong-line comparison sample. The amount of reddening increases with increasing metallicity and decreasing excitation, as represented by decreasing $O3^{gal}$. The red line shows the linear representation of this relationship, given by $E(B-V)^{gal} = -0.25 \times O3^{gal} + 0.23$.

with global galaxy properties such as $O3^{gal}$, the O3 ratio inferred from global galaxy spectra, as shown in Figure 6 for the strong-line comparison sample. The anticorrelation between $E(B-V)^{gal}$ and $O3^{gal}$ suggests that the center of the $E(B-V)$ distribution for the H II regions depends on the characteristic metallicity of the galaxy, reflecting the relationship between galaxy reddening and chemical enrichment (Heckman et al. 1998). We adopt a linear representation of the data in Figure 6, and use the median O3 of the simulated H II regions to set the center of the $E(B-V)$ distribution using this linear relation. We note that the relationship shown in Figure 6 is derived from the global galaxy ratio $O3^{gal}$, which we later conclude is biased with respect to the median H II region ratio $O3^{HII}$. Iteratively including this bias in the $E(B-V)$ relation changes the central $E(B-V)$ values by < 0.04 magnitudes, which has no impact on our results. We redden the strong and auroral line fluxes from each modeled H II region individually using its assigned $E(B-V)$, assuming the attenuation law of Cardelli et al. (1989).

We produce a number of DIG regions equal to the number of H II regions, and each DIG region is associated with an H II region. DIG emission is observed to be spatially correlated with H II regions (Zurita et al. 2000) and the diffuse gas immediately surrounding an H II region likely has a similar metallicity to that of the gas in that H II region. Each DIG region is assigned the same $O3N2$ value as its associated H II region. While the results of Zhang et al. (2017) suggest that DIG and H II region O3 is the same on average, O3 is double-valued as a function of electron temperature and metallicity and thus does not provide a good parameterization of these properties, as described in Section 2.4 above. If we matched DIG and H II regions in O3, the double-valued nature of the line ratio would make it unclear how to match DIG and H II regions in the regime where O3 vs. T_3 is flat. We instead match in $O3N2$, which increases monotonically with increasing T_3 for H II regions. Matching in $O3N2$ instead of O3 alone should still provide a realistic way of associating DIG and H II regions based on the

close agreement of the DIG and H II region sequences in the O3N2 diagram and on the result of Zhang et al. (2017) that the systematic difference between H II and DIG region N2 is small. Given O3N2, the strong-line ratios O3, N2, S2, and O2 of each DIG region are assigned using the DIG excitation sequences shown in Figure 4. We use the running median of the DIG sequences if $-0.6 < \log([\text{O III}]\lambda 5007/\text{H}\beta) < 0.4$ and use the linear extrapolations of the DIG sequences otherwise.

The DIG fraction, f_{DIG} , is defined as the fraction of the total intrinsic Balmer line flux of the galaxy that originates from DIG. The $\text{H}\alpha$ and $\text{H}\beta$ line fluxes of each DIG region are assigned such that the intrinsic DIG Balmer line fluxes account for the fraction f_{DIG} of the combined intrinsic Balmer line flux of the H II and DIG region. The same f_{DIG} is used for each H II -DIG region pair in a single mock galaxy. The $[\text{O III}]\lambda\lambda 4959, 5007$, $[\text{N II}]\lambda\lambda 6548, 6584$, $[\text{S II}]\lambda\lambda 6716, 6731$, and $[\text{O II}]\lambda\lambda 3726, 3729$ fluxes are then calculated using the strong-line ratios and Balmer line fluxes. In order to calculate the auroral line fluxes of the DIG regions, we need the DIG electron temperatures T_3 and T_2 . However, there are no observational constraints on the electron temperature of DIG because of its low surface brightness and the intrinsic weakness of the auroral lines. We initially assume that the electron temperatures T_3 and T_2 of each DIG region are equal to the electron temperatures of the associated H II region, but we reevaluate this assumption in Section 3.1 below. With the assumed DIG T_3 and T_2 , the intrinsic DIG auroral-line fluxes $[\text{O III}]\lambda 4363$ and $[\text{O II}]\lambda\lambda 7320, 7330$ are calculated using equations 9 and 10. The line fluxes of each DIG region are then reddened assuming the same extinction as the associated H II region.

The global galaxy spectrum is produced by summing the reddened flux from each H II and DIG region on a line-by-line basis for $[\text{O II}]\lambda\lambda 3726, 3729$, $[\text{O III}]\lambda 4363$, $\text{H}\beta$, $[\text{O III}]\lambda\lambda 4959, 5007$, $[\text{N II}]\lambda 5755$, $\text{H}\alpha$, $[\text{N II}]\lambda\lambda 6548, 6584$, $[\text{S II}]\lambda\lambda 6716, 6731$, and $[\text{O II}]\lambda\lambda 7320, 7330$. We then analyze the global galaxy spectrum as if it were real global galaxy spectroscopic data. The global line fluxes are corrected for reddening using the summed $\text{H}\alpha$ and $\text{H}\beta$ fluxes assuming an intrinsic ratio $\text{H}\alpha/\text{H}\beta = 2.86$ and the attenuation law of Cardelli et al. (1989). The strongline ratios are calculated using the dereddened global line fluxes.

The global electron temperatures are calculated from the global dereddened strong-to-auroral line ratios using equations 9 and 10, and global direct-method oxygen abundances are calculated using equations 13 and 14. We calculate global $12+\log(\text{O}/\text{H})$ under three assumptions: (1) both $[\text{O III}]\lambda 4363$ and $[\text{O II}]\lambda\lambda 7320, 7330$ are detected, (2) only $[\text{O III}]\lambda 4363$ is detected, and (3) only $[\text{O II}]\lambda\lambda 7320, 7330$ is detected. We refer to the three metallicities as $12+\log(\text{O}/\text{H})_{T_2, T_3}$, $12+\log(\text{O}/\text{H})_{T_3}$, and $12+\log(\text{O}/\text{H})_{T_2}$, respectively. In cases 2 and 3, the unknown electron temperature is estimated from the known electron temperature using equation 12. These three oxygen abundance values will be useful for comparing with different real datasets since it is not uncommon for only one of the auroral oxygen lines to be detected in galaxy spectra, even in stacks.

The process described above is repeated many times while varying T_{cent} in order to build up a statistical sample of mock galaxy spectra, allowing us to average over

sources of scatter to find median trends. In order to quantify the bias between the distribution of H II region properties and the global properties as inferred from the galaxy spectrum, for each line ratio or physical property we save both the global value inferred from the galaxy spectrum and the median value of the distribution of individual H II regions for every mock galaxy. Properties derived from the global galaxy spectra will be indicated with the superscript “gal,” while median properties of the H II region distribution will be denoted by the superscript “HII.”

There are only four free parameters in these models. These free parameters are the number of H II regions per galaxy, N_{HII} , the central temperature of the H II region T_3 distribution, T_{cent} , the width of the H II region T_3 distribution, σ_T , and the fraction of intrinsic Balmer flux originating from DIG emission, f_{DIG} . In practice, σ_T and f_{DIG} are set to observationally-motivated values appropriate for the real dataset being modeled, while T_{cent} is freely varied to produce galaxies with a range of metallicities. The value of N_{HII} determines how well the T_3 distribution is sampled, and thus simply corresponds to a source of scatter if N_{HII} is small, but does not change any trends.

3. COMPARISON DATASETS AND FIDUCIAL MODELS

We compare our models to observations of local star-forming galaxies in order to verify that the mock galaxy spectra produced following the methodology of Section 2.5 resemble spectra of real galaxies. Auroral emission lines are detected for a few hundred individual SDSS galaxies (Izotov et al. 2006; Pilyugin et al. 2010), and we assemble a sample of such galaxies for comparison in Section 3.2. However, samples of individual SDSS galaxies for which auroral lines are detected are not representative of typical star-forming galaxies from which the $z \sim 0$ MZR is constructed, generally having much higher SFR at fixed M_* than average and sampling only the low-mass, low-metallicity tail of the local population. Auroral line measurements across a wide dynamic range of galaxy properties have been obtained by stacking SDSS spectra (Andrews & Martini 2013; Brown et al. 2016; Curti et al. 2017), providing a comparison sample that is more representative than samples of individual galaxies with auroral line detections. We therefore focus primarily on constructing models representing typical $z \sim 0$ star-forming galaxies. We compare these models to the SDSS stacks from Andrews & Martini (2013), Brown et al. (2016), and Curti et al. (2017) (hereafter AM13, B16, and C17, respectively), and quantify biases in metallicity measurements made from global galaxy spectra. The electron temperatures and oxygen abundances for all comparison samples are calculated using the same methods as for the mock galaxy spectra, outlined in Section 2.

3.1. SDSS stacks with auroral line detections

Auroral line measurements have been obtained across a wide range of stellar masses, SFRs, and excitation levels by stacking the spectra of $z \sim 0$ star-forming galaxies from SDSS. Creating composite spectra in bins of global galaxy properties allows for the detection of the weak auroral lines $[\text{O III}]\lambda 4363$ and $[\text{O II}]\lambda\lambda 7320, 7330$ by leveraging the statistical power of hundreds or thousands of

galaxies per bin to increase sensitivity. This method has progressed metallicity studies of local galaxies by reducing the reliance on strong-line indicators. AM13 utilized measurements of composite spectra binned in M_* alone, as well as M_* and SFR, to investigate the MZR and FMR using direct-method metallicities. B16 constructed composite spectra for SDSS galaxies in bins of M_* and position above or below the mean $z \sim 0$ relation between M_* and specific star-formation rate (SSFR; SFR/M_*), demonstrating a systematic dependence of strong-line indicators on position relative to the M_* -SSFR relation. C17 binned galaxies in O3 and O2, and utilized auroral line measurements from stacked spectra to provide fully empirical strong-line metallicity calibrations based on global galaxy spectra rather than H II regions for the first time. Strong and auroral line ratio measurements of the stacked spectra from these studies provide a comparison sample that both spans a wide range of metallicities and is representative of the $z \sim 0$ star-forming population.

Our goal is to quantify the mean bias in metallicity measurements inferred from global galaxy spectra relative to the characteristic metallicity of the H II regions within a galaxy as a function of global galaxy properties. Thus, it is imperative that the samples that are used to test the performance of the models are themselves representative of the normal star-forming population of galaxies. While the stacked spectra from AM13, B16, and C17 are constructed from samples that largely overlap (AM13 and B16 use identical sample selection, while the selection criteria of C17 only slightly differ), we simultaneously compare to stacks from all three works in order to average over differences in selection, binning, and stacking methods. Because of the binning methods of each work, some bins will contain galaxies that are wholly unrepresentative of the typical local population (e.g., M_* -SFR bins that fall far from the mean $z \sim 0$ M_* -SFR relation). We only compare to those stacks from each work that closely follow the mean galaxy property relations of the local population. We use the stacks binned in M_* only from AM13. From B16, we use those stacks that fall within ± 0.5 dex in SSFR of the mean $z \sim 0$ M_* -SSFR relation. We select the C17 stacks for which the central O3 and O2 of the bin fall within ± 0.1 dex of the median relation of the strong-line comparison sample of individual SDSS galaxies. As described below, we choose observationally-motivated values of the DIG fraction f_{DIG} , the number of H II regions per mock galaxy N_{HII} , and the T_3 distribution width σ_T appropriate for the sample of galaxies from which the stacked spectra were created.

We place constraints on f_{DIG} using the $\text{H}\alpha$ surface brightness, $\Sigma_{\text{H}\alpha}$, given by

$$\Sigma_{\text{H}\alpha} = \frac{L_{\text{H}\alpha}^{\text{tot}}}{2\pi R_{\text{half,H}\alpha}^2}, \quad (23)$$

where $L_{\text{H}\alpha}^{\text{tot}}$ is the total $\text{H}\alpha$ luminosity, and $R_{\text{half,H}\alpha}$ is the half-light radius of the galaxy $\text{H}\alpha$ emission. Oey et al. (2007) demonstrated that f_{DIG} decreases with increasing $\Sigma_{\text{H}\alpha}$. The authors argued that a scenario in which H II regions occupy a larger fraction of the ionized ISM volume as star formation becomes more concentrated predicts a dependence of $f_{\text{DIG}} \sim \Sigma_{\text{H}\alpha}^{1/3}$, which agreed well with the

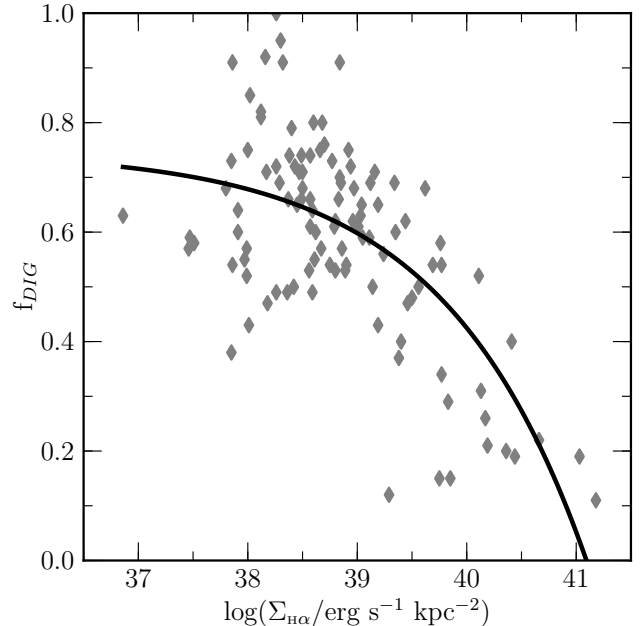


Figure 7. The fraction of Balmer emission originating from DIG, f_{DIG} , vs. $\Sigma_{\text{H}\alpha}$ for galaxies from the SINGG $\text{H}\alpha$ survey (Oey et al. 2007), displayed as gray diamonds. The best-fit function of the form $f_{\text{DIG}} \sim \Sigma_{\text{H}\alpha}^{1/3}$, as suggested by Oey et al. on theoretical grounds, is displayed as a black line and presented in equation 24.

data. Using the dataset from Oey et al. (2007), we fit f_{DIG} as a function of $\Sigma_{\text{H}\alpha}$ assuming this theoretically-predicted functional form, and obtain

$$f_{\text{DIG}} = -1.50 \times 10^{-14} \times \Sigma_{\text{H}\alpha}^{1/3} + 0.748, \quad (24)$$

where $\Sigma_{\text{H}\alpha}$ is given in units of $\text{erg s}^{-1} \text{kpc}^{-2}$. The data and best-fit function are shown in Figure 7.

We constrain f_{DIG} for the SDSS stack samples using $\Sigma_{\text{H}\alpha}$ of the individual SDSS galaxies in the strong-line comparison sample, which is nearly identical to the sample from which the AM13 and B16 stacks were constructed (see Section 2.4). We note that results do not change if the strong-line comparison sample is instead selected using the criteria of C17. To determine $\Sigma_{\text{H}\alpha}$ for the strong-line comparison sample, we first aperture-correct the intrinsic fiber $\text{H}\alpha$ luminosities. We obtain aperture corrections by dividing the total SFR by the fiber SFR, and apply these correction factors to the fiber $\text{H}\alpha$ luminosities to obtain total $\text{H}\alpha$ luminosities (Brinchmann et al. 2004). While measurements of the $\text{H}\alpha$ half-light radii are not available, we instead use the optical sizes. R-band sizes of local star-forming galaxies have been shown to be similar to $\text{H}\alpha$ sizes (James et al. 2009). We use the elliptical Petrosian R-band half-light radii from the NASA-Sloan Atlas v1.0.1⁵. Galaxy sizes are not available for all galaxies in the strong-line comparison sample. The NASA-Sloan Atlas contains size measurements for 79% of the full sample ($\sim 165,000$ galaxies) for which we compute the dust-corrected $\Sigma_{\text{H}\alpha}$ according to equation 23. The DIG fraction for each galaxy is then estimated using equation 24.

The distribution of f_{DIG} values and f_{DIG} vs. O3^{gal} for the strong-line comparison sample are shown in Figure 8.

⁵ <http://www.nsatlas.org>

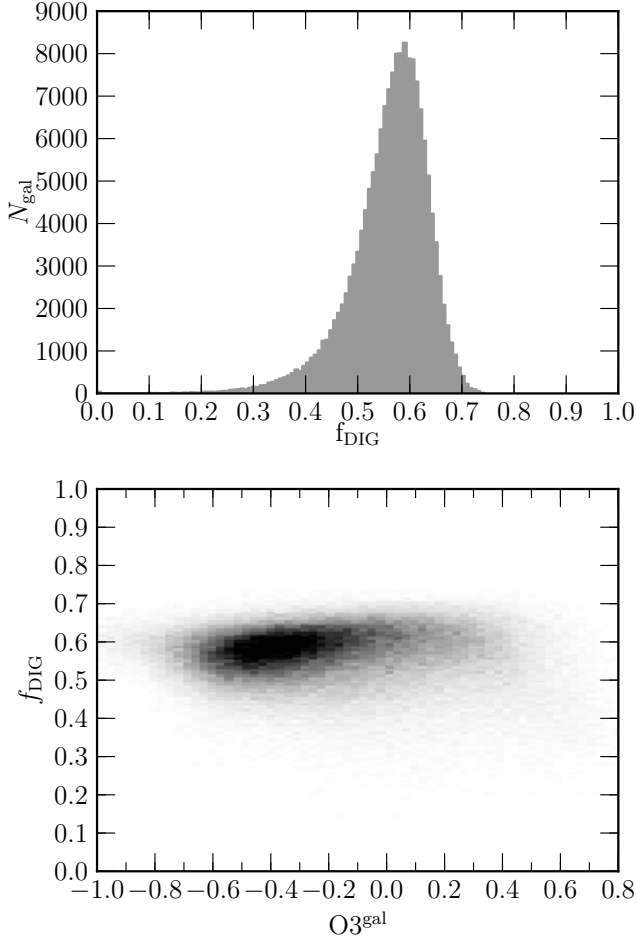


Figure 8. The distribution of f_{DIG} (top) and f_{DIG} as a function of $O3$ (bottom) for SDSS galaxies in the strong-line comparison sample. The f_{DIG} distribution has a median value of 0.55 and a standard deviation of 0.08, and is nearly Gaussian in shape. The DIG fraction f_{DIG} does not show a strong dependence on excitation, as encoded by $O3$.

The strong-line comparison sample has a median f_{DIG} of 0.55 with a standard deviation of 0.08. The distribution shape is nearly Gaussian, with a more significant tail towards low f_{DIG} . The DIG fraction shows no significant dependence on excitation across a wide dynamic range, with the median f_{DIG} changing by $< 5\%$ as a function of $O3^{\text{gal}}$. Additionally, the scatter in f_{DIG} also shows no strong dependence on $O3^{\text{gal}}$. We therefore assign f_{DIG} to each mock galaxy by randomly drawing values from a normal distribution with a mean value of 0.55 and a standard deviation of 0.08. It is important to note that f_{DIG} is not dependent on any line ratios, and is thus independent of all of the line-ratio diagrams that we use to test the models.

As noted above, the number of H II regions per galaxy, N_{HII} , does not affect any trends but instead corresponds to a source of uncorrelated scatter, which decreases as N_{HII} increases and the T_3 distribution is better sampled. The chosen value of N_{HII} has no systematic effects on our results. Nevertheless, we choose a value of N_{HII} that is appropriate for SDSS fiber observations of local star-forming galaxies. At $z_{\text{med}} = 0.08$, the median redshift of the strong-line comparison sample, the $3''$ diameter of an

SDSS fiber corresponds to a physical diameter of 4.5 kpc. Based on H II region identification in narrowband H α surveys (e.g., Zurita et al. 2000), a ~ 4.5 kpc diameter aperture will typically contain tens of H II regions, but may contain as few as a handful of H II regions depending on fiber placement, the ISM structure, and level of star-formation activity in the galaxy. We choose a value of $N_{\text{HII}} = 25$ to roughly match the number of H II regions expected to fall within an SDSS fiber aperture.

We set $\sigma_T = 0.07$ dex, a value that appears to be reasonable for $z \sim 0$ star-forming galaxies as described below. This value is within the range of observed σ_T for local spirals in the CHAOS galaxy survey (see Fig. 5, Berg et al. 2015; Croxall et al. 2015, 2016). We note that the T_3 distribution width, σ_T , encodes both stochastic variations in metallicity due to inhomogeneities in the ISM and systematic variations from radial metallicity gradients, if the observed aperture covers a large area of the disk compared to the steepness of the gradient. Radial oxygen abundance gradients of local star-forming galaxies tend to have slopes ranging from ~ -0.01 to ~ -0.1 dex kpc^{-1} for galaxies with $8.5 < \log(M_*/M_\odot) < 11.$, with less massive galaxies displaying steeper gradients on average (Sánchez et al. 2014; Ho et al. 2015). At the median redshift of the strong-line comparison sample, $z_{\text{med}} = 0.08$, $1''$ corresponds to a physical length of 1.5 kpc. With the assumption that the $3''$ SDSS fiber is placed on the center of each galaxy, the light falling in the fiber probes the inner ~ 2 kpc radially. Thus, the additional temperature variations due to metallicity gradients are likely only significant for the least-massive galaxies in SDSS. After measurement uncertainty is accounted for, the intrinsic scatter of H II regions about the metallicity gradients in local spirals is $\sim 0.05 - 0.1$ dex (Kennicutt et al. 2003; Rosolowsky & Simon 2008; Bresolin 2011; Berg et al. 2013; Croxall et al. 2015, 2016), corresponding to $\sim 0.02 - 0.07$ dex in T_3 indicative of the minimum σ_T in the absence of metallicity gradients for local star-forming galaxies. The shallow gradients of the CHAOS galaxies ($0.02-0.04$ dex kpc^{-1}) suggest that stochastic variations in metallicity account for the majority of the width of the electron temperature distributions in Figure 5.

In summary, the model matched to typical SDSS star-forming galaxies assumes a Gaussian f_{DIG} distribution characterized by a mean and standard deviation of 0.55 and 0.08, respectively, $N_{\text{HII}} = 25$, and $\sigma_T = 0.07$ dex. We create 2500 mock galaxy spectra following the method described in Section 2.5, where T_{cent} is drawn from a logarithmic uniform distribution from $\log(T_{\text{cent}}/\text{K}) = 3.7$ to 4.3 (5,000 to 20,000 K), the T_3 range of the reference H II region sample. We infer median line ratio and electron temperature relations from these 2500 mock galaxy spectra. We create an additional model for comparison with the same parameters except $f_{\text{DIG}} = 0$ such that the mock galaxies are constructed from H II regions only and include no DIG emission. We refer to this model with no DIG emission as the *hiionly* model.

We compare the model with $f_{\text{DIG}}=0.55$ matched to SDSS stacks to AM13, B16, and C17 stacks in Figures 9-11, and include the *hiionly* model for comparison. The $O3N2$, $O3S2$, and $O3O2$ strong-line ratio diagrams are shown in Figure 9. The $f_{\text{DIG}}=0.55$ model shows excellent agreement with excitation sequences followed by the

SDSS stacks. The *hiionly* model fails to reproduce the O3S2 and O3O2 sequences, displaying lower S2 and O2 at fixed O3 than the AM13, B16, and C17 stacks at nearly all values of O3. The largest disagreement occurs in the moderate metallicity regime where $O3 \sim 0.0$. This failure of the *hiionly* model confirms that combinations of H II regions alone cannot simultaneously reproduce line ratio sequences in all line-ratio spaces. DIG emission properties are distinct from those of H II regions in S2 and O2, which strongly affects global galaxy line ratios and must be taken into consideration. The close agreement of the $f_{\text{DIG}}=0.55$ model to the observations in the O3S2 and O3O2 diagrams suggests that both the DIG excitation sequences in Figure 4 and the f_{DIG} relation in equation 24 are reasonable.

The strong-line ratios $O3^{\text{gal}}$, $O2^{\text{gal}}$, $N2^{\text{gal}}$, and $S2^{\text{gal}}$ are shown as a function of T_3^{gal} and T_2^{gal} in Figure 10. T_3^{gal} measurements are only available for the SDSS stacks with $T_3^{\text{gal}} > 10^4$ K. The reason for this limited range is twofold. First, the strong-to-auroral line ratio $[O \text{ III}]\lambda\lambda 5007, 4959/\lambda 4363$ becomes exponentially weaker at lower T_3 while O3 also drops off significantly due to a smaller fraction of oxygen in the O^{++} state, leading to an extremely weak $[O \text{ III}]\lambda 4363$ at low T_3^{gal} that may not even be detected in stacks. Second, $[O \text{ III}]\lambda 4363$ is blended with $[\text{Fe II}]\lambda 4360$, which significantly contaminates $[O \text{ III}]\lambda 4363$ measurements for high-metallicity, low- T_3^{gal} galaxies in which $[\text{Fe II}]\lambda 4360$ is stronger (Andrews & Martini 2013; Curti et al. 2017). T_3^{gal} measurements are not shown for AM13, B16, and C17 stacks with $[\text{Fe II}]\lambda 4360/[O \text{ III}]\lambda 4363 > 0.5$ for which $[O \text{ III}]\lambda 4363$ measurements were deemed unreliable. Due to the combined effect of these two limitations, T_3^{gal} measurements are only shown for stacks of galaxies with $\log(M_*/M_\odot) \lesssim 9.4$. The $f_{\text{DIG}}=0.55$ model matches the observed SDSS stacks well in the T_3^{gal} diagrams within the amount of scatter displayed by the SDSS stacks. The *hiionly* model fails to produce high enough $O2^{\text{gal}}$ and $S2^{\text{gal}}$ values at moderate T_3^{gal} to match the observations. Due to the limited dynamic range of the T_3^{gal} measurements for the SDSS stacks, the turnover points of the models ($\log(T_3^{\text{gal}}) \approx 3.95$ for $O2^{\text{gal}}$ and $S2^{\text{gal}}$) that would provide an excellent test for agreement are not sampled by the SDSS stacks.

In the right column of Figure 10, we again compare the predicted model line ratios with those observed in the SDSS composites, this time as a function of T_2^{gal} . The auroral line $[O \text{ II}]\lambda\lambda 7320, 7330$ does not suffer from contamination or severe dropoff in brightness at high metallicities, and is thus robustly measured across a much wider range of temperatures than $[O \text{ III}]\lambda 4363$. The *hiionly* model shows large discrepancies in $O2^{\text{gal}}$ and $S2^{\text{gal}}$ again demonstrating the importance of accounting for DIG emission in global galaxy spectra. The shapes of the $f_{\text{DIG}}=0.55$ model sequences match those of the observed sequences well, but with a systematic offset towards higher T_2^{gal} at fixed line ratio that is seen in all four strong-line ratios.

Since strong-line ratios of H II regions as a function of T_3 and T_2 are directly constrained by observations,

this offset in T_2^{gal} must either originate from incorrect assumptions about DIG region line ratios or electron temperatures, or from a systematic effect in the binning and stacking process that is not captured in our models that only produce individual galaxy spectra. It is improbable that incorrect strong-line DIG excitation sequences (see Figure 4) are the cause of this offset, because shifting the strong-line ratios of DIG regions alone would lead to a mismatch in the strong-line vs. strong-line sequences shown in Figure 9, which agree well under the current set of assumptions. Additionally, no systematic offset is observed the strong-line vs. T_3^{gal} plots in Figure 10, and changing the DIG strong-line excitation sequences would introduce a disagreement in these diagrams as well. The T_2^{gal} offset also cannot be resolved by decreasing f_{DIG} as T_2^{gal} increases. This adjustment would introduce disagreement in Figure 9 and the left column of Figure 10 while still failing to match the high- T_2^{gal} tail of the observations where even the *hiionly* model overestimates $O2^{\text{gal}}$, $N2^{\text{gal}}$, and $S2^{\text{gal}}$ and underestimates $O3^{\text{gal}}$ at fixed T_2^{gal} .

The T_2 - T_3 diagram is shown in Figure 11. In this diagram, the SDSS stacks display lower T_2^{gal} at fixed T_3^{gal} than the H II region relation of Campbell et al. (1986) (equation 12). Both the *hiionly* and $f_{\text{DIG}}=0.55$ models fall below the H II region T_2 - T_3 relation, but neither show as large of an offset as the SDSS stacks. The small difference between the *hiionly* ($f_{\text{DIG}}=0.0$) and $f_{\text{DIG}}=0.55$ models is predominantly due to the different relation between O2 and T_2 for DIG regions compared to that of H II regions, which changes the relative weight of regions of different T_2 to the T_2^{gal} estimate from the global galaxy spectrum. In order to match the observations, the $f_{\text{DIG}}=0.55$ model must have higher T_3^{gal} at fixed T_2^{gal} or lower T_2^{gal} at fixed T_3^{gal} . No systematic offset in T_3^{gal} is observed in Figure 10, suggesting that the mismatch between model and observations in the T_2 - T_3 diagram is caused by a mismatch in T_2^{gal} alone. The T_2^{gal} offsets in Figure 10 appear to be roughly equivalent for each strong-line ratio, with the model being ~ 0.05 dex higher in T_2^{gal} at fixed line ratio than the observations, corresponding to an offset of $\sim 1,000 - 1,500$ K at $T_2 = 8,000 - 12,000$ K that closely matches the T_2^{gal} discrepancy between the $f_{\text{DIG}}=0.55$ model and observations at fixed T_3^{gal} . We conclude that the discrepancy between the $f_{\text{DIG}}=0.55$ model and SDSS composites originates from T_2^{gal} alone.

The T_2^{gal} discrepancy between model and observations could arise from either an incorrect assumption about DIG electron temperatures in the models or some aspect of the stacking process that is not captured by our individual galaxy models, since we are comparing to data from stacked spectra. We do not have a way of testing the latter hypothesis without matching the scatter in SDSS excitation sequences in detail and obtaining actual line profiles from the models in addition to line fluxes, which our models do not do since they are only designed to investigate mean properties of the local galaxy population. However, both AM13 and C17 performed their stacking procedures on individual SDSS galaxies with auroral-line

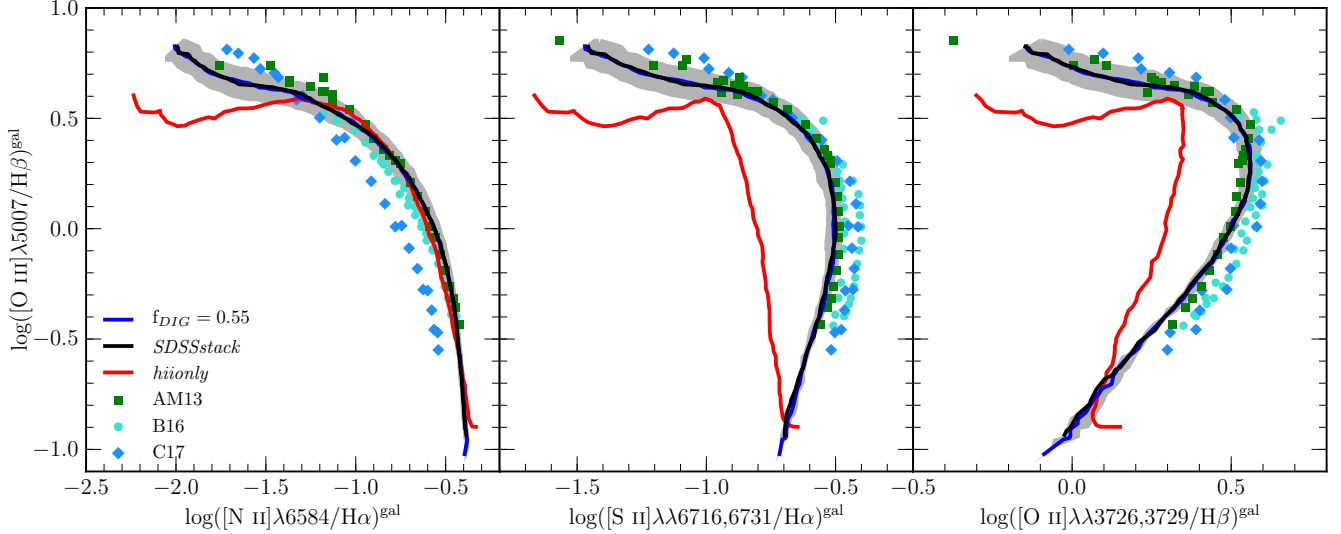


Figure 9. The O3N2 (left), O3S2 (middle), and O3O2 (right) strong-line ratio diagrams for stacks of SDSS galaxies and models under different sets of assumptions and input parameters. The stacks of $z \sim 0$ SDSS star-forming galaxies from AM13, B16, and C17 are shown as green squares, light blue circles, and dark blue diamonds, respectively. The blue line shows the running median of mock galaxies in bins of O3N2^{gal} for the model with $f_{\text{DIG}}=0.55$ and equal H II and DIG T_2 at fixed metallicity. The shaded gray region represents the 68th-percentile width of the distribution of mock galaxies around this running median. The black line displays the running median for the *SDSSstack* model with $f_{\text{DIG}}=0.55$ under the assumption that DIG T_2 is 15% lower than H II region T_2 at fixed metallicity, and is identical to the blue line in these strong-line ratio diagrams. The red line shows the *hionly* model that does not include DIG emission ($f_{\text{DIG}}=0.0$).

detections and found that the inferred electron temperatures and metallicities of the stacks were not systematically offset from the mean values of the individual galaxies. These tests suggest that the offset in T_2^{gal} does not originate from a systematic effect of the binning and stacking procedures.

The T_2^{gal} discrepancy then most likely arises from an incorrect assumption about T_2 of DIG regions. Up to this point, we have assumed that T_2 and T_3 of a DIG region are the same as those of the associated H II region. The observed T_2^{gal} offset instead suggests that the DIG T_2 is lower than that of H II regions at fixed metallicity, while T_3 remains roughly equivalent. We find that the model can be brought into excellent agreement with the SDSS composites if the T_2 of each DIG region is assumed to be 15% (0.06 dex) lower than that of the associated H II region. Models incorporating the revised DIG T_2 assumption are shown in Figures 9-11 as black lines, and we refer to this model as the *SDSSstack* model. Results are unchanged for diagrams that do not involve T_2^{gal} , while the shift towards lower T_2^{gal} brings the adjusted model into excellent agreement with the SDSS stacks in Figures 10 and 11. We adopt the *SDSSstack* model as the fiducial description for typical $z \sim 0$ star-forming galaxies for the remainder of this work.

Our assumption that DIG T_2 is lower than T_2 of H II regions on average is in conflict with past studies of Milky Way and extragalactic DIG, which suggest that DIG electron temperature is higher on average than that of H II regions. Studies of DIG strong-line ratios in the Milky Way (Haffner et al. 1999) and other galaxies (Otte et al. 2001, 2002; Hoopes & Waltherbos 2003) have suggested that DIG is hotter than H II regions on average based on the larger N2, S2, and O2 ratios observed for DIG. Additionally, Reynolds et al. (2001) detected the auroral line [N II]λ5755 for DIG along one line-of-sight in the Milky Way, and found that DIG along this line-of-sight has a

higher temperature than bright Galactic H II regions. However, the Milky Way results only probe a number of distinct sight lines and most extragalactic studies of DIG line-ratios observe extra-planar DIG in edge-on galaxies. It is not clear how representative such observations are of the DIG regions observed in face-on disk galaxies in the MaNGA DIG galaxy sample, and if past comparisons between DIG and H II region temperature have been made at fixed nebular abundance. Additional observations of temperature-sensitive auroral lines for DIG regions are required to unequivocally settle the question of DIG electron temperature. Even if DIG T_2 is not lower than that of H II regions in reality, adopting this assumption in our model framework captures an important systematic effect that is present in global galaxy spectra and will contribute to the bias in direct-method metallicity.

One concern is whether the disagreement in the T_2 - T_3 diagram and strong-line ratio vs. T_2 diagrams can be resolved by adjusting other model parameters instead of making an assumption that DIG T_2 is 15% lower than H II region T_2 at fixed metallicity. In particular, the width of the T_3 distribution, σ_T , can change the magnitude of the offset in the T_3 - T_2 diagram. This effect has been previously shown by Pilyugin et al. (2012b), who demonstrated that the T_2 - T_3 offset increases as the range of metallicities of combined H II regions increases (equivalent to increasing σ_T in our framework). We have set $\sigma_T = 0.07$ dex based on empirical observations of H II regions in individual galaxies (Berg et al. 2015; Croxall et al. 2015, 2016), but it is worthwhile to investigate whether different values of σ_T may resolve the T_2 discrepancies. Such an investigation is presented in Appendix B. To briefly summarize, while increasing σ_T can reproduce the SDSS stack T_2 - T_3 offset without any different assumptions regarding DIG T_2 , the required values of σ_T lead to significant changes in the predicted global galaxy strong-line ratios that do not match the observations. Adjusting σ_T is thus not a viable option for resolving the

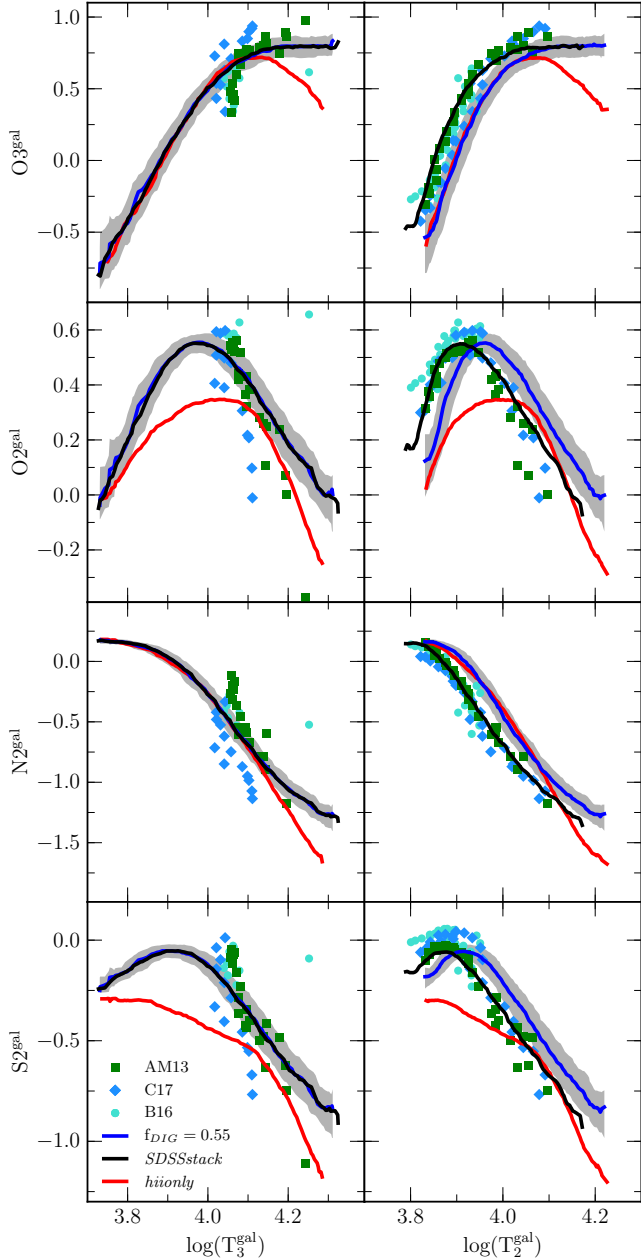


Figure 10. Global galaxy strong-line ratios $O3^{\text{gal}}$, $O2^{\text{gal}}$, $N2^{\text{gal}}$, and $S2^{\text{gal}}$ as a function of T_3^{gal} (left column) and T_2^{gal} (right column). Lines and points are the same as in Figure 9. The $f_{\text{DIG}}=0.55$ model is systematically offset towards higher T_2 at fixed line ratio compared to the SDSS stacks. This offset is not present in the *SDSSstack* model, in which we assume that DIG T_2 is lower than H II region T_2 by 15% at fixed metallicity.

T_2 discrepancies, and we continue under the assumption that DIG T_2 is 15% lower than H II region T_2 at fixed metallicity.

3.2. The SDSS auroral-line comparison sample

We also test our model framework against observations of individual SDSS galaxies with electron temperature measurements. We use the sample of 181 SDSS galaxies from Pilyugin et al. (2010) for which both $[\text{O III}]\lambda 4363$ and $[\text{O II}]\lambda\lambda 7320, 7330$ have been detected. We ex-

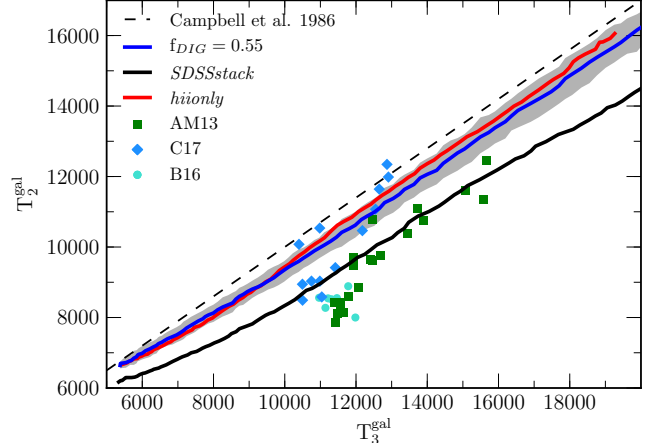


Figure 11. The global galaxy ionic temperature diagram of T_2^{gal} vs. T_3^{gal} . The dashed black line shows the H II region T_2 - T_3 relation of Campbell et al. (1986) given in equation 12. All other lines and points are the same as in Figure 9.

pand this sample by adding 271 galaxies from Izotov et al. (2006). Izotov et al. identified 309 SDSS galaxies for which $[\text{O III}]\lambda 4363$ was measured, and we add those galaxies that were not already included as part of the Pilyugin et al. (2010) sample. We note that while all of these additional galaxies have measurements of $[\text{O III}]\lambda 4363$ and $[\text{O II}]\lambda\lambda 7320, 7330$, only 86 have measurements of $[\text{O II}]\lambda\lambda 3726, 3729$ due to their redshifts, and thus not all of them have estimates of T_2^{gal} . Those objects lacking $[\text{O II}]\lambda\lambda 3726, 3729$ observations are not plotted in diagrams involving $O2^{\text{gal}}$ or T_2^{gal} . We refer to this combined sample as the “auroral-line comparison sample.”

We determine the DIG fraction for the auroral-line comparison sample following the same method used for the larger SDSS sample. We apply aperture correction factors to the reddening-corrected $H\alpha$ luminosities, and determine $\Sigma_{H\alpha}$ using the R-band half-light radius for each galaxy in the auroral-line comparison sample. The DIG fractions are found using equation 24. The auroral-line comparison sample has an f_{DIG} distribution that is nearly Gaussian, with a mean and standard deviation of 0.4 and 0.13, respectively, and no strong dependence on the level of excitation in the global galaxy spectrum. The lower average f_{DIG} for this sample compared to that of the full SDSS sample reflects the extreme star-forming nature of galaxies in the auroral-line comparison sample. Model f_{DIG} values are drawn randomly from this normal distribution. We adopt the same value as in the *SDSSstack* model for the number of H II regions per fiber, $N_{\text{HII}} = 25$, but find that a smaller width of the T_3 distribution better fits the auroral-line sample, instead using $\sigma_T = 0.02$ dex. A smaller value of σ_T is likely more appropriate for the low-mass, high-sSFR galaxies in the auroral-line comparison sample. Metals can be distributed more homogeneously throughout the ISM in such galaxies than in massive or low-sSFR galaxies because of an increase in feedback efficiency, as suggested by flatter metallicity gradients with decreasing M_* and increasing sSFR (Ho et al. 2015; Ma et al. 2017). We continue to assume that DIG T_2 is 15% lower than H II region T_2 at fixed metallicity, as described in Sec-

tion 3.1. Despite the comparatively narrow T_3^{gal} range of the auroral-line comparison sample, we again randomly draw 2500 samples of T_{cent} from a logarithmic uniform distribution over $\log(T_{\text{cent}}/\text{K}) = 3.7$ to 4.3, and create mock galaxy spectra following the method described in Section 2.5. We refer to this model as the *auroral* model.

We compare the *auroral* model to individual galaxies in the auroral-line comparison sample in Figures 12-14. We find that the strong-line ratio diagrams (Fig. 12), line ratios as a function of T_2^{gal} (Fig. 13, right column), and the T_2 - T_3 diagram (Fig. 14) show excellent agreement between the *auroral* model and observations. However, as a function of T_3^{gal} (Fig. 13, left column) the model overestimates $N2^{\text{gal}}$, $S2^{\text{gal}}$, and $O2^{\text{gal}}$ at fixed T_3^{gal} in the high-temperature regime ($\log(T_3^{\text{gal}}) > 4.1$). The discrepancies are largest in the high-temperature, low-metallicity regime for which we had to extrapolate the DIG excitation sequences, and thus may suggest that the DIG excitation sequence extrapolations are not completely accurate in this regime, especially for $O2^{\text{gal}}$. We caution that results for metal-poor galaxies with observed $O3N2^{\text{gal}} \gtrsim 2.0$ and $\log(T_3) \gtrsim 4.15$ rely heavily on the extrapolation of the DIG sequences and should therefore be treated with caution. It is also possible that the extreme star-forming and metal-poor nature of some of the galaxies in the auroral-line comparison sample require some physics that is not captured in the framework of our simple models. However, the model framework appears to perform well overall even for a sample of extreme star-forming galaxies that are unrepresentative of the local star-forming galaxy population. It is also of note that the assumption that DIG T_2 is lower than H II region T_2 at fixed metallicity is required to match observations of *individual* galaxies with auroral-line measurements in addition to stacks of SDSS galaxies, suggesting that the T_2 offset is not a result of some systematic effect introduced by the stacking process.

4. RESULTS

Using these models, we characterize the biases in strong-line ratios, electron temperatures, and direct-method metallicity measurements from global galaxy spectra. These biases arise as a consequence of DIG contamination of emission lines and flux-weighting effects when combining emission from multiple H II regions with a range of excitation levels. The bias of a particular property is quantified by taking the difference between the value measured from a mock global galaxy spectrum and the median value of the same property for the individual H II regions in that mock galaxy. We represent the bias in property X with the symbol ΔX . For each property, the superscript “gal” (X^{gal}) indicates that the property is derived from the observed global galaxy spectrum, while the superscript “HII” (X^{HII}) is used to indicate the median value of the property for the distribution of H II regions within each galaxy. Obtaining measurements that are representative of the H II region distribution in a galaxy is desirable because both strong-line and direct-method metallicity estimates are based on H II regions (real or simulated) rather than ensembles of H II regions surrounded by DIG. Furthermore, the H II regions trace only the most recent generation of star formation. Therefore, they provide a metallicity that

is ideal for comparing to cosmological hydrodynamical simulations, which trace the metallicity of star-forming particles.

The bias determinations presented below can be used to correct properties measured from global galaxy spectra in order to obtain values representative of the median H II region distributions. The *SDSSstack* model is designed to reproduce the mean properties and trends of $z \sim 0$ star-forming galaxies, but does not accurately represent deviations of individual galaxies from mean relations.

4.1. Biases in the strong-line ratios

We quantify the typical global galaxy bias in the strong-line ratios O3, O2, N2, and S2 for $z \sim 0$ star-forming galaxies from SDSS. These strong-line ratios can be combined to construct strong-line metallicity indicators used in calibrations that are widely applied to estimate galaxy metallicities. Additionally, the strong-line ratios O3 and O2 are used in the calculation of direct-method metallicity (equations 13 and 14). It is thus of great importance to eliminate biases in galaxy strong-line ratios before using either the direct method or strong-line calibrations to determine galaxy metallicities.

In Figure 15, we present the global galaxy biases in O3, O2, N2, and S2 as a function of $O3N2^{\text{gal}}$, the O3N2 ratio as observed in global galaxy spectra. To determine the typical biases, we take the running median of individual mock galaxy spectra from each model in bins of $O3N2^{\text{gal}}$. The biases are quantified as a function of $O3N2^{\text{gal}}$ instead of each individual line ratio (i.e., we show $\Delta O3$ vs. $O3N2^{\text{gal}}$ as opposed to $\Delta O3$ vs. $O3^{\text{gal}}$) because O3N2 increases monotonically with metallicity and T_3 , and does not saturate over the range of metallicities of interest here. O3 and O2 are double-valued such that it would be necessary to determine on which branch a galaxy lies in order to correct the line ratio, and S2 and N2 saturate at high metallicities, limiting the utility of bias estimates as a function of these line ratios. Parameterizing by O3N2 instead should not severely limit the number of galaxies to which these corrections may be applied since O3N2 only involves strong lines that are easily detected in low-redshift star-forming galaxies down to low metallicities and stellar masses. We include the *hiionly* model for comparison in order to understand how much of the bias arises from DIG contamination. Biases in the *hiionly* model arise purely from flux-weighting effects due to combining light on a line-by-line basis from multiple H II regions with different metallicities. Any additional bias in models including DIG is driven by the inclusion of DIG emission in the global spectrum.

The top panel of Figure 15 shows the bias in O3. $O3^{\text{gal}}$ can be biased high by as much as +0.3 dex in typical local star-forming galaxies, with the maximum bias occurring at $O3N2^{\text{gal}} \gtrsim 2.0$. The *SDSSstack* and *hiionly* models display a similar level of $O3^{\text{gal}}$ bias at $O3N2^{\text{gal}} < 1.5$. In this regime, DIG emission has little effect on the global O3 bias because DIG and H II regions are matched in O3N2, and SDSS galaxies, DIG, and H II regions follow similar excitation sequences in the O3N2 diagram. The positive bias at $O3N2^{\text{gal}} < 1.5$, reaching +0.2 dex at $O3N2^{\text{gal}} \sim -0.5$, is predominantly driven by flux-weighting effects when combining light from H II regions

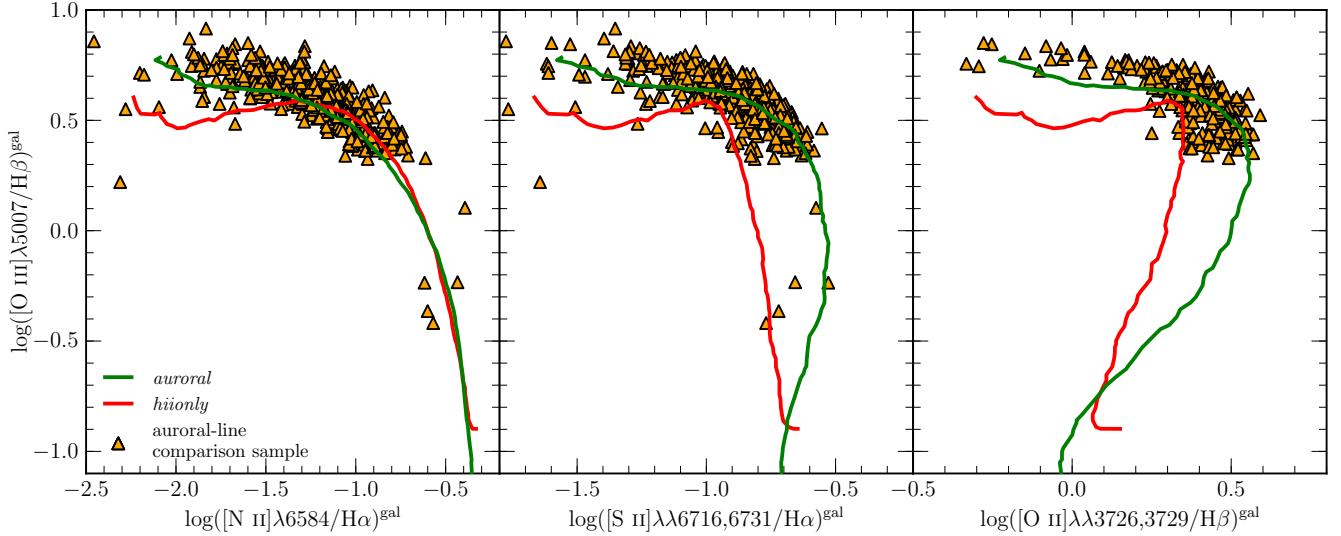


Figure 12. The O3N2 (left), O3S2 (middle), and O3O2 (right) strong-line ratio diagrams for individual SDSS galaxies with auroral line detections and models under different sets of assumptions and input parameters. Orange triangles show SDSS galaxies in the auroral-line comparison sample from Pilyugin et al. (2010) and Izotov et al. (2006). The green line displays the running median of mock galaxies in bins of $O3N2^{\text{gal}}$ for the *auroral* model with $f_{\text{DIG}}=0.40$ and $\sigma_T = 0.02$ dex, under the assumption that DIG T_2 is 15% lower than H II region T_2 at fixed metallicity. The red line shows the *hiionly* model that includes no DIG emission ($f_{\text{DIG}}=0.0$) and follows the same DIG T_2 assumption as the *auroral* model.

with a range of metallicities due to the shape of the O3 vs. T_3 relation of H II regions (Figure 2). Since $H\beta$ luminosity does not correlate with electron temperature for H II regions within a single galaxy (Berg et al. 2015; Croxall et al. 2015, 2016), when the slope of the O3 vs. T_3 relation is steep the global $[O III]\lambda 4959,5007$ flux is dominated by high-O3 H II regions while H II regions of all metallicities contribute equally to the global $H\beta$ flux on average. Thus, a steep slope in the O3 vs. T_3 relation leads to an $O3^{\text{gal}}$ value that is higher than $O3^{\text{HII}}$, the median of the individual H II regions. The positive bias is largest where the slope is steepest. In contrast, when the O3 vs. T_3 relation is flat near the turnover point ($O3N2^{\text{HII}} \sim 1.9$, $\log(T_3) \sim 4.1$) the bias from flux-weighting effects becomes small, as seen in the *hiionly* model at high $O3N2^{\text{gal}}$. At $O3N2^{\text{gal}} > 1.5$, the *SDSSstack* model diverges from the *hiionly* model, displaying a significant positive $\Delta O3$. In this low-metallicity regime, the DIG and H II region sequences diverge in the O3N2 diagram such that DIG regions have higher O3 and N2 than H II regions at fixed O3N2. This divergence leads to a positive $O3^{\text{gal}}$ bias that increases with increasing $O3N2^{\text{gal}}$. We note that mock galaxy spectra with $O3N2^{\text{gal}} \gtrsim 2.0$ rely almost entirely on the linear extrapolation of the DIG excitation sequence, and predictions in this regime should therefore be used with caution.

A similar relative behavior between the *SDSSstack* and *hiionly* models is observed in the $N2^{\text{gal}}$ bias, shown in the second panel from the bottom in Figure 15. At $O3N2^{\text{gal}} < 1.5$, the two models closely follow one another, while they diverge at $O3N2^{\text{gal}} > 1.5$ where DIG emission plays a role in the *SDSSstack* model. The explanation is the same as for the $O3^{\text{gal}}$ bias, except that in this case the $N2$ vs. T_3 relation is flat at low T_3 (low $O3N2$) and becomes steeper with increasing T_3 . Flux-weighting effects therefore lead to no bias at low $O3N2^{\text{gal}}$ and a slight increase in the bias at higher $O3N2^{\text{gal}}$ reaching +0.1 dex due to H II regions alone. The additional bias in the *SDSSstack* model at

$O3N2^{\text{gal}} > 1.5$ is again due to the divergence of DIG and H II regions in the O3N2 diagram, such that DIG regions have higher N2 than H II regions at fixed O3N2.

DIG emission plays a much more important role in the $O2^{\text{gal}}$ bias, displayed in the second panel from the top in Figure 15. The *hiionly* model shows a negligible $O2^{\text{gal}}$ bias of < 0.1 dex at all $O3N2^{\text{gal}}$ values. The lack of a significant bias in the *hiionly* model results from the shape of the O2 vs. T_3 relation, which peaks at $\log(T_3^{\text{HII}}) \sim 4.0$ ($O3N2^{\text{HII}} \sim 1.4$) and does not have a severely steep slope in either extreme. The *SDSSstack* model displays a larger $\Delta O2$ of > 0.1 dex over most of the $O3N2^{\text{gal}}$ range, peaking at +0.25 dex, and is primarily caused by DIG contamination in global galaxy spectra. DIG displays higher O2 at fixed O3N2 than H II regions, as can be seen in the O3N2 and O3O2 diagrams (Figure 3), leading to an overestimate of O2 relative to the median O2 of the the H II region distribution. The behavior of the *SDSSstack* $O2^{\text{gal}}$ bias can be understood through the divergence of the DIG excitation sequence from that of H II regions in the O3O2 diagram at both low metallicities ($O3N2^{\text{gal}} \gtrsim 1.75$) and moderate metallicities ($O3N2^{\text{gal}} \sim 0.5$).

The $S2^{\text{gal}}$ bias, shown in the bottom panel of Figure 15, behaves similarly to that of $O2^{\text{gal}}$. A flux-weighted combination of H II regions alone only leads to a small positive $\Delta S2$ at $O3N2^{\text{gal}} \gtrsim 1.75$. Elevated S2 in DIG regions leads to a bias in $S2^{\text{gal}}$ values as high as +0.35 dex at $O3N2^{\text{gal}} \sim 0.5$. $S2^{\text{gal}}$ displays a larger bias than $O2^{\text{gal}}$ because the DIG and H II region excitation sequences have a larger separation in the O3S2 diagram than in the O3O2 diagram (Figure 3).

In order to correct for these strong-line ratio biases in observed galaxy samples, we fit each bias as a function of observed $O3N2^{\text{gal}}$ with a fourth-order polynomial of the form

$$\Delta R = c_0 + c_1 x + c_2 x^2 + c_3 x^3 + c_4 x^4, \quad (25)$$

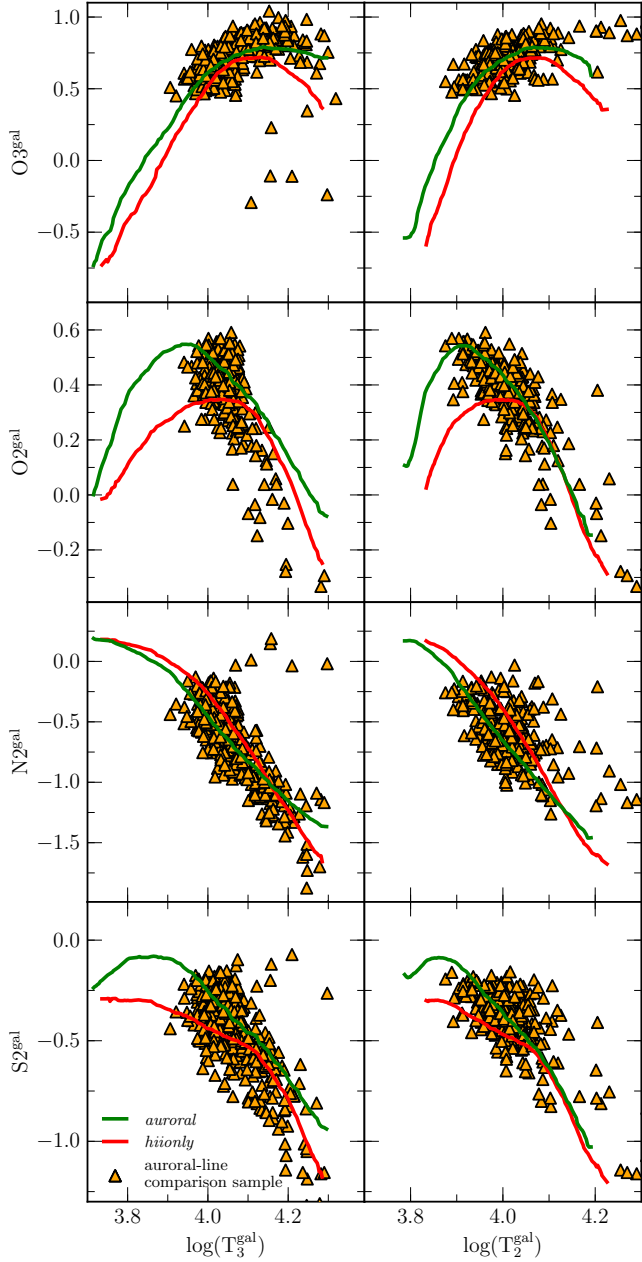


Figure 13. Global galaxy strong-line ratios $O3^{\text{gal}}$, $O2^{\text{gal}}$, $N2^{\text{gal}}$, and $S2^{\text{gal}}$ as a function of T_3^{gal} (left column) and T_2^{gal} (right column). Lines and points are the same as in Figure 12.

where $x = O3N2^{\text{gal}}$ and R is the strong-line ratio $O3$, $O2$, $N2$ or $S2$. The best-fit polynomials are shown in Figure 15 and the coefficients are given in Table 1. These bias functions may be subtracted from observed galaxy strong-line ratios to obtain the median strong-line ratios of the H II region distributions, correcting for DIG contribution and flux-weighting effects. We note that the corrections presented above are only appropriate for a sample of galaxies representative of typical $z \sim 0$ star-forming galaxies with $f_{\text{DIG}}=0.55$, and should not be applied to unrepresentative samples of galaxies. See Appendix A for bias characterizations over a range of f_{DIG} .

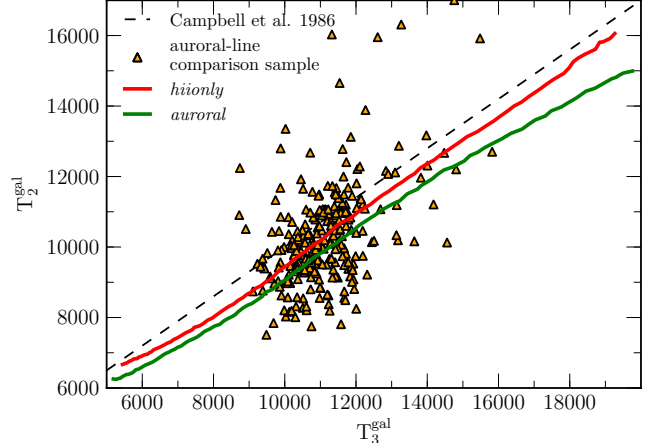


Figure 14. The global galaxy ionic temperature diagram of T_2^{gal} vs. T_3^{gal} . The dashed black line shows the H II region T_2 - T_3 relation of Campbell et al. (1986) given in equation 12. All other lines and points are the same as in Figure 12.

Table 1
Global galaxy bias coefficients

Strong-line ratios ^a					
ΔR	c_0	c_1	c_2	c_3	c_4
O3	0.138	-0.168	-0.0749	0.140	-0.0262
O2	0.208	0.118	-0.173	-0.00540	0.0260
N2	0.0312	-0.0111	-0.0277	0.0640	-0.0103
S2	0.296	0.188	-0.214	-0.0463	0.0457
Electron temperatures ^b					
ΔT_e	c_0	c_1	c_2	c_3	c_4
T_3	-2,171	6,813	-2,537,	-2,278	1,109
T_2	18,280	-75,610	114,500	-78,200	19,690
Direct-method oxygen abundances ^c					
$\Delta \log(O/H)$	c_0	c_1	c_2	c_3	c_4
T_3 and T_2^{d}	0.121	-0.337	0.629	-0.267	0.0333
T_3 only ^e	-0.0266	-0.591	0.530	0.311	-0.362
T_2 only ^f	0.340	-0.459	0.420	-0.0143	-0.00841

^aCoefficients for equation 25.

^bCoefficients for equation 26.

^cCoefficients for equation 27.

^dThe direct-method $12+\log(O/H)$ case where both T_3 and T_2 are directly determined from the galaxy spectrum.

^eThe case where only T_3 is estimated directly, while T_2 is inferred using equation 12.

^fThe case where only T_2 is estimated directly, while T_3 is inferred using equation 12.

4.2. Biases in the electron temperatures

Electron temperatures as inferred from global galaxy spectra also display biases with respect to the median electron temperature of the H II regions. We quantify the bias in T_3^{gal} (T_2^{gal}) by taking the running median of ΔT_3 (ΔT_2) of the individual mock galaxy spectra in bins of T_3^{gal} (T_2^{gal}). The typical biases in T_3 and T_2 , as inferred from global galaxy spectra, are shown in Figure 16.

In the *hiionly* model, T_3^{gal} is biased by as much as $\pm 1,000$ K with respect to T_3^{HII} , the median value of the H II region distribution. Below $T_3^{\text{gal}} = 14,000$ K, the *hiionly* T_3^{gal} is biased high, while ΔT_3 is negative at $T_3^{\text{gal}} = 14,000 - 19,000$ K. Since the *hiionly* model does not include any DIG emission, these biases are

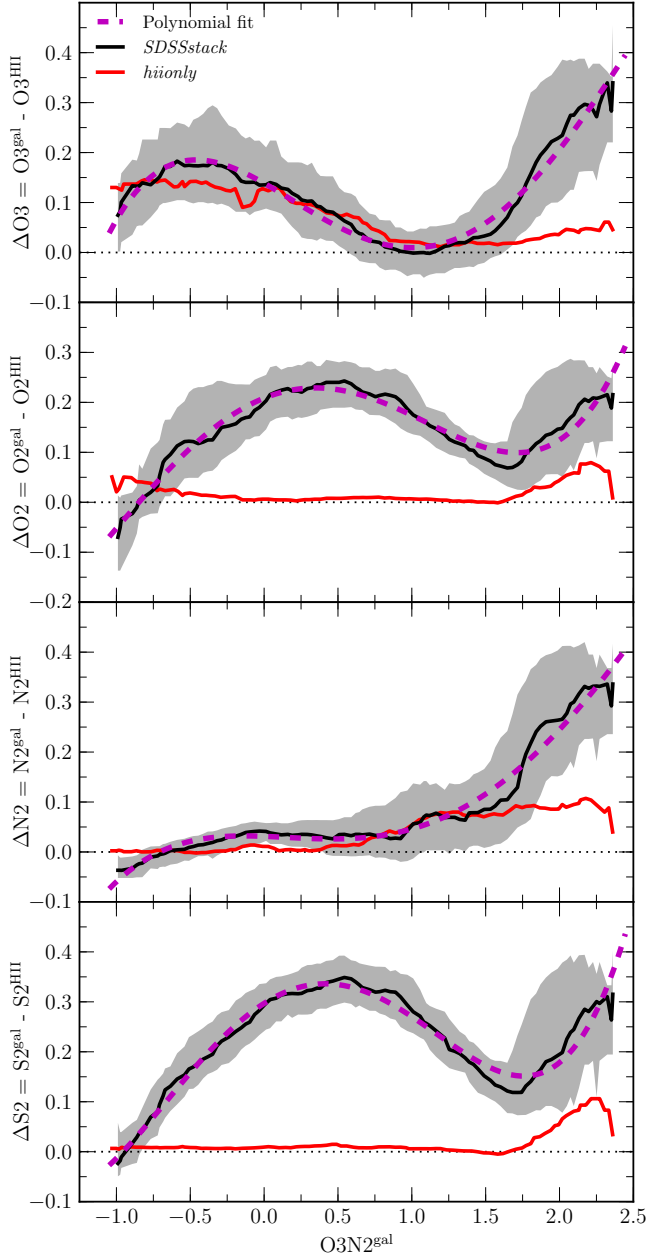


Figure 15. The difference between the global galaxy line ratio and median line ratio of the H II region distribution, ΔX , as a function of $O3N2^{\text{gal}}$ for the strong-line ratios $X=O3, O2, N2$, and $S2$. The red line shows the running median of the 2500 mock galaxy realizations in bins of $O3N2^{\text{gal}}$ for the *hiionly* model with $f_{\text{DIG}}=0.0$. The running median of the *SDSSstack* model with $f_{\text{DIG}}=0.55$ is displayed as a black line, where the gray shaded region corresponds to the 68th-percentile width of the distribution of mock galaxies around the running median. In each panel, the dashed magenta line shows the best-fit fourth-order polynomial to the bias in the global galaxy line ratio, ΔX , for the *SDSSstack* model. The best-fit coefficients are presented in Table 1.

a result of flux-weighting effects when combining light from multiple H II regions of different electron temperatures. T_3 sets the strong-to-auroral line ratio $Q3 = [\text{O III}]\lambda\lambda 4959, 5007 / \lambda 4363$. As T_3 increases, $Q3$ decreases exponentially (equation 9) such that hotter H II regions contribute more strongly to the global strong-to-auroral line ratio. In isolation, this trend would lead to ΔT_3

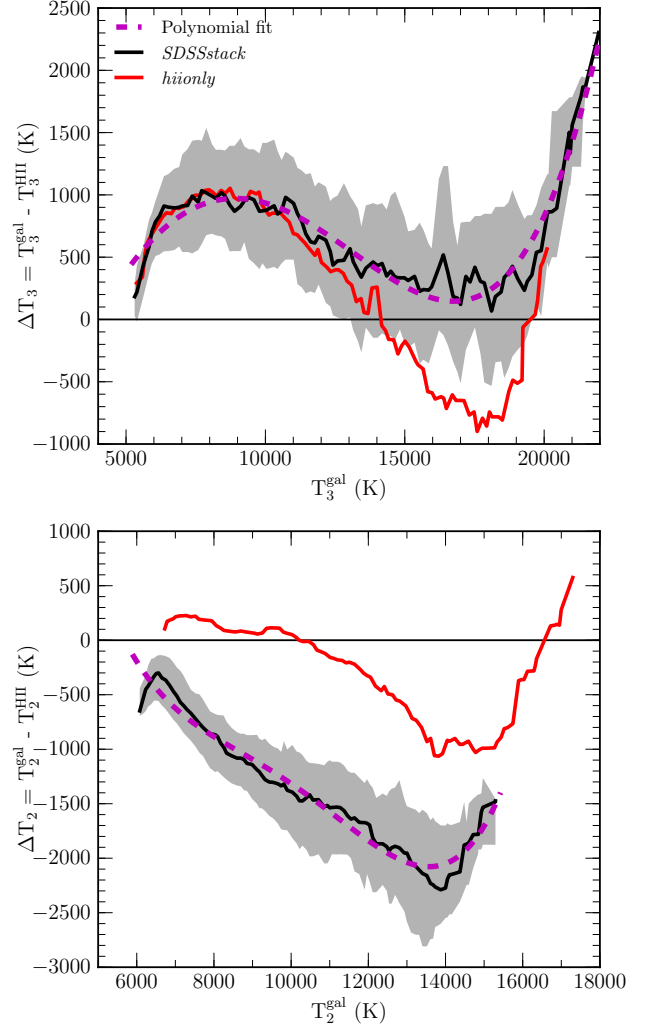


Figure 16. The difference between the global galaxy electron temperature, inferred from the observed galaxy spectrum, and the median electron temperature of the H II region distribution as a function of electron temperature. Results for T_3 are shown in the top panel, while the bias in T_2 is presented in the bottom panel. Lines and shading are the same as in Figure 15. The best-fit coefficients are given in Table 1.

that is always positive and increases significantly at high T_3^{gal} . However, since $H\beta$ luminosity does not correlate with T_3 for individual H II regions in single galaxies, on average $[\text{O III}]\lambda 5007$ luminosity depends on T_3 according to the $O3$ vs. T_3 relation shown in Figure 2. Thus, hotter H II regions have more luminous $[\text{O III}]\lambda 5007$ on average below $T_3 < 14,000$ K ($\log(T_3/K) < 4.15$). On the other hand, at $T_3 > 14,000$ K, hotter H II regions typically have *lower* $[\text{O III}]\lambda 5007$ luminosity. Thus, in the *hiionly* model, there is a positive bias in T_3^{gal} at $T_3^{\text{gal}} < 14,000$ K due to the increased weight of hotter H II regions that have both higher $O3$ and lower $Q3$. At $T_3^{\text{gal}} = 14,000 - 19,000$ K, cooler H II regions with higher $O3$ and higher $Q3$ contribute more to T_3^{gal} because the steepness of the dropoff in the $O3$ vs. T_3 relation dominates over the decrease in $Q3$ with increasing T_3 in this regime. However, the exponential nature of the $Q3$ vs. T_3 relation eventually dominates over the falling $O3$ vs. T_3 relation, leading to a sharp increase in the T_3^{gal} bias above

$T_3 = 19,000$ K as hotter H II regions again receive more weight in the global T_3^{gal} calculation.

In the *SDSSstack* model, the T_3^{gal} bias mimics that of the *hiionly* model at $T_3^{\text{gal}} < 12,000$ K, the regime where H II regions and DIG follow similar excitation sequences in the O3N2 diagram. At $T_3^{\text{gal}} > 12,000$ K, the DIG and H II region sequences diverge in the O3N2 diagram, such that DIG O3 continues increasing with T_3 whereas H II region O3 turns over. This difference in the DIG O3 vs. T_3 behavior leads to ΔT_3 that is always positive in the *SDSSstack* model that includes DIG emission. Similar to the *hiionly* model, the exponential dependence of Q3 on T_3 begins to dominate at $T_3^{\text{gal}} > 19,000$ K due to flux-weighting effects, as evidenced by a sharp increase in ΔT_3 .

The T_2^{gal} bias for the *hiionly* model ranges from $-1,000$ K to $+500$ K. The bias can again be understood as a consequence of combining light from H II regions with a range of temperatures. The strong-to-auroral line ratio $Q2 = [\text{O II}]\lambda\lambda 3726,3729/\lambda\lambda 7320,7330$ depends on T_2 according to equation 10. As before, the global bias is determined by the interplay of the auroral-line Q2 vs. T_2 and strong-line O2 vs. T_2 relations. The O2 vs. T_3 relation is shown in Figure 2. Since T_2 is linearly dependent on T_3 , the O2 vs. T_2 relation will have the same shape as the O2 vs. T_3 relation modulo a linear transform to the temperature axis. At $T_2 < 10,000$ K, hotter H II regions have both higher $[\text{O II}]\lambda\lambda 3726,3729$ luminosity and lower Q2, leading to a positive ΔT_2 , although this bias is fairly small since the O2 vs. T_2 relation slope is not extreme in this regime. At $T_2 = 10,000 - 15,000$ K, the O2 vs. T_2 relation drops off steeply such that cooler H II regions have higher $[\text{O II}]\lambda\lambda 3726,3729$ luminosity and dominate the T_2^{gal} measurement, leading to a negative ΔT_2 that reaches $-1,000$ K at $T_2^{\text{gal}} = 14,000$ K. The exponential fall of Q2 with increasing T_2 begins to dominate at $T_2^{\text{gal}} > 15,000$ K, leading to a rapid increase in ΔT_2 .

The T_2^{gal} bias for the *SDSSstack* model is always negative and can be large, underestimating T_2^{HII} by as much as 2,000 K. There are two effects driving the difference between the T_2^{gal} bias of the *SDSSstack* and *hiionly* models. First, inclusion of DIG emission significantly increases the $O2^{\text{gal}}$ ratio. However, $\Delta O2$ is not a strong function of $O3N2^{\text{gal}}$ (a good proxy for electron temperature), and will thus not have a large effect on the T_2^{gal} bias, which is sensitive to the slope of the $\Delta O2$ vs. $O3N2^{\text{gal}}$ relation rather than the normalization. When the slope of the $\Delta O2$ vs. $O3N2^{\text{gal}}$ relation is flat, the bias in $O2^{\text{gal}}$ is not a function of electron temperature and thus does not strongly affect the globally-derived T_2^{gal} . The dominant factor separating the *SDSSstack* and *hiionly* models in ΔT_2 is our inference that DIG T_2 is 15% lower than H II region T_2 at fixed metallicity. This choice was motivated by differences between observations and a model in which DIG and H II region T_2 was always equal. An offset between model and stacks of SDSS galaxies was observed in all plots involving T_2 but was not present in plots that only include T_3 , suggesting that DIG T_2 is not equivalent to H II region T_2 at fixed metallicity. The difference

in DIG and H II region T_2 effectively shifts the globally-derived T_2^{gal} lower and results in a large negative ΔT_2 when DIG emission is included, ultimately resulting in a significant underestimation of T_2^{HII} from global galaxy spectra at all metallicities.

We fit ΔT_3 and ΔT_2 as a function of T_3^{gal} and T_2^{gal} , respectively, using a fourth-order polynomial:

$$\Delta T_e = c_0 + c_1 y + c_2 y^2 + c_3 y^3 + c_4 y^4, \quad (26)$$

where T_e is T_3 or T_2 , and $y = T_3^{\text{gal}}/10^4$ K or $T_2^{\text{gal}}/10^4$ K. The best-fit coefficients are presented in Table 1.

4.3. Biases in direct-method metallicity measurements

We use the same method employed above to characterize the bias in the direct-method oxygen abundance as inferred from global galaxy spectra. Since it is common for only one auroral line to be measured in a galaxy spectrum, we evaluate the bias in metallicity for the cases where (1) both T_3^{gal} and T_2^{gal} are measured directly from the galaxy spectrum, (2) only T_3^{gal} is measured and T_2^{gal} is inferred from the T_2 - T_3 relation of equation 12, and (3) only T_2^{gal} is measured and T_3^{gal} is inferred from the T_2 - T_3 relation of equation 12. The bias in global direct-method metallicity, $\Delta \log(\text{O}/\text{H})$, as a function of direct-method metallicity inferred from global galaxy spectra is presented in Figure 17 for each of these three cases. The bias is always calculated with respect to the median direct-method metallicity of the individual H II region distribution in each mock galaxy. Having determined the biases in both strong-line ratios and electron temperatures, we can elucidate the origin of direct-method oxygen abundance biases. Once again, we separately report the results from the *hiionly* and *SDSSstack* models to understand the additional effects that DIG contamination introduces.

The formulae for the calculation of the ionic abundances O^+/H and O^{++}/H (equations 13 and 14) are functions of both the strong-line ratio of each ion (O2 or O3) and the corresponding ionic electron temperature (T_2 or T_3). O^+/H has a linear dependence on O2 and O^{++}/H has a linear dependence on O3 such that a bias in either of these strong-line ratios will result in an equivalent bias in the corresponding ionic abundance. We plot the temperature dependence of the ionic abundance formulae at fixed strong-line ratio for a range of T_3 and T_2 in Figure 18. At high temperature (low metallicity) the temperature dependence is weak such that even a large bias in electron temperature does not significantly bias the ionic abundance. The temperature dependence is strong at low temperature (high metallicity) such that even a moderate bias of ± 500 K can change the ionic abundance by ~ 0.2 dex. How much the bias in a particular ionic abundance affects the total oxygen abundance depends on the relative population of oxygen in O^+ and O^{++} , which is a function of metallicity.

We first focus on the case where both T_3^{gal} and T_2^{gal} are measured directly from the galaxy spectrum. In the low-metallicity limit ($12 + \log(\text{O}/\text{H})_{T_2, T_3}^{\text{gal}} \lesssim 8.0$), most of the oxygen is in O^{++} such that changes in O^+/H will have a negligible effect on the total oxygen abundance. The global metallicity bias is thus dominated by biases

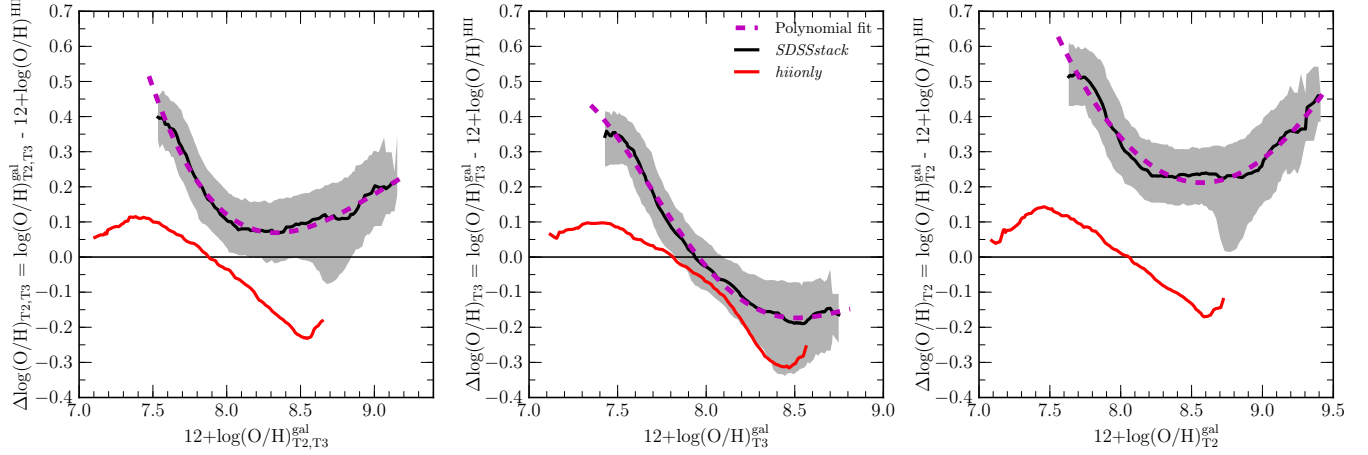


Figure 17. The difference between the global galaxy direct-method metallicity, inferred from the observed galaxy spectrum, and the median metallicity of the H II region distribution. We show the bias in global galaxy metallicity for three cases: both T_3 and T_2 are measured from the galaxy spectrum (left panel); only T_3 is measured directly and T_2 is estimated using the T_2 - T_3 relation of equation 12 (middle panel); and only T_2 is measured directly and T_3 is estimated using equation 12 (right panel). Lines and shading are the same as in Figure 15. The best-fit fourth-order polynomial coefficients are presented in Table 1.

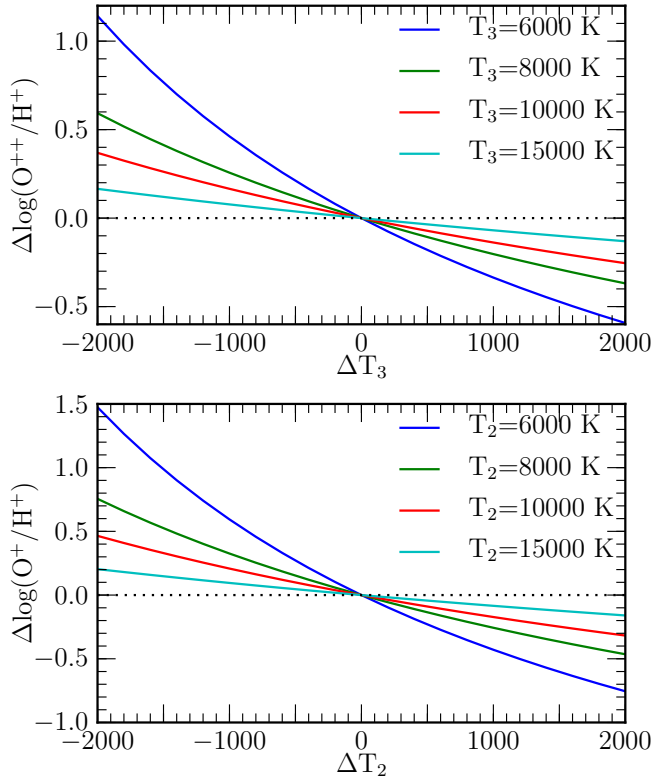


Figure 18. Temperature dependence of the ionic oxygen abundances at fixed strong-line ratio. The top panel displays the change in O^{++}/H^+ with changes in T_3 according to equation 14 for a range of T_3 as indicated by the solid lines where color corresponds to the T_3 value. The bottom panel shows the same relationship for O^+/H^+ and T_2 according to equation 13. In each panel, the dotted line indicates zero change in the ionic abundance.

in $O3^{\text{gal}}$ and T_3^{gal} in this regime. At low metallicity (high $O3N2^{\text{gal}}$), $O3^{\text{gal}}$ is biased high by $< +0.05$ dex in the *hiionly* model, contributing only a small amount to $\Delta\log(O/H)_{T2,T3}$. T_3^{gal} is biased ~ 500 K low at low metallicity in the *hiionly* model. When combined, these two effects lead to a bias in the direct-method metallicity of $+0.1$ dex in the low-metallicity limit from combi-

nations H II regions alone. The *SDSSstack* model has a positive T_3^{gal} bias that increases sharply at the low-metallicity extreme. While higher T_3^{gal} will bias the global metallicity low, the temperature dependence of direct-method metallicity is weakest at high temperature. The metallicity bias for the *SDSSstack* model at low metallicity is instead dominated by the positive bias in $O3^{\text{gal}}$, which reaches $+0.3$ dex in the low-metallicity limit. The strong-line bias leads to an overestimate of galaxy direct-method metallicity that grows from $+0.1$ dex at $12 + \log(O/H)_{T2,T3}^{\text{gal}} = 8.0$ to $+0.4$ dex at $12 + \log(O/H)_{T2,T3}^{\text{gal}} = 7.6$.

In the high-metallicity limit ($12 + \log(O/H)_{T2,T3}^{\text{gal}} \gtrsim 8.5$), O^+ is the most numerous ionic form of oxygen and biases in $O3^{\text{gal}}$ and T_3^{gal} will be subdominant drivers of $\Delta\log(O/H)_{T2,T3}$. In the *hiionly* model, $O2^{\text{gal}}$ is relatively unbiased at all metallicities while T_2^{gal} is biased high by ~ 250 K at $T_2^{\text{gal}} \sim 7500$ K (high metallicity). While the T_2^{gal} bias is not large, the direct-method metallicity is highly sensitive to temperature changes at low temperature, such that a bias of only ~ 250 K in T_2 leads to a bias in the direct-method metallicity of -0.2 dex. When DIG emission is included in the *SDSSstack* model, $O2^{\text{gal}}$ is biased high and T_2^{gal} is biased low, $\Delta\log(O/H)_{T2,T3}$ to $+0.2$ dex at $12 + \log(O/H)_{T2,T3}^{\text{gal}} = 9.0$. Including DIG emission leads to significantly different behavior of $\Delta\log(O/H)$ from the case where emission from H II regions alone is considered. Because DIG exhibits higher low-ionization line ratios and lower T_2 than H II regions, DIG contamination in global galaxy spectra leads to an overestimate of $12 + \log(O/H)^{\text{HII}}$, the median metallicity of the H II region population.

The cases where only one ionic temperature is measured directly can be understood as modulations of the case where both T_2^{gal} and T_3^{gal} are known. Biases from strong-line ratios will remain the same, while the bias arising from the unknown temperature will differ. We note that the *hiionly* bias shows little change when only one ionic temperature is known. This consistency occurs

because H II regions closely follow the the T_2 - T_3 relation of equation 12 from which the unknown temperature is inferred.

The case where only T_3^{gal} is measured from the galaxy spectrum is shown in the middle panel of Figure 17. In this case, T_2^{gal} is estimated using the T_2 - T_3 relation of equation 12. While H II regions follow this relation, ionic temperature measurements from global galaxy spectra show that galaxies do not, instead having lower T_2 at fixed T_3 than H II regions. Assuming that galaxies follow the same ionic temperature relation as H II regions is a common assumption in the literature (e.g., Izotov et al. 2006; Berg et al. 2012; Jones et al. 2015). For the *SDSSstack* model, this assumption leads to an overestimate of T_2^{gal} by 1,000 – 1,500 K when inferred using equation 12. This discrepancy has little effect at low metallicity where O^+ is negligible, but leads to a negative bias in oxygen abundance of -0.15 dex at $12+\log(O/H)_{T_3}^{\text{gal}} = 8.4 - 8.7$.

The right panel of Figure 17 shows the case where only T_2^{gal} is measured directly from the galaxy spectrum. While this case is less common in the literature for individual galaxies than the case where only $[O\text{ III}]\lambda 4363$ is detected, stacked spectra of high-metallicity galaxies often only yield $[O\text{ II}]\lambda\lambda 7320, 7330$ detections (Liang et al. 2007; Andrews & Martini 2013; Brown et al. 2016; Curti et al. 2017). In this case, T_3^{gal} is underestimated by $\sim 2,000$ K at all values of T_2^{gal} when T_3^{gal} is inferred from the T_2 - T_3 relation of equation 12. This incorrect T_3^{gal} value leads to a large $\Delta\log(O/H)_{T_2}$ value of $+0.3$ to $+0.5$ dex at $12+\log(O/H)_{T_2}^{\text{gal}} < 8.0$ for the *SDSSstack* model. Overestimating T_3^{gal} by 2,000 K leads to an overestimate of O^{++}/H by $\sim +0.6$ dex because of the temperature dependence of O^{++}/H at low T_3 , as shown for $T_3=6,000$ K in the top panel of Figure 18. While O^{++} is not the main form of oxygen in this high-metallicity, low-temperature regime, the $\sim +0.6$ dex overestimate of O^{++}/H causes O^{++}/H to contribute strongly enough to affect the total oxygen abundance. Thus, the global bias in direct-method metallicity is higher at all metallicities when T_2^{gal} is known and T_3^{gal} is inferred from an H II region T_2 - T_3 relation than when both T_2^{gal} and T_3^{gal} are measured directly. The *SDSSstack* model predicts that the additional bias when only T_2^{gal} is known compared to the case when both T_2^{gal} and T_3^{gal} are measured is ~ 0.15 dex and is nearly constant with metallicity. This value is in excellent agreement with the observation of Andrews & Martini (2013) that the metallicities of their M_* -binned stacks were 0.18 dex higher on average if the metallicity was calculated using T_2^{gal} alone instead of both T_2^{gal} and T_3^{gal} (see their Figure 6). We note that if a T_2 - T_3 relation fit to galaxy stacks instead of H II regions was used to infer the unknown ionic temperature, then the bias when only one temperature is measured would closely match the bias shown in the left panel of Figure 17 where both ionic temperatures are known. The differences between the three panels arise solely because galaxies do not fall on the H II region T_2 - T_3 relation.

We fit the direct-method metallicity bias in each of the three ionic temperature cases with a fourth-order poly-

nomial:

$$\Delta\log(O/H) = c_0 + c_1z + c_2z^2 + c_3z^3 + c_4z^4, \quad (27)$$

where $z = 12+\log(O/H)^{\text{gal}} - 8$ for the appropriate electron temperature case (T_2 and T_3 , T_2 only, or T_3 only). The best-fit coefficients are presented in Table 1. These functions may be used to correct direct-method metallicities of galaxies with measured auroral lines in order to obtain a metallicity measurement that is characteristic of the H II region population.

4.4. Corrections for individual galaxies or unrepresentative samples

We have presented best-fit polynomials that allow for the correction of strong-line ratios, electron temperatures, and direct-method oxygen abundances obtained from global galaxy spectra to values that are representative of the distribution of H II regions in each galaxy. These corrections are based on a model that is matched to the typical $z \sim 0$ star-forming population as represented by stacks of SDSS galaxies from AM13, B16, and C17. The best-fit polynomials presented above thus provide robust corrections for samples of galaxies that are also representative of the typical local star-forming population, that is, having $f_{\text{DIG}}=0.55$ on average. It may be of interest, however, to correct the line ratios, temperatures, and oxygen abundances of individual galaxies that do not fall on the mean relations, or to provide corrections for an unrepresentative sample of galaxies, as would be necessary for galaxies that do not follow the mean M_* -SFR relation when investigating the SFR dependence of the MZR. We provide a recipe for correcting individual galaxies or unrepresentative samples for which $f_{\text{DIG}}=0.55$ is not appropriate in Appendix A.

5. APPLICATION TO THE $Z \sim 0$ MZR AND FMR

In this section, we show examples of how the biases determined from our model framework can be used to correct local metallicity scaling relations, removing the effects of flux-weighting and DIG contamination. We apply corrections to the $z \sim 0$ direct-method MZR and FMR, and investigate the effects of strong-line ratio biases on the MZR when using strong-line metallicity calibrations. We additionally demonstrate how the expected decrease in f_{DIG} with increasing SFR can explain the observed trends in strong-line ratio at fixed direct-method metallicity from Brown et al. (2016) and Cowie et al. (2016).

5.1. The $z \sim 0$ direct-method MZR

We investigate the effects of the biases in direct-method galaxy metallicity presented in Section 4.3 on measurements of the local MZR. Using measurements from composite spectra of local star-forming galaxies in bins of M_* , AM13 presented the local MZR over three orders of magnitude in M_* and an order of magnitude in $12+\log(O/H)$. The increase in sensitivity from stacking enabled AM13 to probe an order of magnitude lower in M_* ($\log(M_*/M_\odot) = 7.5$) than most previous MZR studies based on strong-line metallicities (e.g., Tremonti et al. 2004), and measure direct-method metallicities representative of galaxies with such a wide dynamic range in properties for the first time.

The direct-method MZR from AM13 stacks is presented in the top panel of Figure 19. We show both the

MZR using direct-method metallicities as inferred from the stacked spectra without correcting for any biases (gray points) and the galaxy metallicities after correcting for the biases presented in Section 4.3 (green points). The original AM13 metallicities were recalculated using our methodology, which includes updated atomic data. Accordingly, our AM13 metallicities prior to correction are systematically shifted with respect to those reported in AM13, yielding ~ 0.1 dex higher metallicities in the highest mass bins, and slightly lower metallicities in the lowest mass bins. We followed the methodology of AM13 to estimate $12+\log(\text{O}/\text{H})$ for those high-mass stacks that do not have clean detections of $[\text{O III}]\lambda 4363$ by adjusting the metallicity as calculated using T_2 only by an amount equal to the median difference between $12+\log(\text{O}/\text{H})_{T_2,T_3}$ and $12+\log(\text{O}/\text{H})_{T_2}$ (see their Section 3.2 and Figure 6). We find this median offset to be -0.24 dex, slightly larger in magnitude than the offset of -0.18 dex reported in AM13 owing to the different atomic data and ionic abundance determinations used here. The values of $12+\log(\text{O}/\text{H})_{T_2}$ prior to this offset adjustment for stacks with T_2 only are shown as unfilled gray squares. Correcting the stacks with no T_3 measurement yields an uncorrected MZR that shows no obvious break at the point where $[\text{O III}]\lambda 4363$ is no longer cleanly detected.

Corrected direct-method metallicities are obtained by applying the best-fit corrections shown in Figure 17. Stacks with measurements of both $[\text{O III}]\lambda 4363$ and $[\text{O II}]\lambda\lambda 7320, 7330$ are corrected using the $12+\log(\text{O}/\text{H})_{T_2,T_3}$ fit, while stacks with only $[\text{O II}]\lambda\lambda 7320, 7330$ are corrected by applying the $12+\log(\text{O}/\text{H})_{T_2}$ fit to the uncorrected $12+\log(\text{O}/\text{H})_{T_2}$ prior to the offset adjustment. Our models naturally account for the offset in metallicity when only T_2 is measured without the need for an ad hoc adjustment to the normalization as in AM13. It is important to note that the range of uncorrected galaxy metallicities ($12+\log(\text{O}/\text{H})_{T_2,T_3}^{\text{gal}} = 7.8 - 8.7$; $12+\log(\text{O}/\text{H})_{T_2}^{\text{gal}} = 8.9 - 9.1$) fall within the range of the models and do not fall close to the lowest or highest model galaxy metallicities where extrapolations are heavily relied upon. Thus, our choice of extrapolations does not strongly impact our results. The bottom panel of Figure 19 shows the difference between the uncorrected and corrected AM13 metallicities, where the original uncorrected AM13 metallicities have been recalculated with our updated atomic data.

We fit the uncorrected and corrected direct-method MZRs with the asymptotic logarithmic formula of Moustakas et al. (2011), also used by AM13:

$$12+\log(\text{O}/\text{H}) = 12+\log(\text{O}/\text{H})_{\text{asm}} - \log \left[1 + \left(\frac{M_{\text{TO}}}{M_*} \right)^\gamma \right]. \quad (28)$$

This function is a power law of slope γ at low stellar masses, and approaches the asymptotic metallicity $12+\log(\text{O}/\text{H})_{\text{asm}}$ at high stellar masses, where the turnover mass M_{TO} controls the transition point between the two behaviors. The best-fit values for the uncorrected AM13 direct-method MZR are $[12+\log(\text{O}/\text{H})_{\text{asm}}, M_{\text{TO}}, \gamma] = [8.87 \pm 0.03, 8.99 \pm 0.09, 0.67 \pm 0.02]$ (compare to $[8.80, 8.90, 0.64]$ in

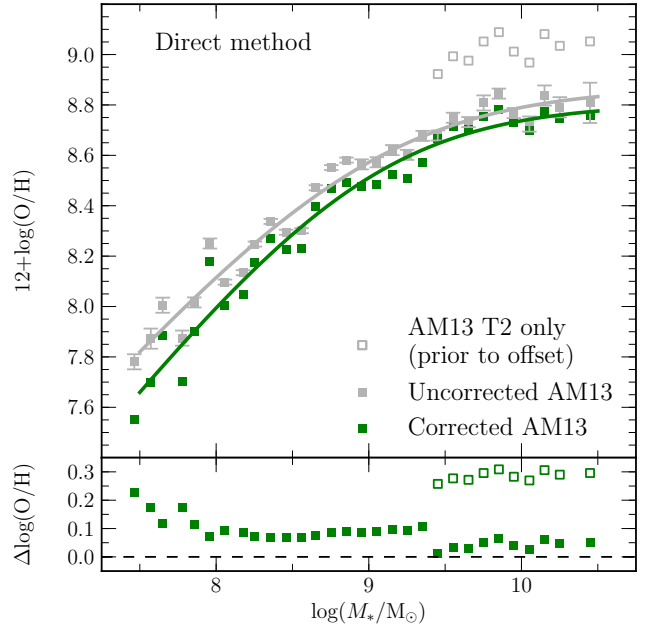


Figure 19. TOP: The direct-method MZR for stacks of SDSS star-forming galaxies in bins of M_* from AM13. Filled gray squares use uncorrected AM13 metallicities recalculated using updated atomic data, while filled green squares show the metallicities after correcting for the effects of flux-weighting and DIG emission. Error bars on the uncorrected points only include measurement uncertainties, and would thus be identical for the corrected points. Hollow gray squares present $12+\log(\text{O}/\text{H})_{T_2}$ for stacks with only T_2 estimates, prior to offsetting to account for the difference between $12+\log(\text{O}/\text{H})_{T_2}$ and $12+\log(\text{O}/\text{H})_{T_2,T_3}$. The gray and green lines show the best-fit MZR function of Moustakas et al. (2011) (equation 28) using uncorrected and corrected metallicities, respectively. The corrected MZR displays a lower normalization and steeper low-mass slope than before correction. BOTTOM: The difference between uncorrected and corrected metallicities as a function of M_* . Hollow points present $\Delta\log(\text{O}/\text{H})$ between uncorrected $12+\log(\text{O}/\text{H})_{T_2}$ prior to applying the offset and the corrected metallicity. The corrections produced by our models naturally account for the offset between $12+\log(\text{O}/\text{H})_{T_2}$ and $12+\log(\text{O}/\text{H})_{T_2,T_3}$.

AM13), and the fit is shown as a gray line in Figure 19. The best fit to the corrected AM13 direct-method MZR is shown as a green line, with best-fit parameters $[12+\log(\text{O}/\text{H})_{\text{asm}}, M_{\text{TO}}, \gamma] = [8.80 \pm 0.02, 8.98 \pm 0.08, 0.75 \pm 0.03]$.

We find lower corrected metallicities at all stellar masses compared to the uncorrected metallicities (reflected in the 0.07 dex lower $12+\log(\text{O}/\text{H})_{\text{asm}}$), with the lowest-mass bins displaying the largest shift. This trend results in a steeper low-mass slope of 0.75 after correcting for the effects of flux-weighting and DIG contamination, compared to a slope of 0.67 for the uncorrected AM13 MZR. Accurately determining the low-mass slope of the MZR is of primary importance since it is set by the scaling of outflow efficiency with stellar mass, as parameterized by the mass loading factor defined as the ratio of outflow rate and SFR, which in turn reflects the nature of galactic winds (Finlator & Davé 2008). In particular, energy-driven galactic winds predict a steeper low-mass slope than momentum-driven winds (Peeples & Shankar 2011). The turnover mass identifies the stellar mass at which galactic winds become inefficient and unable to remove sufficient material in large-scale outflows, and is unaffected by our corrections. In summary, correcting

for flux-weighting and DIG contamination results in a lower normalization and steeper low-mass slope of the $z \sim 0$ direct-method MZR, and these changes have a significance of $\sim 2\sigma$.

5.2. Strong-line MZR at $z \sim 0$

The direct-method MZR provides a robust measurement of the shape of the $z \sim 0$ MZR since it is constructed using a reliable metallicity determination that can be applied to a large number of galaxies through the stacking process. Nevertheless, we investigate the effects of biases in global galaxy line ratios on the MZR as determined using strong-line metallicity calibrations. Such calibrations have been widely applied in the local universe, and strong-line calibrations are currently the only method available to determine gas-phase metallicities of high-redshift galaxies due to the difficulty of detecting faint auroral lines at cosmological distances. Whenever investigating redshift evolution of the MZR, it is crucial that all samples being compared at least have metallicities determined using the same calibration to eliminate known systematic differences between various strong-line calibrations (Kewley & Ellison 2008). Correcting strong-line MZRs for biases can thus provide more robust determinations of the evolution of the MZR. However, potential evolution of physical conditions of star-forming regions with redshift may ultimately require a reevaluation of strong-line calibrations at high redshift (Steidel et al. 2014; Sanders et al. 2015; Shapley et al. 2015). Even so, eliminating observational biases from $z \sim 0$ strong-line MZR measurements provides a more robust baseline relative to which metallicity evolution can be inferred.

We analyze the $z \sim 0$ strong-line MZRs using measurements of strong-line ratios from the AM13 stacks. We investigate the effects of global galaxy strong-line ratio biases on the MZR using four widely-applied metallicity calibrations: two empirical calibrations (Pettini & Pagel 2004 N2 and O3N2; PP04N2 and PP04O3N2, respectively) and two theoretical calibrations (Kewley & Dopita 2002 N2O2 and Tremonti et al. 2004 R23; KD02N2O2 and T04R23, respectively). The original AM13 strong-line metallicities are calculated using the dust-corrected line fluxes appropriate to each calibration as reported in AM13. In order to determine the corrected AM13 strong-line metallicities, we first apply corrections to each strong-line indicator based on the best-fit polynomials presented in Figure 15 and then estimate strong-line metallicities using each calibration. The individual strong-line ratio biases in Figure 15 may be combined to provide a correction to any strong-line metallicity indicator. The uncorrected and corrected strong-line MZRs using each of the four calibrations are presented in the top row of Figure 20, while the bias in $\log(\text{O}/\text{H})$ is shown in the center row, and the bias in the strong-line ratio is presented in the bottom row. The best-fit corrected AM13 direct-method MZR is shown for comparison.

There is a large spread in the normalization of the MZR when using different strong-line calibrations, as first pointed out by Kewley & Ellison (2008). Empirical calibrations based on H II region samples with auroral-line measurements (PP04N2, PP04O3N2) yield metallicities that are ~ 0.3 dex lower than those obtained from theoretical calibrations based on photoionization models (KD02N2O2, T04R23). It is unsurprising that the empir-

ical calibrations produce metallicities that most closely match the direct-method AM13 MZR, since the calibration dataset is dominated by objects with direct-method metallicities. Correcting for flux-weighting and DIG effects does not reduce the offset between empirical and theoretical calibrations, but instead increases the magnitude of the disagreement by shifting the KD02N2O2 and T04R23 MZRs towards higher metallicity at fixed M_* . That the conflict between theoretical and empirical calibrations remains suggests that the disagreement between MZRs based on theoretical and empirical calibrations is not a result of observational biases in global galaxy spectra. Instead, the problem appears to be a manifestation of a long-standing disagreement in normalization of the metallicity scale between direct-method and theoretical strong-line calibrations observed for extragalactic H II regions (Kennicutt et al. 2003).

It is unclear which method provides a metallicity scale closer to the truth since there are potential systematic issues on both sides. Empirical direct-method calibrations may be biased towards lower metallicities due to the presence of temperature gradients and inhomogeneities within the ionized gas (Stasińska 2005; Bresolin 2007), although this problem primarily affects high-metallicity, low-temperature H II regions. Direct-method metallicities may indeed have a normalization bias, but have been shown to tightly correlate with metallicities determined from oxygen recombination lines with a slope of unity (Blanc et al. 2015) and an offset of ~ -0.2 dex. For photoionization models, it is difficult to determine the proper combination of input parameters and physical conditions that produce realistic H II regions because of degeneracies among parameters. Additionally, observed nearby H II regions often have filamentary gas structures and cluster stars distributed throughout the ionized gas (e.g., 30 Dor; Pellegrini et al. 2011), a very different geometry from the ionizing point source and uniform-density sphere or slab of gas utilized in most photoionization codes (Kewley & Dopita 2002; Gutkin et al. 2016).

All strong-line MZRs display a high-mass flattening, although this is more apparent with some calibrations than others. In general, the turnover mass is higher than that measured with the direct-method. The PP04N2 and PP04O3N2 turnover masses do not change significantly once the galaxy metallicities are corrected for flux-weighting effects and DIG contamination. In contrast, the KD02N2O2 and T04R23 MZRs have turnover masses that are shifted lower when using corrected metallicities, bringing the turnover mass into better agreement with that of the direct-method MZR.

AM13 found that various strong-line calibrations produce MZRs that have low-mass slopes much shallower than that of the direct-method MZR. We also find that all strong-line MZRs using uncorrected metallicities have low-mass slopes close to $\gamma \sim 0.3 - 0.4$, significantly shallower than the slope of 0.75 for the direct-method MZR. For all strong-line MZRs except PP04O3N2, correcting for flux-weighting effects and DIG emission yields steeper low-mass slopes. The KD02N2O2 and T04R23 slopes appear to be close to that of the direct-method MZR after correction, relieving some tension between the theoretical strong-line and direct-method MZR shapes.

In summary, after correction for flux-weighting effects and DIG contamination in global galaxy line ra-

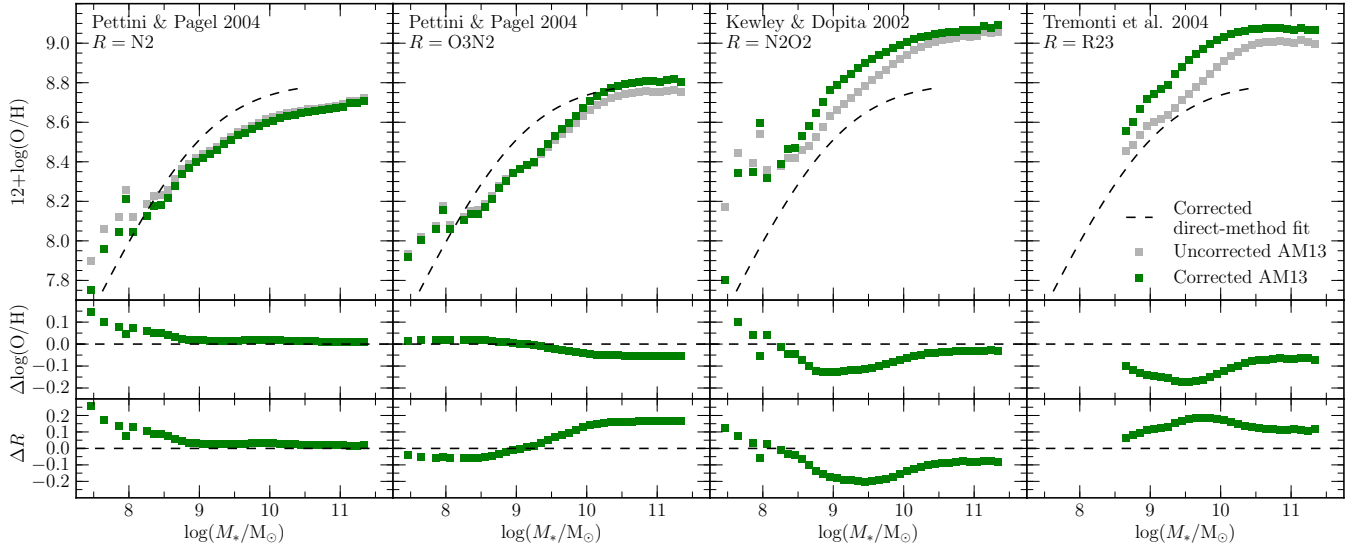


Figure 20. The MZR based on strong-line metallicities for the M_* stacks of AM13 is displayed in the top row. We show results for four commonly-used strong-line indicators: the empirical N2 and O3N2 calibrations of Pettini & Pagel (2004), the theoretical N2O2 calibration of Kewley & Dopita (2002), and the theoretical R23 calibration of Tremonti et al. (2004). In each panel, filled gray squares use the uncorrected strong-line ratio to infer the metallicity, while filled green squares utilize the strong-line ratio after correcting for flux-weighting effects and DIG emission. For reference, the corrected direct-method MZR best-fit function from Section 5.1 is shown as a dashed black line. The middle row displays the difference $\Delta\log(\text{O}/\text{H})$ between uncorrected and corrected metallicity, while the bottom row presents the difference ΔR between the uncorrected and corrected strong-line ratio. The bias in strong-line metallicity, primarily driven by DIG contamination, can exceed 0.1 dex.

tios, theoretical strong-line calibrations appear to match the direct-method MZR low-mass slope and turnover mass, but retain a large offset in normalization. Empirical strong-line calibrations provide a much closer match in normalization, but display higher turnover mass and shallower low-mass slope than those measured with the direct-method. Tensions between empirical and theoretical strong-line metallicities remain even after correcting for contamination from DIG emission.

5.3. The direct-method $z \sim 0$ FMR

The FMR as determined using direct-method metallicities will also be subject to biases from flux-weighting effects and DIG emission. We investigate the effects of flux-weighting and DIG contamination on the FMR using the M_* -SFR stacks of AM13. We recalculate the direct-method metallicities of the AM13 M_* -SFR stacks using the methodology in Section 2.3 that includes updated atomic data. In order to reproduce the results of AM13 using new atomic data, we calculate the original metallicities for those stacks with only T_2 measurements by subtracting the median difference between $12+\log(\text{O}/\text{H})_{T_2}$ and $12+\log(\text{O}/\text{H})_{T_2,T_3}$ from $12+\log(\text{O}/\text{H})_{T_2}$ for those stacks with measurements of both temperatures in the same SFR bin. This process yields the uncorrected AM13 FMR, shown in the left panel of Figure 21 as filled squares color-coded by SFR. The hollow squares show $12+\log(\text{O}/\text{H})_{T_2}$ for bins with T_2 only prior to the application of the offset.

We correct the AM13 metallicities of each M_* -SFR bin for the effects of flux-weighting and DIG contamination. The strength of the SFR dependence of the MZR may change after correcting for metallicity biases since f_{DIG} decreases as SFR increases at fixed M_* . Because f_{DIG} depends on SFR, we cannot use the *SDSSstack* model with $f_{\text{DIG}}=0.55$ to correct the metallicities in each M_* -

SFR bin, but must instead use a different f_{DIG} for each M_* -SFR bin. Accordingly, from the strong-line comparison sample that is selected following AM13, we select the subset of galaxies in a particular M_* -SFR bin and determine the median f_{DIG} using the method outlined in Section 3.1. We then produce a model for each M_* -SFR bin with the inferred f_{DIG} , while all other input parameters are the same as for the *SDSSstack* model. Using these new models, we fit the metallicity biases using equation 27 and apply these new fits to correct the direct-method metallicity of each M_* -SFR bin.

The corrected direct-method FMR for AM13 M_* -SFR stacks is presented in the right panel of Figure 21. The difference between the uncorrected and corrected $\log(\text{O}/\text{H})$ for each bin is presented in the bottom-right panel, where the hollow triangles show $\Delta\log(\text{O}/\text{H})$ between the corrected value and the uncorrected $12+\log(\text{O}/\text{H})_{T_2}$ before applying the offset. SFR dependence is still clearly present in the corrected direct-method FMR with higher-SFR galaxies having lower metallicities at fixed M_* , in agreement with other observations of the SFR dependence of the local MZR (Mannucci et al. 2010; Lara-López et al. 2010; Andrews & Martini 2013). However, the SFR dependence is weaker after correcting for biases in the metallicity estimates. At fixed M_* , $\Delta\log(\text{O}/\text{H})$ correlates with SFR such that galaxies with lower SFR have larger positive biases, while galaxies with high SFR have smaller positive or sometimes slight negative biases. This effect weakens the strength of the SFR dependence, occurring because DIG contamination causes galaxies to appear more metal rich when direct-method metallicities are employed due to increased low-ionization line strength and decreased T_2 . This bias is strongest in low-SFR galaxies in which DIG emission begins to dominate the line fluxes, leading to large corrections at low-SFR and smaller corrections as

SFR increases.

Mannucci et al. (2010) parameterized the SFR dependence with a planar projection using the parameter μ_α that is a linear combination of M_* and SFR:

$$\mu_\alpha = \log(M_*/M_\odot) - \alpha \times \log(\text{SFR}/M_\odot \text{ yr}^{-1}). \quad (29)$$

We evaluate the SFR strength of the direct-method FMR based on uncorrected and corrected metallicities by finding the value of α that minimizes the scatter around a linear fit in each case. We find that the uncorrected AM13 metallicities yield $\alpha = 0.70 \pm 0.015$ (compare to $\alpha = 0.66$ reported in AM13), while the SFR dependence is slightly weaker after correcting the metallicities, with $\alpha = 0.63 \pm 0.016$. The best-fit projections of the uncorrected and corrected direct-method FMRs are presented in the top and bottom panels of Figure 22. The smaller value of α after correcting the metallicities confirms that DIG contamination leads to an overestimation of the strength of the SFR dependence. However, this small decrease in α does not bring estimates using the direct-method into agreement with those made using strong-line metallicities. Investigations using strong-line indicators find much weaker SFR dependence ranging from $\alpha = 0.19$ (Yates et al. 2012) to $\alpha = 0.32$ (Mannucci et al. 2010).

5.4. B16 and Cowie et al. 2016 results are primarily caused by DIG contamination

B16 estimated direct-method metallicities of stacks of SDSS galaxies in bins of M_* and distance from the $z \sim 0$ M_* -SSFR relation (ΔSSFR), and showed that empirical strong-line metallicity calibrations have a systematic dependence on ΔSSFR . In particular, these authors found that galaxies with higher ΔSSFR display systematically higher N2, lower O3N2, and higher N2O2 values at fixed direct-method metallicity. B16 provided new calibrations that include a ΔSSFR term to account for this variation. Cowie et al. (2016) found similar results based on individual $z \sim 0$ SDSS galaxies with auroral-line detections, instead using $\text{H}\beta$ luminosity as the secondary parameter. These authors found that, at fixed direct-method metallicity, galaxies with higher $\text{H}\beta$ luminosity displayed higher N2, N2O2, and N2S2. Cowie et al. (2016) provided new strong-line calibrations including an additional $\text{H}\beta$ luminosity term, and interpreted the trends as an increase in both N/O and ionization parameter as SFR increases. Since SSFR and $\text{H}\beta$ luminosity are strongly correlated, it appears that the two studies observed the same phenomenon using different parameterizations.

In Figure 23, we show direct-method metallicity as a function of the strong-line ratios N2a, O3N2, N2O2, and N2S2. We plot the points from the M_* - ΔSSFR stacks of B16, color-coded by $\Delta\log(\text{SSFR})$. We recalculate uncorrected B16 direct-method metallicities using our methodology and updated atomic data presented in Section 2.3. Following AM13 and B16, we estimate the uncorrected metallicities of stacks for which only T_2 was measured by adjusting $12+\log(\text{O}/\text{H})_{T_2}$ by the median offset between $12+\log(\text{O}/\text{H})_{T_2}$ and $12+\log(\text{O}/\text{H})_{T_2,T_3}$ for those stacks with both T_2 and T_3 measurements in the same ΔSSFR bin. There are no stacks in the $\Delta\log(\text{SSFR}) = -0.25$ bin with T_3 estimates, thus the offset for T_2 -only metallicities cannot be determined in the same way for this

bin. B16 did not apply any offset to the metallicities of stacks in this lowest- ΔSSFR bin, instead adopting the value of $12+\log(\text{O}/\text{H})_{T_2}$ assuming the T_2 - T_3 relation followed by H II regions. To place the metallicities in the $\Delta\log(\text{SSFR}) = -0.25$ bin onto the same scale as those of the other bins, we apply the offset for the closest ΔSSFR bin ($\Delta\log(\text{SSFR}) = 0.25$) to $12+\log(\text{O}/\text{H})_{T_2}$. This solution is robust because, while the offset increases with decreasing ΔSSFR , the rate of change of the offset size with ΔSSFR decreases with decreasing ΔSSFR . The two bins closest in ΔSSFR to the $\Delta\log(\text{SSFR}) = -0.25$ bin have the smallest difference in offset of only 0.026 dex, so this solution should yield the uncorrected metallicities of the $\Delta\log(\text{SSFR}) = -0.25$ stacks within $\lesssim 0.02$ dex. It is important to note that these metallicities and strong-line ratios are inferred directly from the observed line fluxes of each stack, and have not been corrected for any biases.

We expect f_{DIG} to correlate with ΔSSFR since $\Sigma_{\text{H}\alpha}$, from which f_{DIG} is estimated, correlates strongly with SFR and SSFR, but does not show a strong dependence on M_* . It is therefore expected that f_{DIG} will change significantly across samples that vary greatly in SSFR and SFR, as in B16 and Cowie et al. (2016). If f_{DIG} changes significantly between bins of ΔSSFR or $\text{H}\beta$ luminosity, then the bias arising from DIG contamination will also vary systematically between such bins. We investigate the connection between DIG emission and the B16 and Cowie et al. (2016) results by determining the median f_{DIG} for subsets of the B16 sample. We begin with the SDSS strong-line comparison sample of individual galaxies that is selected in a nearly identical manner to the samples of AM13 and B16. We divide the full sample into subsamples in 0.5 dex-wide bins of $\Delta\log(\text{SSFR})$ using the parameterization of the mean $z \sim 0$ M_* -SSFR relation from B16. For each subsample, we determine $\Sigma_{\text{H}\alpha}$ and f_{DIG} for the individual galaxies and use the distribution of f_{DIG} values to infer the median f_{DIG} following the methods described in Section 3.1. We find the median f_{DIG} for bins centered on $\Delta\log(\text{SSFR}/\text{yr}^{-1}) = [-0.25, 0.25, 0.75, 1.25, 1.75]$ to be $f_{\text{DIG}}^{\text{med}} = [0.59, 0.53, 0.40, 0.28, 0.17]$. We create a set of five models that have all model parameters set to the same values as for the *SDSSstack* model except for f_{DIG} , which is set to the $f_{\text{DIG}}^{\text{med}}$ value for each ΔSSFR bin. In Figure 23, we plot the predicted global galaxy strong-line ratios and uncorrected direct-method metallicities for the models matched to each ΔSSFR bin. The values plotted for the models are the predicted observed values as would be inferred from global galaxy spectra before correcting for any biases.

For each line ratio, we find that the predicted global galaxy line ratios and uncorrected metallicities from the models are in excellent agreement with the observations of B16, although the models somewhat underpredict the deviation in N2O2 and N2S2 that is observed in the highest ΔSSFR bins. This disagreement at high ΔSSFR may indicate that the f_{DIG} - $\Sigma_{\text{H}\alpha}$ relation of equation 24 overpredicts f_{DIG} at high $\Sigma_{\text{H}\alpha}$ and may require some revision. Additionally, lines of constant f_{DIG} in the models match lines of constant ΔSSFR in the B16 stacks. It is therefore plausible that the systematic trends observed in B16 and Cowie et al. (2016) can be explained by variation of f_{DIG} with ΔSSFR and $\text{H}\beta$ luminosity.

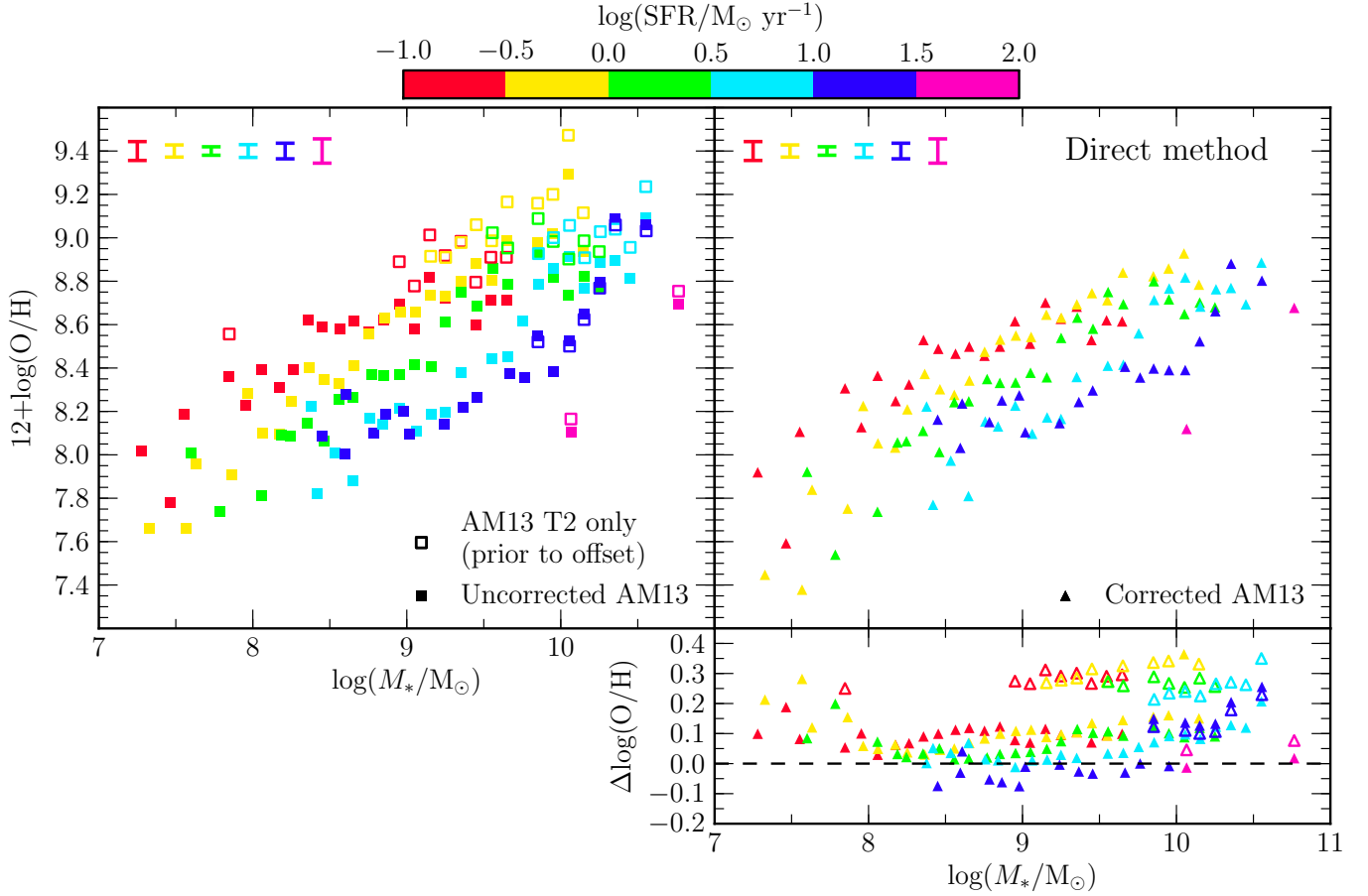


Figure 21. The direct-method FMR for M_* -SFR stacks from AM13, color-coded by SFR. Metallicities in the left panel have not been corrected for the effects of flux-weighting or DIG contamination. Filled squares denote points using the uncorrected AM13 metallicities, while hollow squares show $12+\log(\text{O}/\text{H})_{\text{T}2}$ assuming the T_2 - T_3 relation of equation 12 for those stacks with T_2 estimates but no T_3 estimates. In the right panel, metallicities have been corrected for flux-weighting effects and DIG contamination. The mean uncertainty in metallicity for each SFR bin is displayed in the upper left corner. Filled triangles in the bottom-right panel show the difference between the uncorrected and corrected direct-method metallicities, where hollow symbols show the difference between uncorrected $12+\log(\text{O}/\text{H})_{\text{T}2}$ and corrected $12+\log(\text{O}/\text{H})_{\text{T}2}$ for those bins with T_2 only. After correction, the SFR dependence in the FMR is weaker since there is a positive correlation between $\Delta\log(\text{O}/\text{H})$ and SFR at most stellar masses.

Following Sections 4.1 and 4.3, we fit the strong-line ratio and direct-method metallicity biases using equations 25 and 27, respectively, for each of the models matched to the B16 ΔSSFR bins. These best-fit polynomials are then used to correct the strong-line ratios and direct-method metallicities of the points in each B16 ΔSSFR bin for flux-weighting effects and DIG contamination. Figure 24 shows the corrected direct-method metallicities as a function of corrected strong-line ratios for the B16 M_* -SSFR stacks. The dependence on ΔSSFR of each strong-line ratio at fixed metallicity has decreased or disappeared once biases in both properties are accounted for. This resolution is most apparent in $\text{N}2\text{O}2$ and $\text{N}2\text{S}2$, which displayed the strongest ΔSSFR dependence prior to correction because DIG contamination affects $\text{O}2$ and $\text{S}2$ more strongly than $\text{O}3$ or $\text{N}2$.

We conclude that the majority of the systematic offsets as a function of ΔSSFR and $\text{H}\beta$ luminosity observed by B16 and Cowie et al. (2016) are a result of the decreasing importance of DIG emission as star formation intensity increases. Offsets in strong-line ratios at fixed direct-method metallicity occur because both the strong-line ratio and the direct-method metallicity are biased, pre-

dominantly due to DIG contamination. The spread in line ratio at fixed metallicity is largest at high metallicities ($12+\log(\text{O}/\text{H}) > 8.3$), where singly-ionized oxygen is the dominant ionic species, because DIG contamination strongly affects $\text{O}2$, T_2 , and, consequently, the O^+/H estimate. After accounting for f_{DIG} variation as a function of ΔSSFR , any remaining systematic offset as a function of ΔSSFR is small and does not require large systematic changes in the physical conditions of the H II region gas to explain. Since the B16 results appear to be equivalent to those of Cowie et al. (2016), a large systematic increase in N/O and ionization parameter with increasing SFR is not needed to explain the shift in strong-line ratios at fixed direct-method metallicity observed by Cowie et al. (2016).

5.5. Correcting the Curti et al. (2017) empirical calibrations

C17 recently used stacks of SDSS star-forming galaxies in bins of $\text{O}3$ and $\text{O}2$ to construct a set of fully-empirical strong-line calibrations for a range of commonly applied line ratios using direct-method metallicities. Utilizing a fully-empirical calibration dataset with a large dynamic

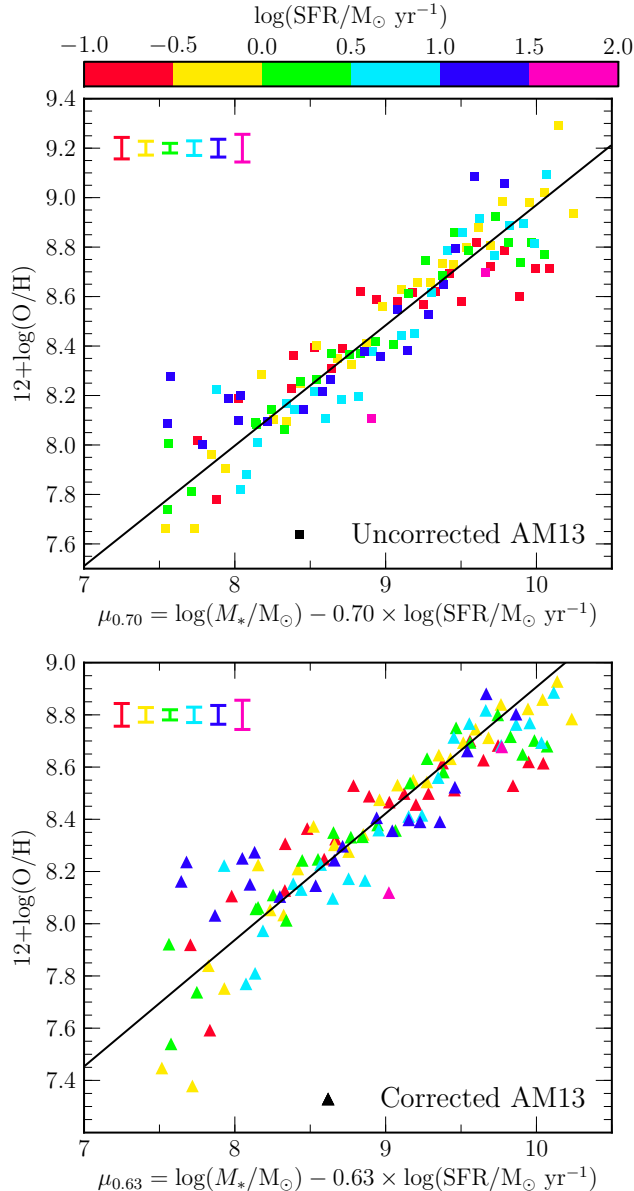


Figure 22. The planar projection of the FMR for AM13 M_* -SFR stacks. We use the FMR parameterization of (Mannucci et al. 2010), and show the FMR projection using uncorrected (top) and corrected (bottom) direct-method metallicities. In each panel, the black line shows the best-fit linear relation around which the scatter is minimized for the best-fit value of α . The value of the parameter α that minimizes the scatter around the plane was found to be $\alpha = 0.70 \pm 0.015$ when using uncorrected metallicities and $\alpha = 0.63 \pm 0.016$ after correction. Correcting for flux-weighting effects and DIG contamination slightly decreases the strength of the SFR dependence of the FMR. Error bars in the upper left corner show the mean uncertainty in $12+\log(\text{O}/\text{H})$ for each SFR bin.

range in metallicity improves upon past metallicity calibrations based upon galaxy spectra, which required the use of photoionization models at high metallicities where auroral lines are not detected for individual SDSS galaxies (Maiolino et al. 2008). While the C17 calibrations can be used over a wider range of metallicities than any other empirical calibration to date, both the direct-method metallicities and strong-line ratios used in the calibrations are subject to biases from flux-weighting effects and

DIG contamination as described in this work. In order to use the C17 calibrations to estimate the characteristic metallicity of the star-forming regions in galaxies by removing DIG contamination or flux-weighted combination effects, we recommend first using the observed uncorrected galaxy line ratios to determine the uncorrected metallicity, then correcting the metallicity inferred from the C17 calibrations using the fit to the bias in $12+\log(\text{O}/\text{H})_{\text{T2,T3}}$ (left panel of Figure 17). The best-fit coefficients are given in Table 1. This method will yield robust corrected metallicities that are representative of the distribution of H II region metallicities galaxies.

6. IMPLICATIONS FOR HIGH-REDSHIFT STUDIES

The MZR is known to evolve with redshift such that galaxies have lower metallicities at fixed stellar mass as redshift increases (e.g., Erb et al. 2006; Maiolino et al. 2008; Steidel et al. 2014; Troncoso et al. 2014; Sanders et al. 2015; Onodera et al. 2016). High-redshift metallicity studies have relied nearly uniformly on strong-line calibrations to estimate metallicity because of the difficulty of detecting faint auroral lines at $z > 1$. We have shown how contamination from DIG emission can affect strong-line ratios and thus impact strong-line metallicity estimates. Correcting for these biases can lead to significant changes in the inferred shape of the local MZR. It is of interest to consider what effects DIG contamination might have on the interpretation of high-redshift strong-line ratios.

High redshift galaxies have both smaller size (van der Wel et al. 2014) and higher SFR (Whitaker et al. 2014; Shivaei et al. 2015) at fixed M_* than $z \sim 0$ galaxies on average. Thus, typical $\Sigma_{\text{H}\alpha}$ values are much higher at high redshift than for local galaxies, with typical $z \sim 2$ galaxies having $\Sigma_{\text{H}\alpha}$ as high as local starburst galaxies. If the relationship between $\Sigma_{\text{H}\alpha}$ and f_{DIG} in equation 24 holds in the same form at high redshifts, then DIG emission should only account for a small fraction ($\sim 0-20\%$) of line emission in high-redshift star-forming galaxies. Based on the observations and simple model of Oey et al. (2007), we expect that DIG emission becomes increasingly less important with increasing redshift. Accordingly, correction of high-redshift galaxy line ratios should be performed using models that have $f_{\text{DIG}}=0$, such as the *hiionly* model. Additionally, the high SSFR of high-redshift galaxies and accompanying strong feedback may efficiently mix metals into the ISM such that the width of the H II region metallicity distribution is small. Such a scenario can explain the flat metallicity gradients observed in some high-redshift galaxies (Jones et al. 2013; Leethochawalit et al. 2016; Wang et al. 2017; Ma et al. 2017), and is similar to the inferred reason behind flatter gradients in lower mass local galaxies (Ho et al. 2015). If efficient metal distribution is a common feature at high redshift, then an appropriate model should also have smaller σ_{T} than the *SDSSstack* model.

If DIG emission is negligible at high redshift, it carries implications for the interpretation of the evolution of strong-line ratios. Galaxies at $z \sim 1-2$ display systematically different emission-line ratios from those typically observed in local galaxies, including an offset towards higher $[\text{O III}]/\text{H}\beta$ and/or $[\text{N II}]/\text{H}\alpha$ in the O3N2 diagram (Shapley et al. 2005; Liu et al. 2008; Kewley et al. 2013; Steidel et al. 2014; Shapley et al. 2015) and higher O3

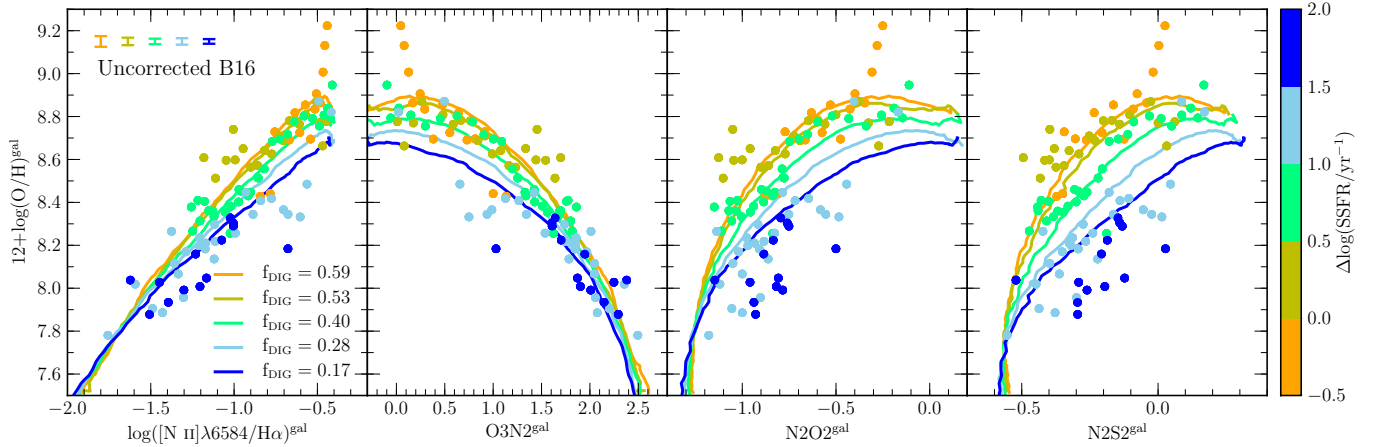


Figure 23. Global galaxy direct-method metallicity as a function of observed strong-line ratios for the M_* - Δ SSFR stacks of B16. Filled circles denote data from B16 color-coded by $\Delta\log(\text{SSFR})$, where the metallicities have been recalculated using updated atomic data. Metallicities and line ratios have not been corrected for flux-weighting effects or DIG contamination. Predicted global galaxy metallicity and uncorrected line ratios from models matched in f_{DIG} to each Δ SSFR bin are shown as solid lines of the corresponding color. Error bars in the upper left corner display the mean uncertainty in $12+\log(\text{O}/\text{H})$ for each $\Delta\log(\text{SSFR})$ bin.

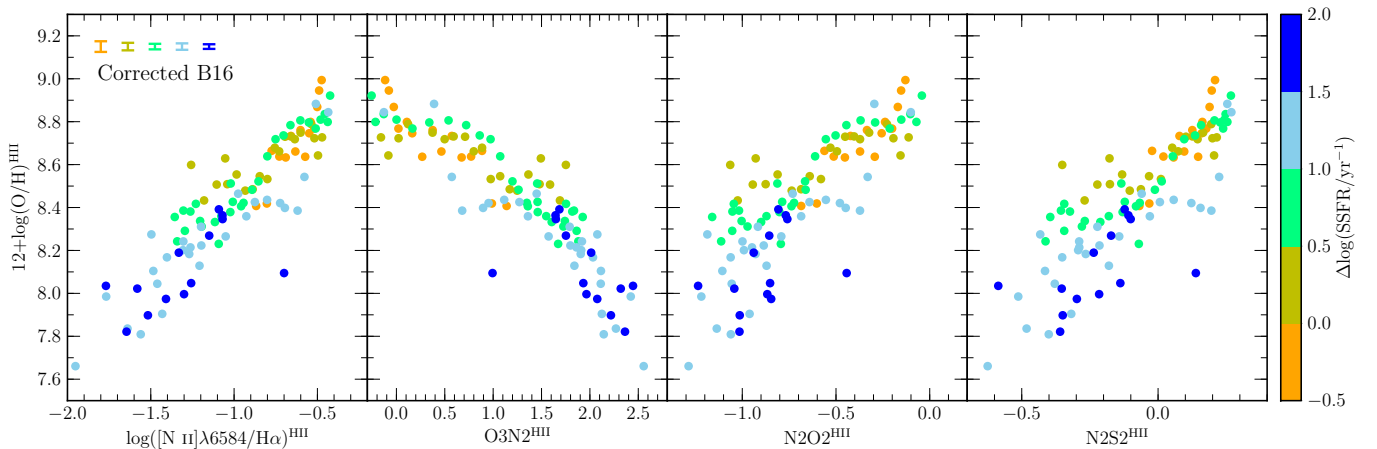


Figure 24. Corrected direct-method metallicity as a function of corrected strong-line ratios for the M_* - Δ SSFR stacks of B16. The effects of flux-weighting and DIG emission have been corrected for using the models shown in Figure 23. Correcting for DIG contamination reduces the scatter and systematic dependence on $\Delta\log(\text{SSFR})$ in these relations. Mean uncertainties on the metallicity for each Δ SSFR bin are shown in the upper left corner.

and $[\text{O III}]/[\text{O II}]$ values at fixed M_* than those observed in the local universe (Nakajima & Ouchi 2014; Onodera et al. 2016; Sanders et al. 2016). Such evolution in galaxy strong-line ratios may imply that local strong-line metallicity calibrations do not produce reliable metallicity estimates for high-redshift galaxies. By comparing the positions of high-redshift galaxies to those of local galaxies in diagnostic emission line diagrams, such evolution in strong-line ratios has been explained with evolving physical conditions of the ionized gas in H II regions, including gas density, ionization parameter, N/O abundance ratio, and shape of the ionizing spectrum. These interpretations have assumed that all of the emission line flux from both $z \sim 0$ and high-redshift galaxies originates from H II regions. If DIG emission is negligible in high-redshift star-forming galaxies, then the amount of inferred evolution in gas physical conditions such as the ionization parameter or hardness of the ionizing spectrum is likely overestimated because DIG emission tends to shift $z \sim 0$ global galaxy line ratios towards lower-excitation states compared to their constituent H II regions. It would then be more appropriate to compare high-redshift strong-line

ratios to those of individual H II regions instead of SDSS global galaxy spectra, or else first correct SDSS line ratios using the best-fit functions in Figure 15 before inferring evolution of H II region physical conditions. Such corrections are most important in line-ratio spaces that are significantly affected by DIG emission, such as the O3S2 and $[\text{O III}]/[\text{O II}]$ vs. M_* diagrams. Evolution in some ionized gas physical properties is still clearly required because DIG contamination (or lack thereof) cannot drive an offset in the O3N2 diagram (see Figure 4) for example.

Revealing the true DIG contribution to global galaxy line fluxes in high-redshift galaxies requires high-spatial-resolution emission-line maps to disentangle H II and DIG regions and determine their relative importance. The SDSS-IV MaNGA IFU survey has shown that line ratio maps from such a dataset can efficiently identify H II and DIG regions based on systematic changes in strong-line ratios as a function of $\text{H}\alpha$ surface brightness (Zhang et al. 2017). Similar high-redshift datasets should be able to identify significant DIG emission if the spatial resolution is sufficient to begin to resolve H II regions ($\lesssim 1$ kpc). Such maps have been obtained for

a small number of gravitationally-lensed objects (e.g., Jones et al. 2010; Yuan et al. 2011; Leethochawalit et al. 2016), but understanding the typical DIG contribution at high redshift necessitates larger samples spanning a wide range of galaxy properties. Confirming the nature of DIG emission at high-redshift is crucial for properly interpreting the evolution in galaxy strong-line ratios.

7. SUMMARY AND CONCLUSIONS

We have presented a set of empirically-motivated models that treat galaxies as a collection of multiple line-emitting regions with different physical properties. In addition to line emission from classical H II regions, these models incorporate DIG emission based on observed DIG strong-line ratio excitation sequences for the first time. We present the first measurement of DIG region excitation sequences over a range of excitation levels using data from the SDSS-IV MaNGA IFU survey (Zhang et al. 2017). Our model framework tracks contributions from DIG and H II regions to both strong and auroral optical emission lines. Previous models of galaxy line emission have treated galaxies as single H II regions with effective physical properties. Such descriptions of galaxy line emission are not sufficient to simultaneously match strong and auroral emission line properties in all line-ratio diagrams simultaneously. Including multiple H II regions with a range of excitation levels is required to reproduce the offset of global galaxy spectra in the T_2 - T_3 diagram (Figures 11 and 14; Pilyugin et al. 2010, 2012a; Andrews & Martini 2013). Furthermore, inclusion of DIG emission is necessary to properly reproduce galaxy excitation sequences in strong-line ratio diagrams, as evidenced by the distinct excitation sequences of H II regions, SDSS galaxies, and DIG regions in the O3N2, O3S2, and O3O2 diagrams (Figure 4).

We constructed the *SDSSstack* model in which DIG emission contributes 55% of the total Balmer emission, which provides a good description of typical $z \sim 0$ star-forming galaxies as represented by stacks of SDSS galaxies from Andrews & Martini (2013), Brown et al. (2016), and Curti et al. (2017). We find that the ionic temperature T_2 of DIG regions must be $\sim 15\%$ lower than T_2 of H II regions at fixed metallicity to match the strong-line ratios of SDSS stacks at fixed T_2 . This result may indicate that DIG region electron temperature systematically deviates from the electron temperature of associated H II regions, but may also represent a systematic effect in the process of combining line emission from multiple regions to form a global galaxy spectrum. Observations of auroral lines from DIG regions are needed to investigate this effect. When following this assumption about DIG T_2 , the *SDSSstack* model is in excellent agreement with SDSS stacks simultaneously in diagrams involving strong-line ratios, electron temperatures, and direct-method oxygen abundances.

We used the *SDSSstack* model to characterize biases in strong-line ratios, electron temperatures, and direct-method oxygen abundances as inferred from global galaxy spectra. Contamination of the global galaxy spectrum by DIG emission is the primary driver of biases in the *SDSSstack* model. DIG contamination tends to inflate the strength of low-ionization lines and lower the ionic temperature T_2 , making global galaxy spectra appear more metal-rich than is true of the metallicity dis-

tribution of star-forming regions within each galaxy. We quantified biases in these properties as the difference between the value inferred from a global galaxy spectrum and the median value of the H II region distribution of that property within each galaxy. We provided polynomial fits to the bias in each property (Table 1) that can be subtracted from global galaxy values to correct for the effects of flux-weighting and DIG contamination. The corrections presented in Section 4 are appropriate for samples of galaxies that are representative of the local star-forming population. A recipe for correcting individual galaxies or unrepresentative samples is given in Appendix A in which the *SDSSstack* model is generalized to have any value of f_{DIG} .

We applied these corrections to investigate observational biases in the $z \sim 0$ MZR and FMR. Nearly all metallicity calibrations are based on H II regions, including the direct-method and both empirical and theoretical strong-line metallicity calibrations. It is thus imperative that emission-line ratios of global galaxy spectra are corrected to be representative of the underlying H II region distribution before using calibrations based on H II regions to estimate metallicity. After correcting for flux-weighting effects and DIG contamination, we found that the $z \sim 0$ direct-method MZR has ~ 0.1 dex lower normalization and a slightly steeper low-mass slope ($\gamma = 0.75$) compared to the uncorrected MZR ($\gamma = 0.67$). These changes in the MZR shape have a significance of 2σ . The direct-method FMR displays slightly weaker SFR dependence after correction since DIG tends to make low-SFR galaxies appear more metal-rich, artificially strengthening the trend with SFR. We also investigated the effects of DIG contamination and flux-weighting on the local MZR as determined using multiple strong-line calibrations. DIG contamination can substantially affect the inferred shape of the MZR, flattening the low-mass slope and changing the normalization of theoretical calibrations in particular. Future studies of metallicity scaling relations can use the corrections given in this work to obtain robust galaxy metallicity estimates that are placed on a scale that can be compared directly to gas-phase metallicities reported by chemical evolution models.

We showed that the systematic trends in strong-line ratios at fixed direct-method metallicity with SSFR and $H\beta$ luminosity observed by Brown et al. (2016) and Cowie et al. (2016) can be explained almost entirely by a decreasing f_{DIG} with increasing SSFR. The importance of DIG is naturally expected to decrease with increasing star-formation intensity as classical H II regions occupy a larger volume of the ionized ISM and dominated line emission (Oey et al. 2007). This result demonstrates the importance in correcting for DIG contamination before inferring correlations of H II region physical properties with galaxy properties.

Our results have implications for the inferred evolution of H II region physical properties with redshift. If the trend between f_{DIG} and $\Sigma_{\text{H}\alpha}$ holds out to high redshifts, we expect that DIG emission is negligible in typical high-redshift galaxies that are more highly star-forming (Whitaker et al. 2014) and more compact (van der Wel et al. 2014) than their $z \sim 0$ counterparts at fixed M_* . Inferring evolution in H II region properties by comparing positions of high-redshift galaxies to those of global

galaxy spectra in strong-line ratio diagrams will likely overestimate the magnitude of evolution in, e.g., metallicity and ionization parameter. DIG contamination increases low-ionization line ratios in local star-forming galaxies, making them appear to have a lower level of excitation than the ionized gas in their constituent H II regions. Such an effect can artificially augment the offset between $z \sim 0$ and $z > 1$ star-forming regions in strong-line ratio diagrams, leading to incorrect assumptions about the evolution of ionized gas properties. A more robust comparison can be achieved by correcting $z \sim 0$ global galaxy observations for DIG contamination prior to comparing to high-redshift samples.

We stress that, in cases where it is desirable to measure properties that are characteristic of the H II regions within galaxies, deriving properties directly from observed line ratios of global galaxy spectra will not yield the desired result, but instead will be systematically biased. This is true of any dataset where the spectroscopic aperture (e.g., fiber, slit, etc.) contains light from multiple H II regions and the diffuse gas that exists between H II regions. Models of galaxy line-emission must incorporate both multiple emitting regions with a spread in properties and DIG emission in order to accurately match the emission-line properties of real galaxies. The increasing number of spatially-resolved spectroscopic surveys of local galaxies (e.g., MaNGA, SAMI, CALIFA) will allow for an accurate determination of the strong-line properties of DIG regions. Observational constraints are still needed on the auroral-line properties and electron temperatures of diffuse gas. We encourage future studies modeling the line emission of star-forming galaxies to avoid treating galaxies as single emitting regions with a set of effective properties, and instead design models that reflect the substructure and diversity observed in the ISM of real galaxies.

We acknowledge the importance of the First Carnegie Symposium in Honor of Leonard Searle for presentations and discussions without which this work would not have been possible. We acknowledge support from the NSF AAG grant AST-1312780 and grant NNX16AF54G from the NASA ADAP program. RY acknowledges support by NSF AAG grant AST-1715898. Funding for the Sloan Digital Sky Survey IV has been provided by the Alfred P. Sloan Foundation, the U.S. Department of Energy Office of Science, and the Participating Institutions. SDSS-IV acknowledges support and resources from the Center for High-Performance Computing at the University of Utah. The SDSS web site is www.sdss.org. SDSS-IV is managed by the Astrophysical Research Consortium for the Participating Institutions of the SDSS Collaboration including the Brazilian Participation Group, the Carnegie Institution for Science, Carnegie Mellon University, the Chilean Participation Group, the French Participation Group, Harvard-Smithsonian Center for Astrophysics, Instituto de Astrofísica de Canarias, The Johns Hopkins University, Kavli Institute for the Physics and Mathematics of the Universe (IPMU) / University of Tokyo, Lawrence Berkeley National Laboratory, Leibniz Institut für Astrophysik Potsdam (AIP), Max-Planck-Institut für Astronomie (MPIA Heidelberg), Max-Planck-Institut für Astrophysik (MPA Garching), Max-Planck-Institut für

Extraterrestrische Physik (MPE), National Astronomical Observatories of China, New Mexico State University, New York University, University of Notre Dame, Observatório Nacional / MCTI, The Ohio State University, Pennsylvania State University, Shanghai Astronomical Observatory, United Kingdom Participation Group, Universidad Nacional Autónoma de México, University of Arizona, University of Colorado Boulder, University of Oxford, University of Portsmouth, University of Utah, University of Virginia, University of Washington, University of Wisconsin, Vanderbilt University, and Yale University.

APPENDIX

APPENDIX A: A RECIPE FOR CORRECTING INDIVIDUAL GALAXIES OR UNREPRESENTATIVE SAMPLES

In Section 4, we presented polynomial functions that represent the median bias in strong-line ratios, electron temperatures, and direct-method metallicities when these properties are inferred directly from global galaxy spectra. However, the *SDSSstack* model with $f_{\text{DIG}}=0.55$, upon which the corrections in Section 4 are based, is only appropriate to apply to a sample of galaxies that is representative of the typical $z \sim 0$ star-forming population or to individual galaxies that fall near the mean relations. In this appendix, we present generalized results for a set of models in which f_{DIG} is varied from 0.0 (equivalent to the *hiionly* model) to 0.8, and supply a recipe to follow when applying these generalized results.

The relative contribution of DIG to Balmer emission, f_{DIG} , is inferred using $\Sigma_{\text{H}\alpha}$ and equation 24. Thus, the inferred f_{DIG} depends on the star formation properties of the galaxy, since $\Sigma_{\text{H}\alpha}$ will increase with increasing SFR. If a galaxy falls near the mean $z \sim 0$ M_* -SFR relation, or if the mean of a sample of galaxies lies near the mean local relation, then the corrections given in Section 4 may be applied. However, it is often of interest to study unrepresentative or extreme objects. For example, the sample of individual $z \sim 0$ SDSS galaxies with auroral-line detections have higher SFR at fixed M_* than is typical of the local star-forming population, and thus requires a lower median f_{DIG} value as demonstrated in Section 3.2. Investigating SFR dependence of local scaling relations requires dividing the local galaxy population into subsamples that are unrepresentative by construction, as in studies of the $z \sim 0$ FMR (Mannucci et al. 2010; Lara-López et al. 2010; Andrews & Martini 2013). Extreme local galaxies are also of interest because they may provide local analogs of the ISM conditions in high-redshift galaxies (e.g., Brown et al. 2014; Bian et al. 2016). We therefore provide results for models spanning a wide range in f_{DIG} so that flux-weighting effects and DIG contamination may be corrected for in individual galaxies and samples with a wide range in SFR and SSFR.

Following the methodology presented in Section 2.5, we create five models with the same input parameters as for the *SDSSstack* model ($N_{\text{HII}}=25$, $\sigma_{\text{T}}=0.07$ dex, $f_{\text{DIG}}=0.55$), except we vary the value of f_{DIG} from 0.0 to 0.8 in increments of 0.2. For this set of models, the bias in properties inferred from global galaxy spectra relative to the median properties of the distribution of H II

Table 2

Global galaxy bias coefficients for strong-line ratios (equation 25)

$\Delta O3$					
f_{DIG}	c_0	c_1	c_2	c_3	c_4
0.0	0.113	-0.0816	-0.0299	0.0341	-0.00443
0.2	0.124	-0.115	-0.0417	0.0663	-0.00948
0.4	0.134	-0.175	-0.0571	0.145	-0.0343
0.6	0.133	-0.211	-0.0364	0.167	-0.0437
0.8	0.139	-0.188	-0.0769	0.150	-0.0241
$\Delta O2$					
f_{DIG}	c_0	c_1	c_2	c_3	c_4
0.0	0.00828	-0.0132	0.0112	-0.00632	0.00377
0.2	0.0950	0.0472	-0.0756	-0.0115	0.0176
0.4	0.169	0.0591	-0.134	0.0308	0.00655
0.6	0.223	0.0989	-0.183	0.0288	0.0132
0.8	0.291	0.143	-0.269	0.0413	0.0211
$\Delta N2$					
f_{DIG}	c_0	c_1	c_2	c_3	c_4
0.0	0.00307	0.0145	0.0295	0.00878	-0.00786
0.2	0.0115	0.0180	0.0113	0.0102	-0.000491
0.4	0.0204	-0.00620	0.00106	0.0503	-0.0128
0.6	0.0280	-0.0123	-0.0147	0.0618	-0.0120
0.8	0.0376	-0.00259	-0.0388	0.0565	-0.002357
$\Delta S2$					
f_{DIG}	c_0	c_1	c_2	c_3	c_4
0.0	0.0105	-0.000192	-0.0110	-0.00180	0.00586
0.2	0.142	0.0960	-0.112	-0.0343	0.0313
0.4	0.240	0.125	-0.166	-0.00721	0.0235
0.6	0.318	0.166	-0.219	-0.00621	0.0289
0.8	0.397	0.223	-0.287	-0.0283	0.0479

regions in each galaxy is shown in Figure 25 for strong-line ratios, Figure 26 for electron temperatures, and Figure 27 for direct-method oxygen abundances. As before, we display the bias in direct-method oxygen abundance for three scenarios in which (1) both T_3 and T_2 are estimated directly from the galaxy spectrum, (2) only T_3 is known and T_2 is estimated from equation 12, and (3) only T_2 is known and T_3 is estimated from equation 12. For each model, we fit the bias in each property with the fourth-order polynomials of equations 25-27. The best-fit coefficients for the strong-line bias are presented in Table 2, while the best-fit coefficients for the electron temperature and direct-method oxygen abundance biases are given in Tables 3 and 4, respectively.

We recommend using the following procedure to apply corrections to individual galaxies or samples that are unrepresentative of the $z \sim 0$ star-forming population. First, estimate f_{DIG} for each galaxy or the median f_{DIG} of the sample using $\Sigma_{H\alpha}$ and equation 24. Identify the models presented in this appendix that bracket this f_{DIG} value. Interpolate between the best-fit polynomials of these bracketing models to obtain corrections for strong-line ratios, electron temperatures, or direct-method metallicities appropriate for the galaxy or sample of galaxies. Subtract the interpolated correction values for a given property from the values of that property as inferred from the global galaxy spectrum in order to correct for flux-weighting effects and DIG contamination. This procedure should yield robust corrections to individual galaxies or samples of galaxies that do not follow the mean local M_* -SFR relation. When inferring metallicities from strong-line calibrations, we recommend first

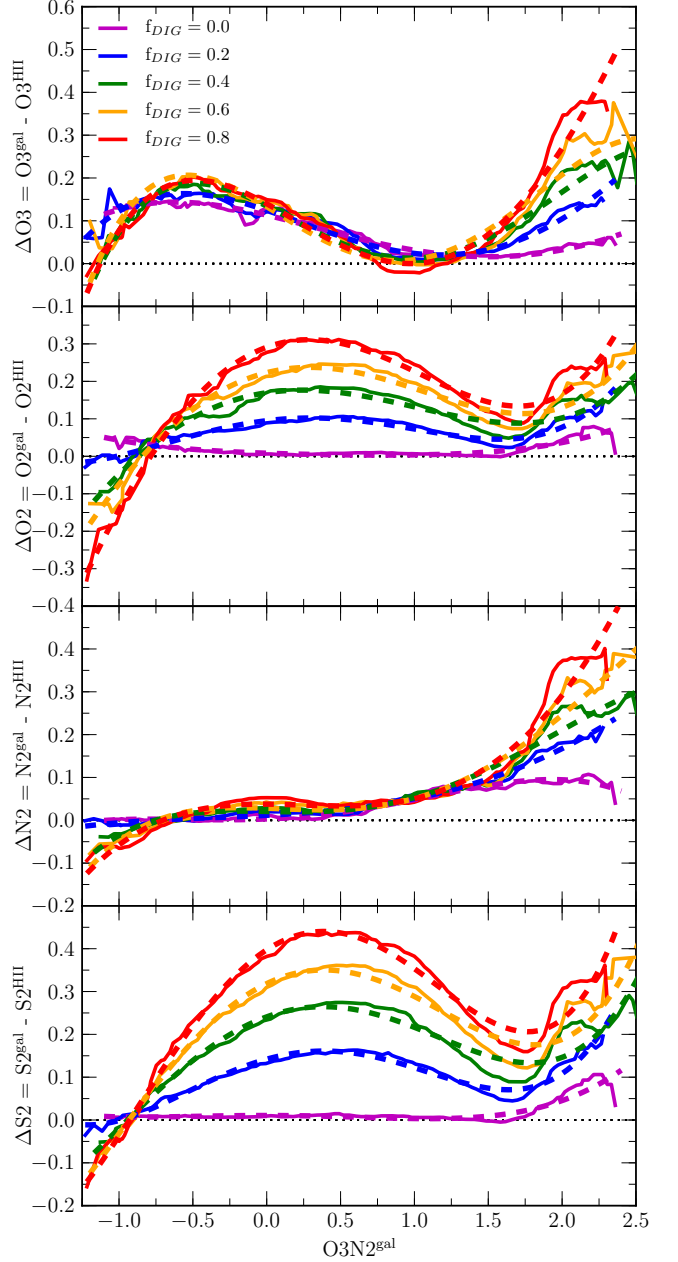


Figure 25. The difference between the global galaxy line ratio and median line ratio of the H II region distribution, ΔX , as a function of $O3N2^{gal}$ for the strong-line ratios $X=O3$, $O2$, $N2$, and $S2$. Solid lines show the running median of 2500 mock galaxy realizations in bins of $O3N2^{gal}$ for models with $f_{DIG}=0.0$ to 0.8 . In each panel, the dashed lines display the best-fit fourth-order polynomial to the bias in the global galaxy line ratio, ΔX , for the model of the corresponding color. The best-fit coefficients are presented in Table 2.

correcting the simple strong-line ratios $O3$, $O2$, $N2$, and $S2$, then constructing the corrected metallicity indicator (e.g., $R23$, $O3N2$) from these corrected simple ratios before using strong-line calibrations (empirical or theoretical) based on H II regions to estimate metallicity.

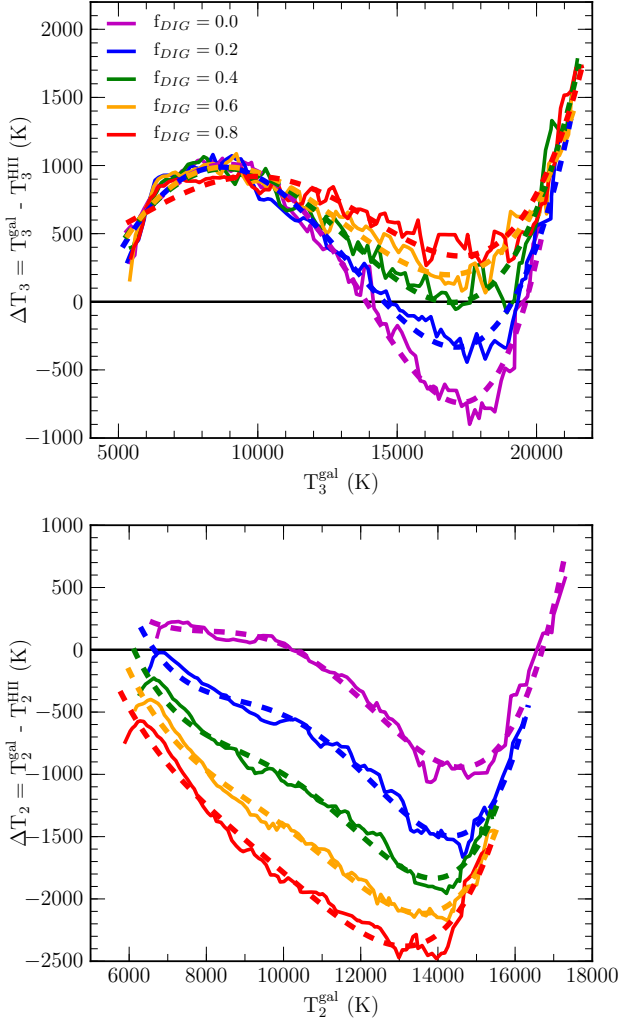


Figure 26. The difference between the electron temperature inferred from the global galaxy spectrum and the median electron temperature of the H II region distribution as a function of electron temperature. Results for T_3 are shown in the top panel, while the bias in T_2 is presented in the bottom panel, for models with DIG contribution ranging from $f_{\text{DIG}}=0.0$ to 0.8. Best-fit fourth-order polynomials for each model are presented as dashed lines of the corresponding color. The best-fit coefficients are given in Table 3.

Table 3
Global galaxy bias coefficients for electron temperatures (equation 26)

ΔT_3					
f_{DIG}	c_0	c_1	c_2	c_3	c_4
0.0	407.9	-4,953	16,610	-15,140	4,031
0.2	-2,444	7,038	-1,307	-3,995	1,623
0.4	-1,949	5,794	-795.2	-3,512	1,394
0.6	-2,796	9,447	-6,403	120.1	580.6
0.8	854.9	-3,791	9,842	-7,991	2,005
ΔT_2					
f_{DIG}	c_0	c_1	c_2	c_3	c_4
0.0	14,810	-63,090	99,850	-68,230	16,690
0.2	28,460	-114,500	169,400	-109,900	25,970
0.4	25,560	-103,700	154,300	-101,800	24,640
0.6	18,980	-76,430	112,600	-75,170	18,620
0.8	13,370	-54,490	80,700	-55,920	14,550

Table 4
Global galaxy bias coefficients for direct-method oxygen abundances (equation 27)

$\Delta \log(\text{O}/\text{H}) (T_3 \text{ and } T_2)^{\text{a}}$					
f_{DIG}	c_0	c_1	c_2	c_3	c_4
0.0	-0.0382	-0.402	-0.0948	0.381	0.123
0.2	0.0150	-0.299	0.408	0.100	-0.565
0.4	0.0776	-0.320	0.472	0.0335	-0.201
0.6	0.121	-0.327	0.847	-0.692	0.257
0.8	0.178	-0.431	1.26	-1.10	0.358
$\Delta \log(\text{O}/\text{H}) (T_3 \text{ only})^{\text{b}}$					
f_{DIG}	c_0	c_1	c_2	c_3	c_4
0.0	-0.0825	-0.550	-0.241	0.662	0.514
0.2	-0.0604	-0.473	0.0717	0.192	-0.0671
0.4	-0.0424	-0.518	0.320	0.202	-0.164
0.6	-0.0287	-0.545	0.586	-0.211	0.310
0.8	-0.0177	-0.617	1.13	-0.650	0.0385
$\Delta \log(\text{O}/\text{H}) (T_2 \text{ only})^{\text{c}}$					
f_{DIG}	c_0	c_1	c_2	c_3	c_4
0.0	0.0152	-0.341	-0.0727	0.306	-0.0113
0.2	0.129	-0.346	0.266	0.283	-0.346
0.4	0.246	-0.387	0.364	0.00148	-0.0165
0.6	0.352	-0.590	0.999	-0.662	0.203
0.8	0.485	-0.813	1.44	-1.08	0.347

^aThe direct-method $12+\log(\text{O}/\text{H})$ case where both T_3 and T_2 are directly determined from the galaxy spectrum.

^bThe case where only T_3 is estimated directly, while T_2 is inferred using equation 12.

^cThe case where only T_2 is estimated directly, while T_3 is inferred using equation 12.

APPENDIX B: HOW DO CHANGES IN σ_T AFFECT PREDICTED LINE RATIOS AND ELECTRON TEMPERATURES?

In our models of $z \sim 0$ galaxies, we assume that T_2 of DIG regions is 15% lower than T_2 of H II regions at fixed metallicity. This assumption was motivated by offsets between observations of $z \sim 0$ galaxies and the $f_{\text{DIG}}=0.55$ model in the strong-line ratio vs. T_2 diagrams (Fig. 10) when we assumed that DIG and H II region T_2 were the same at fixed metallicity. Our assumption regarding lower DIG T_2 additionally brought the magnitude of the predicted offset between H II regions and $z \sim 0$ galaxies in the T_2 - T_3 diagram into agreement with observations (Fig. 11). Given that there are no direct observational constraints of the electron temperature of DIG other than along one line-of-sight in the Milky Way (Reynolds et al. 2001), and the ionizing spectrum and gas physical conditions differ for DIG and H II regions, our assumption regarding DIG T_2 is not unreasonable. Nevertheless, it is worthwhile to consider whether the T_2 discrepancies can be resolved under a different set of assumptions.

The adopted value of the width of the input H II region T_3 distribution, σ_T , can significantly affect the electron temperatures inferred from mock global galaxy spectra. This effect has been demonstrated by Pilyugin et al. (2012b), who were able to reproduce the offset between H II regions and $z \sim 0$ galaxies in the T_2 - T_3 diagram by modeling galaxies as ensembles of H II regions with a range of metallicities (equivalent to a range of T_3). These authors found that the magnitude of the T_2 - T_3 offset increased as the range of metallicities of the combined H II regions increased. In our model framework, a wider

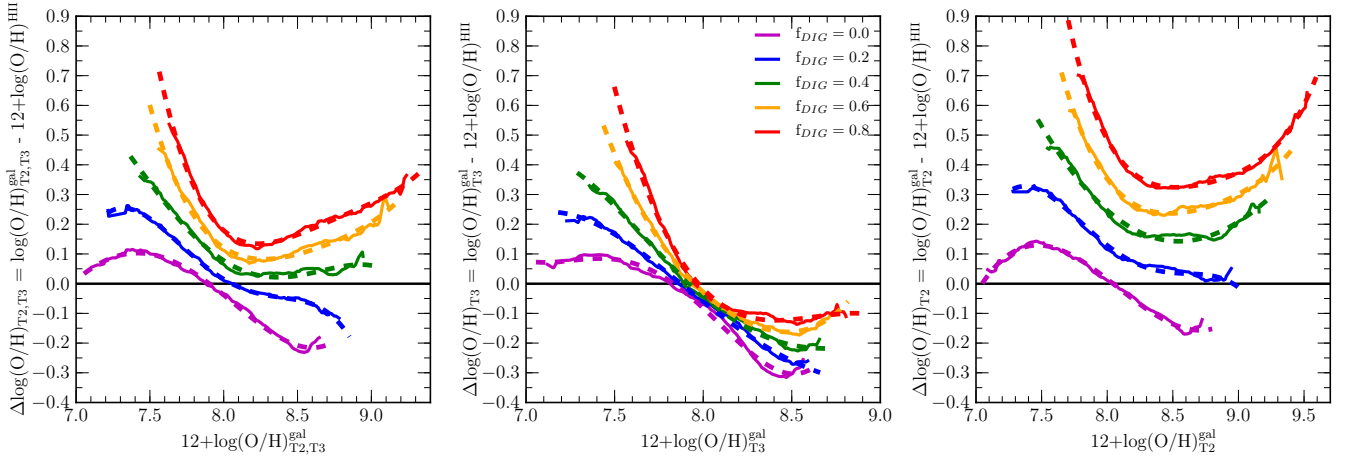


Figure 27. The difference between the global galaxy direct-method metallicity, inferred from the observed galaxy spectrum, and the median metallicity of the H II region distribution for models with $f_{\text{DIG}}=0.0$ to 0.8. We show the bias in global galaxy metallicity for three cases: both T_3 and T_2 are measured from the galaxy spectrum (left panel); only T_3 is measured directly and T_2 is estimated using the T_2 - T_3 relation of equation 12 (middle panel); and only T_2 is measured directly and T_3 is estimated using equation 12 (right panel). Dashed lines show the best-fit fourth-order polynomials for the model with the corresponding color. The best-fit coefficients are presented in Table 4.

range in metallicity is equivalent to increasing the value of σ_T . We adopted a value of $\sigma_T=0.07$ dex based on the observed T_3 distributions of H II regions in nearby spiral galaxies (Berg et al. 2015; Croxall et al. 2015, 2016). The results of Pilyugin et al. (2012b) suggest that adopting a larger value of σ_T could potentially resolve the discrepancy between models and observations in the T_2 - T_3 diagram without assuming different H II and DIG T_2 at fixed metallicity. We investigate the effects of adopting different values of σ_T on the predicted strong-line ratios and electron temperatures in order to determine whether different values of σ_T offer a viable solution to the discrepancies present in diagrams involving T_2 .

We produce a set of models that have the same input parameters except for σ_T , which is varied. We consider five values of the width of the log-normal T_3 distribution: $\sigma_T=[0.04, 0.07, 0.1, 0.15, 0.2]$. Other parameters are set to the values adopted in our fiducial models ($N_{\text{HII}} = 25$, $f_{\text{DIG}}=0.55$, $\log(T_{\text{cent}}/\text{K}) = 3.7$ to 4.3). In these models, we do not assume a lower DIG T_2 at fixed metallicity, but instead assume that T_2 of H II and DIG regions is equal at fixed metallicity.

The models with varied σ_T are shown in the T_2 - T_3 diagram in Figure 28. When working under the assumption that H II region and DIG T_2 are equal at fixed metallicity, $\sigma_T \approx 0.15$ dex is required to match $z \sim 0$ observations in the T_2 - T_3 diagram. This value of σ_T is roughly twice the value observed for H II region distributions in local spiral galaxies (Berg et al. 2015; Croxall et al. 2015, 2016). We show predictions from the same set of models in the strong-line ratio O3N2, O3S2, and O3O2 diagrams in Figure 29. Increasing σ_T results in lower $[\text{S II}]/\text{H}\alpha$ and $[\text{O II}]/\text{H}\beta$ at fixed $[\text{O III}]/\text{H}\beta$. Changes to the global galaxy strong-line excitation sequences come about because increasing the range of H II region T_3 also increases the range of H II and DIG region strong-line ratios (Fig. 2). Combining light from H II and DIG regions with a wider range of strong-line ratios results in different average excitation sequences because the relation between each strong-line ratio and T_3 is different.

The $\sigma_T=0.15$ model significantly underpredicts $[\text{S II}]/\text{H}\alpha$ and $[\text{O II}]/\text{H}\beta$ at fixed $[\text{O III}]/\text{H}\beta$ for $z \sim 0$

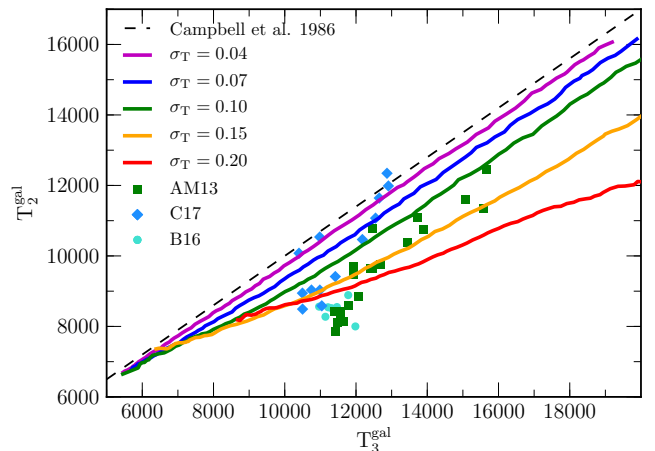


Figure 28. The global galaxy ionic temperature diagram of T_2^{gal} vs. T_3^{gal} , including models for which only σ_T is varied. The solid colored lines show predictions of models with $f_{\text{DIG}}=0.55$ and different values of σ_T , under the assumption that DIG and H II region T_2 is the same at fixed metallicity. The dashed black line shows the H II region T_2 - T_3 relation of Campbell et al. (1986) given in equation 12. The colored points indicate stacks of $z \sim 0$ SDSS galaxies with auroral-line measurements.

galaxies. While this discrepancy could potentially be resolved by adopting both a larger σ_T and larger f_{DIG} , reconciling the $\sigma_T=0.15$ model with observations in the O3S2 and O3O2 diagrams would require $f_{\text{DIG}} \gtrsim 0.8$. Such a high fraction of Balmer emission originating from DIG is in conflict with narrowband $\text{H}\alpha$ studies of nearby galaxies which place the DIG fraction at 30 – 60% (Zurita et al. 2000; Oey et al. 2007). While adopting a larger σ_T than our fiducial value of 0.07 dex can reproduce the T_2 - T_3 offset without additional assumptions regarding DIG T_2 , this assumption also results in strong-line ratios that disagree significantly with observations of galaxies. We conclude that our assumed value of $\sigma_T=0.07$ dex is reasonable alongside the assumption that DIG T_2 is lower than that of H II regions at fixed metallicity. Increasing the adopted values of σ_T and f_{DIG} while assuming equal DIG and H II region T_2 at fixed metallicity cannot provide a

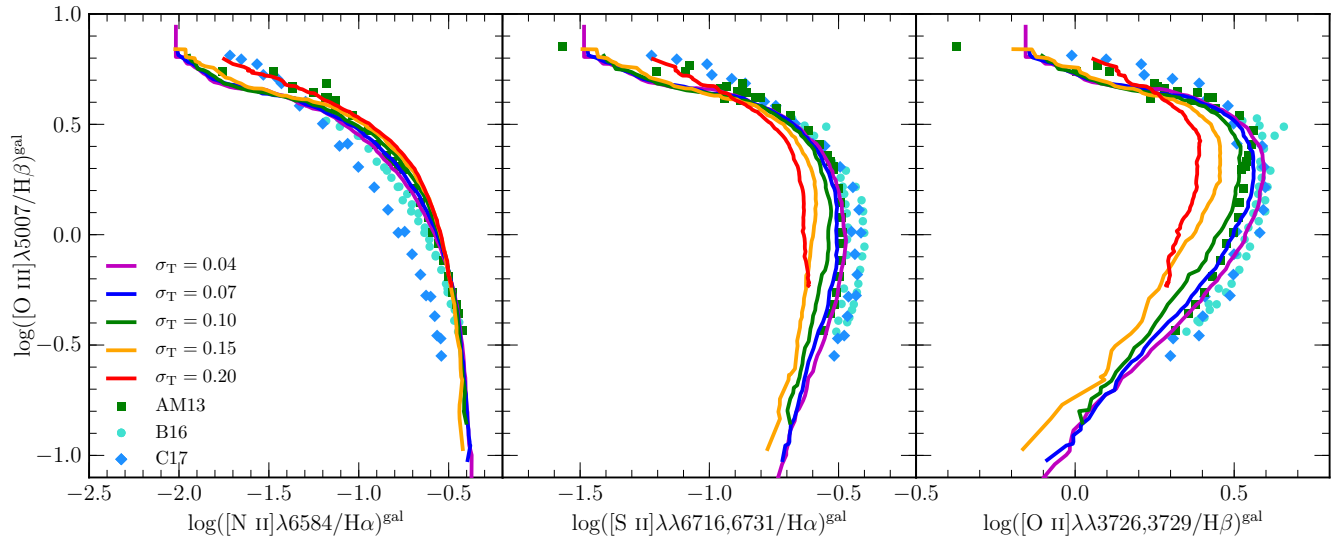


Figure 29. The O3N2 (left), O3S2 (middle), and O3O2 (right) strong-line ratio diagrams for stacks of SDSS galaxies and models with varying σ_{T_2} . Colored lines and points are the same as in Figure 28.

solution to the T_2 discrepancies in Figures 10 and 11.

REFERENCES

- Abazajian, K. N., Adelman-McCarthy, J. K., Agüeros, M. A., et al. 2009, *ApJS*, 182, 543
- Andrews, B. H., & Martini, P. 2013, *ApJ*, 765, 140
- Ascasibar, Y., Guidi, G., Casado, J., Scannapieco, C., & Díaz, A. I. 2016, *ArXiv e-prints*, arXiv:1602.08474
- Barnes, J. E., Wood, K., Hill, A. S., & Haffner, L. M. 2015, *MNRAS*, 447, 559
- Barrera-Ballesteros, J. K., Sánchez, S. F., Heckman, T., & Blanc, G. A. 2017, *ArXiv e-prints*, arXiv:1706.09893
- Berg, D. A., Skillman, E. D., Croxall, K. V., et al. 2015, *ApJ*, 806, 16
- Berg, D. A., Skillman, E. D., Garnett, D. R., et al. 2013, *ApJ*, 775, 128
- Berg, D. A., Skillman, E. D., Marble, A. R., et al. 2012, *ApJ*, 754, 98
- Bian, F., Kewley, L. J., Dopita, M. A., & Juneau, S. 2016, *ApJ*, 822, 62
- Blanc, G. A., Kewley, L., Vogt, F. P. A., & Dopita, M. A. 2015, *ApJ*, 798, 99
- Bresolin, F. 2007, *ApJ*, 656, 186
- . 2011, *ApJ*, 730, 129
- Brinchmann, J., Charlot, S., White, S. D. M., et al. 2004, *MNRAS*, 351, 1151
- Brown, J. S., Croxall, K. V., & Pogge, R. W. 2014, *ApJ*, 792, 140
- Brown, J. S., Martini, P., & Andrews, B. H. 2016, *MNRAS*, 458, 1529
- Bundy, K., Bershady, M. A., Law, D. R., et al. 2015, *ApJ*, 798, 7
- Campbell, A., Terlevich, R., & Melnick, J. 1986, *MNRAS*, 223, 811
- Cardelli, J. A., Clayton, G. C., & Mathis, J. S. 1989, *ApJ*, 345, 245
- Cowie, L. L., Barger, A. J., & Songaila, A. 2016, *ApJ*, 817, 57
- Croxall, K. V., Pogge, R. W., Berg, D. A., Skillman, E. D., & Moustakas, J. 2015, *ApJ*, 808, 42
- . 2016, *ApJ*, 830, 4
- Curti, M., Cresci, G., Mannucci, F., et al. 2017, *MNRAS*, 465, 1384
- Davé, R., Rafieferantsoa, M. H., Thompson, R. J., & Hopkins, P. F. 2017, *MNRAS*, 467, 115
- Dopita, M. A., Kewley, L. J., Sutherland, R. S., & Nicholls, D. C. 2016, *Ap&SS*, 361, 61
- Erb, D. K., Shapley, A. E., Pettini, M., et al. 2006, *ApJ*, 644, 813
- Finlator, K., & Davé, R. 2008, *MNRAS*, 385, 2181
- Fischer, C. F., & Tachiev, G. 2014, MCHF/MCDHF Collection, Version 2, Ref No. 10 & 20, Available online at <http://physics.nist.gov/mchf>, National Institute of Standards and Technology
- Flores-Fajardo, N., Morisset, C., Stasińska, G., & Binette, L. 2011, *MNRAS*, 415, 2182
- Gutkin, J., Charlot, S., & Bruzual, G. 2016, *MNRAS*, 462, 1757
- Haffner, L. M., Reynolds, R. J., & Tuftte, S. L. 1999, *ApJ*, 523, 223
- Haffner, L. M., Dettmar, R.-J., Beckman, J. E., et al. 2009, *Reviews of Modern Physics*, 81, 969
- Heckman, T. M., Robert, C., Leitherer, C., Garnett, D. R., & van der Rydt, F. 1998, *ApJ*, 503, 646
- Ho, I.-T., Kudritzki, R.-P., Kewley, L. J., et al. 2015, *MNRAS*, 448, 2030
- Hoopes, C. G., & Walterbos, R. A. M. 2003, *ApJ*, 586, 902
- Hudson, C. E., & Bell, K. L. 2005, *A&A*, 430, 725
- Izotov, Y. I., Stasińska, G., Meynet, G., Guseva, N. G., & Thuan, T. X. 2006, *A&A*, 448, 955
- James, P. A., Bretherton, C. F., & Knapen, J. H. 2009, *A&A*, 501, 207
- Jones, T., Ellis, R., Jullo, E., & Richard, J. 2010, *ApJ*, 725, L176
- Jones, T., Ellis, R. S., Richard, J., & Jullo, E. 2013, *ApJ*, 765, 48
- Jones, T., Martin, C., & Cooper, M. C. 2015, *ApJ*, 813, 126
- Kauffmann, G., Heckman, T. M., Tremonti, C., et al. 2003, *MNRAS*, 346, 1055
- Kennicutt, Jr., R. C., Bresolin, F., & Garnett, D. R. 2003, *ApJ*, 591, 801
- Kewley, L. J., & Dopita, M. A. 2002, *ApJS*, 142, 35
- Kewley, L. J., Dopita, M. A., Sutherland, R. S., Heisler, C. A., & Trevena, J. 2001, *ApJ*, 556, 121
- Kewley, L. J., & Ellison, S. L. 2008, *ApJ*, 681, 1183
- Kewley, L. J., Maier, C., Yabe, K., et al. 2013, *ApJ*, 774, L10
- Kobulnicky, H. A., Kennicutt, Jr., R. C., & Pizagno, J. L. 1999, *ApJ*, 514, 544
- Kobulnicky, H. A., & Kewley, L. J. 2004, *ApJ*, 617, 240
- Lara-López, M. A., Cepa, J., Bongiovanni, A., et al. 2010, *A&A*, 521, L53
- Law, D. R., Cherinka, B., Yan, R., et al. 2016, *AJ*, 152, 83
- Leethochawalit, N., Jones, T. A., Ellis, R. S., et al. 2016, *ApJ*, 820, 84
- Leitherer, C., Ekström, S., Meynet, G., et al. 2014, *ApJS*, 212, 14
- Liang, Y. C., Hammer, F., Yin, S. Y., et al. 2007, *A&A*, 473, 411
- Liu, X., Shapley, A. E., Coil, A. L., Brinchmann, J., & Ma, C.-P. 2008, *ApJ*, 678, 758
- Ma, X., Hopkins, P. F., Feldmann, R., et al. 2017, *MNRAS*, 466, 4780
- Maiolino, R., Nagao, T., Grazian, A., et al. 2008, *A&A*, 488, 463
- Mannucci, F., Cresci, G., Maiolino, R., Marconi, A., & Gnerucci, A. 2010, *MNRAS*, 408, 2115
- Masters, D., Faisst, A., & Capak, P. 2016, *ApJ*, 828, 18

- Moustakas, J., Zaritsky, D., Brown, M., et al. 2011, ArXiv e-prints, arXiv:1112.3300
- Nakajima, K., & Ouchi, M. 2014, MNRAS, 442, 900
- Oey, M. S., Meurer, G. R., Yelda, S., et al. 2007, ApJ, 661, 801
- Onodera, M., Carollo, C. M., Lilly, S., et al. 2016, ApJ, 822, 42
- Osterbrock, D. E., & Ferland, G. J. 2006, *Astrophysics of gaseous nebulae and active galactic nuclei*
- Otte, B., Gallagher, III, J. S., & Reynolds, R. J. 2002, ApJ, 572, 823
- Otte, B., Reynolds, R. J., Gallagher, III, J. S., & Ferguson, A. M. N. 2001, ApJ, 560, 207
- Peebles, M. S., & Shankar, F. 2011, MNRAS, 417, 2962
- Pellegrini, E. W., Baldwin, J. A., & Ferland, G. J. 2011, ApJ, 738, 34
- Pettini, M., & Pagel, B. E. J. 2004, MNRAS, 348, L59
- Pilyugin, L. S., & Grebel, E. K. 2016, MNRAS, 457, 3678
- Pilyugin, L. S., Grebel, E. K., & Mattsson, L. 2012a, MNRAS, 424, 2316
- Pilyugin, L. S., Vílchez, J. M., Cedrés, B., & Thuan, T. X. 2010, MNRAS, 403, 896
- Pilyugin, L. S., Vílchez, J. M., Mattsson, L., & Thuan, T. X. 2012b, MNRAS, 421, 1624
- Reynolds, R. J., Haffner, L. M., Madsen, G. J., Wood, K., & Hill, A. S. 2012, in *EAS Publications Series*, Vol. 56, EAS Publications Series, ed. M. A. de Avillez, 213–220
- Reynolds, R. J., Haffner, L. M., & Tufte, S. L. 1999, ApJ, 525, L21
- Reynolds, R. J., Scherb, F., & Roesler, F. L. 1973, ApJ, 185, 869
- Reynolds, R. J., Sterling, N. C., Haffner, L. M., & Tufte, S. L. 2001, ApJ, 548, L221
- Rosolowsky, E., & Simon, J. D. 2008, ApJ, 675, 1213
- Salim, S., Lee, J. C., Ly, C., et al. 2014, ApJ, 797, 126
- Sánchez, S. F., Rosales-Ortega, F. F., Jungwiert, B., et al. 2013, A&A, 554, A58
- Sánchez, S. F., Rosales-Ortega, F. F., Iglesias-Páramo, J., et al. 2014, A&A, 563, A49
- Sanders, R. L., Shapley, A. E., Kriek, M., et al. 2015, ApJ, 799, 138
- . 2016, ApJ, 816, 23
- SDSS Collaboration, Albareti, F. D., Allende Prieto, C., et al. 2016, ArXiv e-prints, arXiv:1608.02013
- Seon, K.-I., Witt, A., Kim, I.-J., et al. 2011, ApJ, 743, 188
- Shapley, A. E., Coil, A. L., Ma, C.-P., & Bundy, K. 2005, ApJ, 635, 1006
- Shapley, A. E., Reddy, N. A., Kriek, M., et al. 2015, ApJ, 801, 88
- Shivaei, I., Reddy, N. A., Shapley, A. E., et al. 2015, ArXiv e-prints, arXiv:1507.03017
- Stasińska, G. 2005, A&A, 434, 507
- Steidel, C. C., Rudie, G. C., Strom, A. L., et al. 2014, ApJ, 795, 165
- Storey, P. J., Sochi, T., & Badnell, N. R. 2014, MNRAS, 441, 3028
- Tayal, S. S. 2007, ApJS, 171, 331
- Toribio San Cipriano, L., García-Rojas, J., Esteban, C., Bresolin, F., & Peimbert, M. 2016, MNRAS, 458, 1866
- Tremonti, C. A., Heckman, T. M., Kauffmann, G., et al. 2004, ApJ, 613, 898
- Troncoso, P., Maiolino, R., Sommariva, V., et al. 2014, A&A, 563, A58
- van der Wel, A., Franx, M., van Dokkum, P. G., et al. 2014, ApJ, 788, 28
- Voges, E. S., & Walterbos, R. A. M. 2006, ApJ, 644, L29
- Wang, X., Jones, T. A., Treu, T., et al. 2017, ApJ, 837, 89
- Whitaker, K. E., Franx, M., Leja, J., et al. 2014, ApJ, 795, 104
- Yan, R., Bundy, K., Law, D. R., et al. 2016, AJ, 152, 197
- Yates, R. M., Kauffmann, G., & Guo, Q. 2012, MNRAS, 422, 215
- York, D. G., Adelman, J., Anderson, Jr., J. E., et al. 2000, AJ, 120, 1579
- Yuan, T.-T., Kewley, L. J., Swinbank, A. M., Richard, J., & Livermore, R. C. 2011, ApJ, 732, L14
- Zahid, J., Dima, G., Kudritzki, R., et al. 2014, ArXiv e-prints, arXiv:1404.7526
- Zhang, K., Yan, R., Bundy, K., et al. 2017, MNRAS, 466, 3217
- Zurita, A., Rozas, M., & Beckman, J. E. 2000, A&A, 363, 9